The Effect of Bond Coat Oxidation on the Microstructure and Endurance of Two Thermal Barrier Coating Systems

By

Ryan Daniel Jackson

A thesis submitted to the
University of Birmingham
for the degree of
Doctor of Philosophy

School of Metallurgy and Materials
College of Engineering and Physical Sciences
University of Birmingham
September 2009

ABSTRACT

A series of isothermal and cyclic oxidation tests were carried out on two thermal barrier coating systems consisting of a CMSX-4 nickel-based superalloy substrate, NiCoCrAlY overlay bond coat applied by two different techniques and a yttria stabilised zirconia topcoat applied by electron beam physical vapour deposition (EBPVD). The bond coats were applied by either high velocity oxy-fuel spraying (HVOF) or EBPVD. Isothermal oxidation tests were carried out at 950°C, 1050°C and 1150°C for both coating system for up to 3000 hours. Cyclic oxidation testing was conducted at 1150°C in one hour cycles to coating failure on both coatings.

A detailed examination on the oxide thickness was conducted on all specimens, along with characterisation of the bond coat and TGO. This was coupled with examination of specimen cross-sections for cracking and signs of coating degradation.

Isothermal oxidation showed sub parabolic oxide growth consistent with the literature. Detailed analysis of oxide thickness showed a normal distribution but with increasing standard deviation with increasing oxidation time. Both bond coats were dual phase, $\beta + \gamma$. The EBPVD applied bond coat only, was found to contain yttrium rich precipitates in the bond coat and TGO. Both coatings showed no increase in surface roughness after either isothermal or thermal cycle testing.

Short sub-critical cracks were observed at the TGO/topcoat interface in the HVOF applied bond coat only associated with the flanks of asperities. Coating failure in both coatings occurred at the TGO/bond coat interface on cooling and was likely driven by the thermal expansion mismatch between the TGO, topcoat and substrate. The initial mechanism of crack formation was not determined conclusively but could be a wedge cracking type mechanism.

DEDICATION

I would like to dedicate this to my parents Angela and Mervyn Jackson and my two sisters Clare and Lisa, who have provided me not only with support but also motivated me throughout this work and my life.

ACKNOWLEDGEMENTS

I would first and foremost like to thank my supervisor Prof Hugh Evans for supporting me through this work. A particular thank you also goes to the staff of the Center for Electron Microscopy and Metallurgy and Materials workshop for their support in the experimental work.

I would also like to acknowledge Siemens Industrial Turbomachinery for providing the specimens for this project.

I reserve a special and most important final thank you to Dr Mary Taylor who has provided me with endless, support, help, and advice throughout this work. My thanks could not do justice to the support you have provided me over the last 4 years.

CONTENTS

LIST OF FIGURES

LIST OF TABLES

1 INTRODUCTION

The role of coatings in the protection of metals from high temperature degradation has been seen as important since the start of the 20th century[1, 2]. These first coatings were an early form of aluminium diffusion coating and a process of pack cementation aluminising was patented in 1911 by Van Aller[1]. These first coatings were used to provide protection from the hot environment in power plant steam condensers for example[1]. Their use quickly spread to other furnace components and combustion environments, but with little understanding of the mechanisms by which protection was being afforded[1, 2]. It was hypothesised however that the protection came from the formation of an alumina layer on the coating surface[1].

The first use of coatings of this sort for gas turbines came as early as 1942 with work by Anselm Franz, who used aluminising of low alloy steel as an alternative to more expensive and rare high alloy steels[1]. The thermal protection afforded by these coatings allowed for an increase in the temperatures the components were exposed to. It was found early on that increasing the inlet temperature of the gas turbine allowed for significant increases in engine power and/or efficiency[1-3]. These early coatings in use were solely metallic single layer coatings. It was at this time in the late 1940's that the idea of using a ceramic coating was hypothesised and tested by Bartoo and Clure[4]. They combined this coating with internal air cooling of the turbine blade which provided a great increase in the temperature the component could operate at[4]. The first operational components to use coatings came in 1960 with their use on rocket nozzles[1, 4]. During this time advances in alloy design with the use of cobalt based alloys and then nickel based alloys allowed for further rises in inlet temperature capacity[1]. From the 1960's with the use of air cooled components, mainly turbine blades, further advancements were sought in coatings technology. Focus remained on aluminising and this process continued to evolve, additionally new overlay style coatings were in development which allowed for optimising environmental protection with less emphasis on the substrate material properties[1]. The first such overlay coatings came from the requirements of environmental protection for the nuclear industry and FeCrAlY alloys were soon transferred to use in gas turbines[1]. Further developments over the remaining years focused on optimisation of the coating constituents through use of CoCrAlY, NiCrAlY and CoNiCrAlY coatings[1]. More recent study on coatings has led to the refinement of the coating composition and addition of platinum to diffusion coatings to increase oxide adherence[1, 5]. Figure 1.1 shows schematically the evolution of turbine entry temperature (TET) with changes in alloy design and coatings. It demonstrates that since the introduction of coatings commercially in around 1960 the turbine capability has risen above that of the alloy. This has steadily increased with the optimisation of the coatings and in around 1985[4]came the introduction of ceramic coatings in combination with metallic coatings.

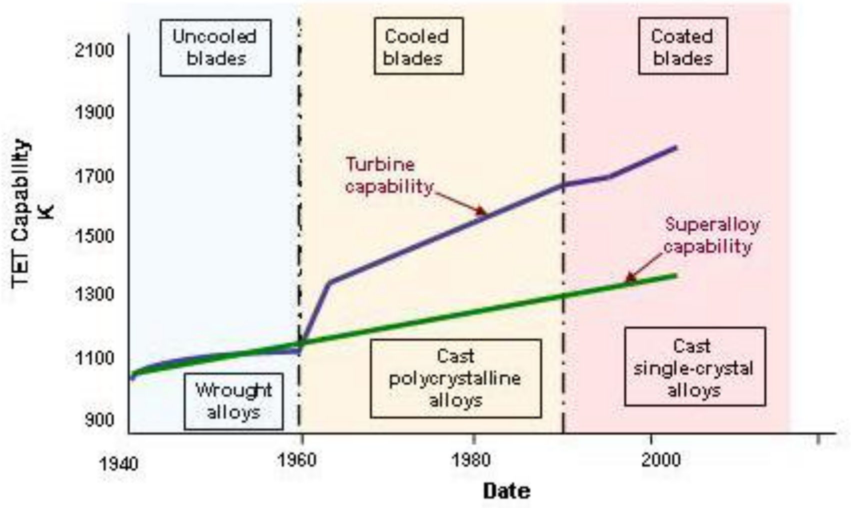

Figure 1.1: Schematic chart showing the increase in turbine entry temperature (TET) over time with changing technology[6].

Both metallic and ceramic coatings first found use in aero gas turbines with specific drive initially for military applications[2, 4]. The requirements of these applications specifically increase in engine power output, led to the drive for higher entry temperatures. These advancements were then passed down to civil aero gas turbine use and led to a significant increase in engine efficiency through reduced need for internal cooling[7]. Land based gas turbines however, whilst having similar requirements to aero engines tend to run at a much lower temperature and as such the requirements for coatings in these applications is much less. Despite this there is an ever growing push for increasing efficiency and so reducing emission from land based gas turbines. As such the entry temperatures for land based gas turbines now require the use of metallic/ceramic coatings- Thermal Barrier Coatings (TBC's).

This thesis evaluates two thermal barrier coating systems for use in a land based gas turbine. As such it will examine the rates of oxidation and thermal stability of the coating at elevated temperatures. It will also describe the major failure mechanisms associated with these coatings and seek to draw parallels with the observed failure modes for the coatings studied here. The first part of this thesis will look to give background information to the process of metal oxidation and the application and use of TBC's. It will then give an overview of the major failure mechanisms involved in these coatings as described in the literature. The remainder of this work will look at the two specific coatings studied here and provide results and observations to the oxidation mechanisms and failure modes, whilst drawing comparisons between the two coatings and the literature.

2 OXIDATION AND DEGRADATION OF METALS AND ALLOYS

2.1 Basic Metal Oxidation

The initial step in the oxidation of metals involves the adsorption of oxygen atoms onto the metal surface [8]. The oxygen can then react at the surface to form either discrete nuclei of oxide and/or a complete film, the generalised equation for this reaction is given in reaction 2.1 [8, 9].

$$aMe + \frac{b}{2}O_2 \rightarrow Me_aO_b \tag{2.1}$$

This process is affected by a number of factors including the surface orientation, presence of crystal defects, surface impurities and impurities in the oxidising gas[8, 9].

The initial oxide film produced creates a barrier between the metal and oxygen, therefore further oxidation requires solid-state diffusion of cations (M^{x+}) and or anions (O^{2-}) through the oxide film [8, 10].

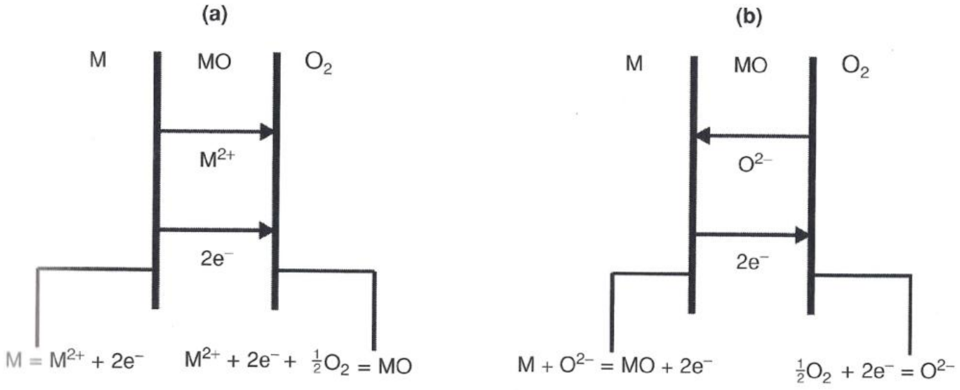

Figure 2.1: Schematic of the transport paths involved in the oxidation of a metal, a) cation transport, b) anion transport[9]

The location of continued growth of the oxide is therefore determined by the predominating diffusion species. If the cation diffusion dominates then new oxide will form at the oxide/gas interface, figure 2.1(a). Alternatively new oxide growth will occur at the scale metal interface should anion diffusion dominate, figure 2.1(b)[9].

This diffusion is driven by electric fields set up through the oxide film and a chemical potential gradient across the film. Along with the diffusion of ions through the oxide, vacancies migrate in the opposite direction to the ion movement. There are typically two types of defect involved in this diffusion process and they are Frenkel defects, whereby the anion lattice is complete and the cation lattice contains vacancies with cation interstitials[9]. Schotky defects contain an equal number of vacancies on both the anion and cation lattice. However in order to maintain neutrality of the scale a movement of electrons must occur along with the ions, figure 2.1.[9] For this to occur the oxide produced must be non-stoichiometric in nature to allow electrons to be elevated to the conduction band[9]. This non-stoichiometry can be caused by either a deficit of cations and corresponding excess of anion, referred to as negative superconductors, or by a deficit of anions (O^{2-}) and corresponding excess of cations, termed positive superconductors. Oxides of metals typically used in this work such as alumina, chromia and nickel oxide are positive superconductors[9].

2.2 Oxidation Rates

It can be observed from the previous section that the rate of oxidation is dependent to a large extent upon the diffusion of cations and/or anions across the oxide and also on the conductivity of the oxide scale. An ideal model for this dependence has been described by Wagner[11].

The Wagner model makes a number of important assumptions to simplify the overall behaviour, some of these are listed below[11].

- The oxide scale is dense and adherent to allow free ion transport.
- The oxidation rate is dependent upon diffusion of ions across the scale.
- There is thermodynamic equilibrium of atoms, ions and electrons at the reaction interfaces.

For oxide growth dominated by cation diffusion the number of diffusing ions per unit area of oxide surface per second (flux) of the cation (JM^{2+}) is equal to the flux of vacancy movement inwards ($-JV_m$), equation 2.2 [11].

$$JM^{2+} = -JV_m = DV_m \frac{C''_{V_m} - C'_{V_m}}{\xi} \qquad (2.2)$$

DV_m = Cation vacancy diffusion co-efficient

C''_{V_m} = Cation vacancy concentration at oxide/metal interface

C'_{V_m} = Cation vacancy concentration at oxide/gas interface

ξ = oxide thickness

As both interfaces are at thermodynamic equilibrium then $C''_{V_m} - C'_{V_m}$ must be constant at all times, therefore this equation can be simplified, equation 2.3 [11].

$$JM^{2+} = \frac{1}{A_{ox}}\frac{dx}{dt} = DV_m \frac{C''_{V_m} - C'_{V_m}}{\xi} \qquad (2.3)$$

A_{ox} = Volume of oxide formed

t = time

Therefore by rearranging this formula and creating a rate constant k', equation 2.4 and integrate assuming x=0 at t=0 to give the parabolic rate constant shown in equation 2.5 [11]

$$\frac{dx}{dt} = \frac{k'}{\xi} \quad \text{Where,} \quad k' = DV_m A_{ox}(C''_{V_m} - C'_{V_m}) \qquad (2.4)$$

The rate of oxidation is also affected by the temperature, pressure of oxygen, time and surface preparation[8, 9]. Under ideal conditions most metals will follow one of three rate equations depending upon the temperature: at lower temperatures the rate follows a logarithmic equation; at higher temperatures the oxidation rate follows a parabolic type equation; under non-protective conditions, a linear rate response from the metal[8, 9] may be observed. This project focuses on temperatures and pressures under which ideally a parabolic relationship would occur and so this will be discussed in the following section. However under these conditions it has now been shown that sub parabolic kinetics are more usually seen[12-16] and these will be discussed in section 2.2.2.

2.2.1 Parabolic

Ideal parabolic relationship for the growth of an oxide has been described by Wagner as discussed in the previous section and has been shown to occur in a number of oxide forming systems[8, 11, 17]. Equation 2.5 describes the kinetics of the process based on the thickness of the oxide formed at a given exposure time at temperature.

$$\xi^2 = K_p t + C_p \tag{2.5}$$

Where, t = time at temperature

K_p = parabolic rate constant~~s~~

C_p = integration Factor

ξ = oxide film thickness or mass gain

Grain boundary diffusion is also important for polycrystalline materials as diffusion at the grain boundary has a lower activation energy (~half that of lattice diffusion) than diffusion through the lattice structure. The growth of alumina at temperatures of around 900-1000°C is thought to be dominated [9, 18-20] by the inward transport of oxygen ions along oxide grain boundaries which act as fast-transport paths[20]. Should the number of oxide grain boundaries decrease during oxidation due to preferential nucleation of oxide grains, the effective diffusion coefficient will reduce as will the oxidation rate. As a consequence, sub-parabolic growth rates of alumina are observed[20]

2.2.2 Sub parabolic Kinetics

Several experimental studies of oxidation resistant coatings and alloys has shown a tendency away from the parabolic kinetics predicted by Wagner's theories[21]. These types of kinetics are described using a modified version of equation 2.5 shown in equation 2.6, whereby the value of the growth exponent n is greater than 2[22].

$$\xi^n = K_n t + C_n \tag{2.6}$$

This equation is describes the oxidation of a system where the initially formed oxide is non-protective and the subsequently formed oxide is protective[22]. It can be applied also to an oxide growing by parabolic kinetics where the exponent n becomes 2. It has been used in the literature[23, 24] to describe the sub parabolic oxidation of thermal barrier coatings.

Experimental studies in the literature have shown values for n can be in excess of 3 depending upon the type of system and testing regime[13, 15, 16, 21]. A number of theories have been proposed for this behaviour, the first of which is the reduction in available "short-circuit" diffusion paths available as a consequence of increased average oxide grain size through preferential nucleation of oxide grains[25], as described briefly in the previous section. Such behaviour has been described in the literature for many systems[12-16] for example Quadakkers et al[26] on FeCrAl alloys and show that the effective diffusion rate of oxygen across the scale varies with the grain size, whereby the diffusion rate decreased with increasing grain size. It is then clear that this is an important observation for the description of sub parabolic and cubic, where $n \geq 3$, growth kinetics; however it is important to know whether it is possible for the grain size to change with time. Studies on some oxide scales such as NiO and zirconia[12, 14] have demonstrated that the average grain size can indeed increase with increasing time at temperature.

Increase in average oxide grain size though is not the only model to describe sub-parabolic growth kinetics in oxides. A continuous increase in compressive growth stress within the oxide layer will decrease the diffusion rate of vacancies across the oxide this will then reduce the growth rate of an oxide, likewise a tensile stress will increase the oxide growth rate[27-30]. This effect has been described and modelled by Evans et al for zirconia and agrees with the observations of the other systems cited above [31] [32].

The third described mechanism comes from the transformation of less stable isoforms of alumina such as γ and θ, which form along with α-alumina during the early competitive stages of oxide growth on the bare metal surface[33, 34]. These isoforms differ in their electronic structure, density and stability at temperature as shown in table 2.1, which gives some of the basic properties of three main isoforms.

Table 2.1: Some selected properties of the main important alumina isoforms[35].

	α- alumina	γ-alumina	θ-alumina
Structure	Rhombohedral	Monoclinic	Modified FCC
Density (Kg/m3)	3980-3990	3560-3600	3200-3700
Elastic modulus, E (GPa)	409-441	-	-
Hardness (GPa)	28	-	-
Melting point (°C)	2051		
Transition Temperature (°C)		Transition to α- ~925	Transition to δ- 700-800

At temperatures above around 1000°C only the more dense α phase remains stable and at this temperature the other main isoforms fully transform into this phase[35]. Common to this process for all isoforms is that the transformations from a less stable form to a more stable form at differing temperatures results ultimately in the irreversible transformation to α phase [35]. This transformation to the denser and more stable isoform results in changing of the oxide growth kinetics[33]. The transitional aluminas γ and θ both have growth rates which are greater than α alumina, figure 2.2 and as such the transition to α at higher temperatures could result in sub parabolic kinetics observed in the literature[35].

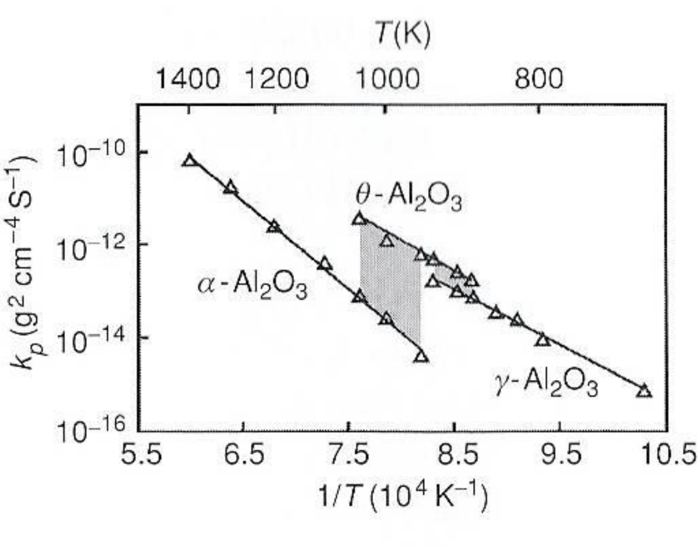

Figure 2.2: Arrhenius plot of the rate constant Kp for oxidation of isoforms of aluminas on a NiAl substrate[35]

2.3 Thermodynamics

The oxidation rate constant as shown by equation 2.6 is related to the concentration of vacancies and this has also been shown to be proportional to the oxygen partial pressure at the interface. Therefore from equation 2.6[17],

$$k^{'} \propto [(P_{O_2}^{'})^{\frac{1}{x}} - (P_{O_2}^{''})^{\frac{1}{x}}] \tag{2.7}$$

$k^{'}$ = rate constant

$P_{O_2}^{'}$ and $P_{O_2}^{''}$ = oxygen partial pressure at the oxide/gas interface and the oxide/metal interface respectively

Typically in a cation dominated process the partial pressure of oxygen at the oxide/metal interface would be negligible when compared to the pressure at the oxide/gas interface and so this term can typically be omitted[8].

For an oxide to form on any metal the partial pressure of oxygen must be greater than the partial pressure of oxygen present at equilibrium for the given oxide. This can be shown in equation (2.9) for the following reaction[8].

$$aMe + \frac{b}{2}O_2 \rightarrow Me_aO_b \qquad (2.8)$$

$$\Delta G = -RT\ln\left(\frac{a_{oxide}}{a_{metal}^{a} \times P_{O_2}^{b}}\right) \qquad (2.9)$$

ΔG= Free energy of formation of the oxide

R= Universal gas constant

T= Temperature (K)

a_{oxide} = Activity of the oxide

a_{metal} = Activity of the metal

P_{O_2} = Partial pressure of oxygen at equilibrium.

For a reaction to occur the oxygen partial pressure must be greater than at this equilibrium value and ΔG must be less than 0[9]. This can be used to predict the presence and expected composition of an oxide scale by plotting the activities of an oxide at various temperatures to form an Ellingham diagram as shown in figure 2.3. The formation of an oxide on the surface can protect the underlying metal from further oxidation and thus can be a beneficial factor[9].

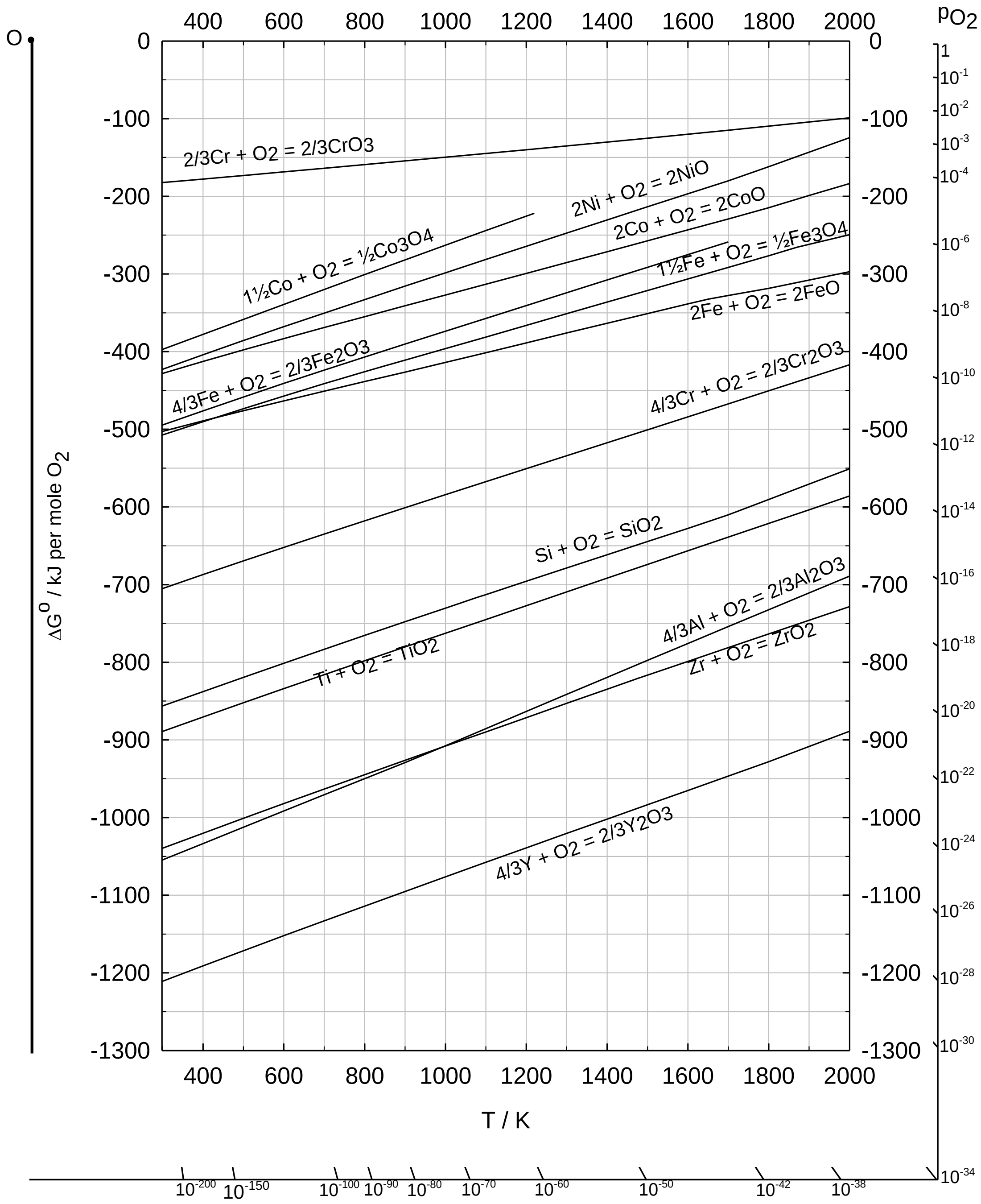

Figure 2.3: Ellingham diagram of some relevant oxides modified from Birks and Meier[9].

These diagrams give an indication as to the stability of an oxide formed on an alloy and can be used to design alloys to form a protective oxide layer through selective oxidation of a particular solute[9]. Careful selection of the element to be oxidised is important to ensure that the desired oxide formed is more stable than the oxide of the parent metal in the alloy. Therefore for nickel-based alloys the formation of an alumina oxide would be relatively easy as the stability of alumina is considerably greater than that of nickel oxide. However for other base metals such as titanium the formation of solely alumina would more problematic as the stabilities are similar therefore a mixed oxide scale would likely be formed. In the case of the oxides shown in figure 2.3, we can see that all of these selected oxides are stable in the temperature range shown and that the majority of the oxides shown particularly chromia and alumina are more stable than nickel oxide. However the stability of an oxide at temperature does not mean that an oxide is good for oxidation or corrosion protection. An equally important factor is the growth rate of the oxide[9].

2.4 Selecting Alloy Compositions for Oxidation Protection

With this information it is possible to design alloys which form a protective oxide scale through selective oxidation. Taking the information from figure 2.3, in principle it could be possible to form a protective oxide scale on a nickel based alloy from any of the elements listed as they form a more stable oxide than nickel[9]. However it is the rate of oxide growth which is equally important, for an ideal protective oxide this must be as low as possible. Therefore those oxides with the lowest K_p values are those, which form the best protective oxides[9].

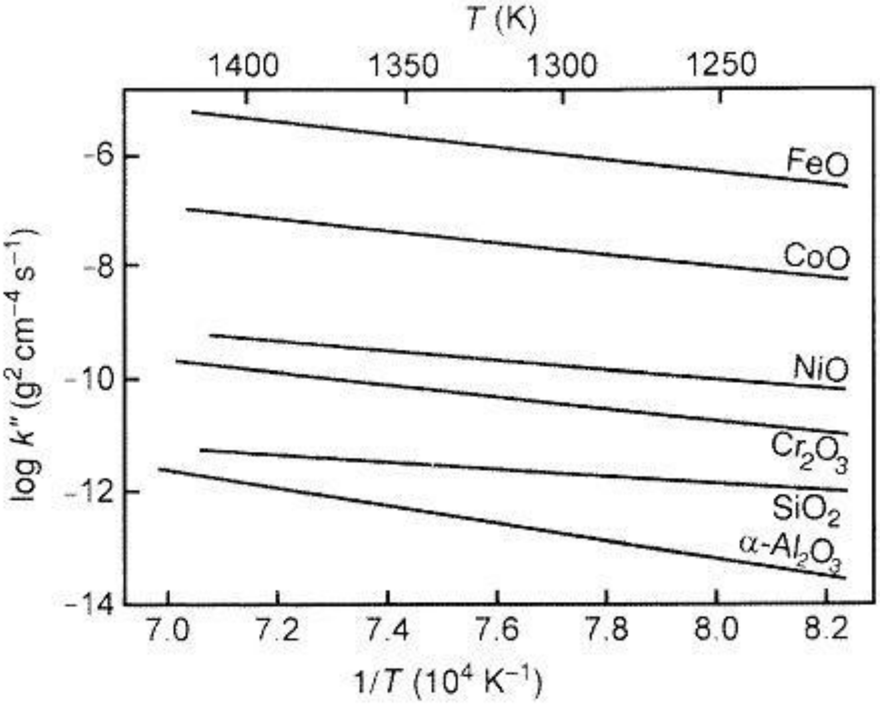

Figure 2.4: Parabolic rate constants for the growth of some oxides[9]

We can see from figure 2.4 that the oxide with the lowest growth rate is α-alumina followed by silica and chromia. This large variation in growth kinetics follows closely with the concentration of point defects in the oxides, with those with higher concentrations having a faster growth rate[9]. Silica has the potential to provide a protective oxide layer at temperatures in excess of that for alumina and has been used on carbon materials at up to 1800°C[9]. However silica can be susceptible to breakdown in moist atmosphere and so is used preferentially in dry atmospheres[9].

2.4.1 Oxidation of Chromium-Bearing Alloys

Chromia is an important protective oxide at temperatures between 600-900°C, and has been widely used in applications such as catalytic converters[9]. At high temperatures in excess of 950°C and in a high flow rate gas, chromia has been shown to convert to the volatile gaseous oxide CrO_3 and as such its use is limited to temperatures below these conditions[9]. Therefore for applications above 950°C alumina is the protective oxide of choice.

2.4.2 Oxidation of Aluminium-Bearing Alloys

With the knowledge that an alumina protective oxide is the scale of choice for high temperature applications it now follows that the fundamental requirement for protection of an alloy from oxidation is to provide enough of the selected element to form a protective oxide scale[9]. The high density of alumina means that the numbers of available vacancies for diffusion are low and thus the growth rate of the oxide is correspondingly low. In addition however to forming the oxide it is important for the alloy to have a sufficient reservoir of the aluminium to enable re-healing of the scale should cracking or spallation occur[36]. However it is important to balance this consideration with maintaining the mechanical properties. In the case of the Ni-based alloys which are the most widely used for high temperature turbine applications aluminium is an important alloying element in the strengthening of the γ' phase of the alloy[37]. However additions of heavier elements such as tungsten, tantalum and ruthenium have meant the concentration of aluminium in these alloys is typically around 5-6wt%, which is considered to be the minimum requirement for the formation of an alumina scale[37]. This is also aided by the addition of chromium, this is shown to increase the likelihood of forming an alumina protective oxide through providing nucleation points of chromia which the alumina forms around[38]. This process is known as the gettering[10] effect. However other theories exist about the beneficial effect of chromium in alumina formers such as determining the growth rate of transient oxides through formation of a chromia layer[39, 40]. Studies have shown that the minimum amount of aluminium required for re-healing of an oxide scale is ~3wt% although this can be as high as 6wt% without the addition of chromium to the alloy[38]. This is demonstrated schematically in figure 2.5 which shows the composition of the oxide scale formed at various alloy aluminium and chromium concentrations.

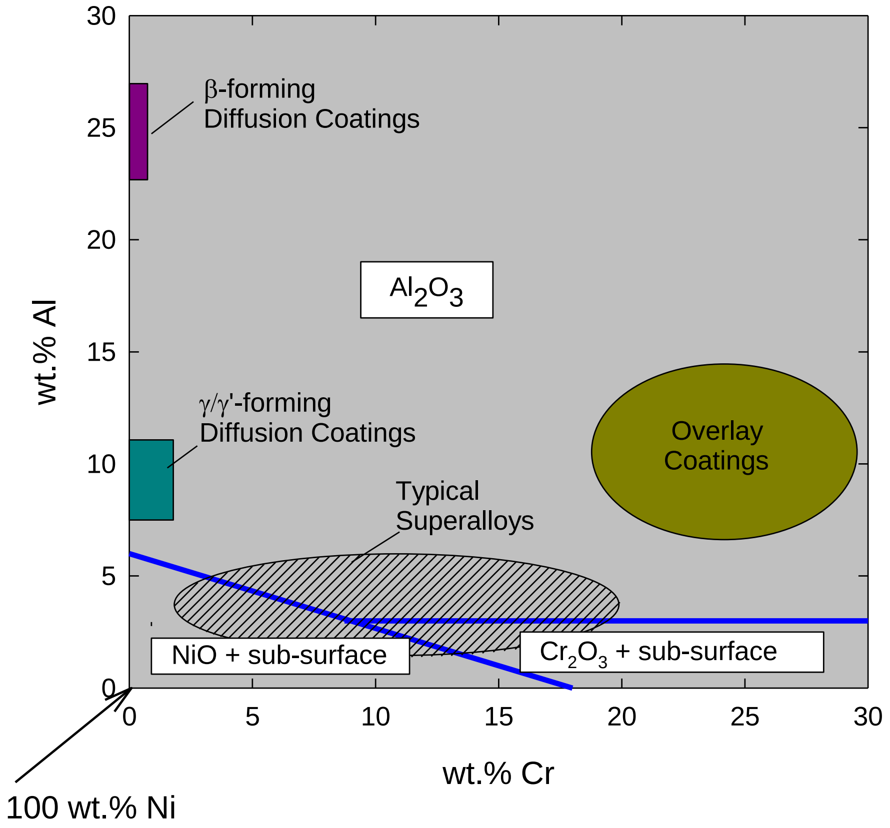

Figure 2.5: A schematic map showing the type of oxide formed in the NiCrAl system at temperatures between 1000-1200°C [41]

We can see from figure 2.5 that the typical superalloys, as used in high temperature applications, typically do not have sufficient aluminium to form a continuous alumina scale. Thus mixed oxides of nickel, chromium and aluminium will form. This therefore requires the addition of a high aluminium/chromium coating to be applied to increase the surface concentration of aluminium to allow a continuous alumina scale to form initially and for rehealing of the scale should it become damaged.

2.5 Aluminium Depletion

Selective oxidation of the aluminium to form a protective scale leads to the depletion of aluminium in the alloy. Figure 2.6 shows schematically the depletion profile of aluminium in a typically used alloy (dotted line) after the formation of an alumina scale.

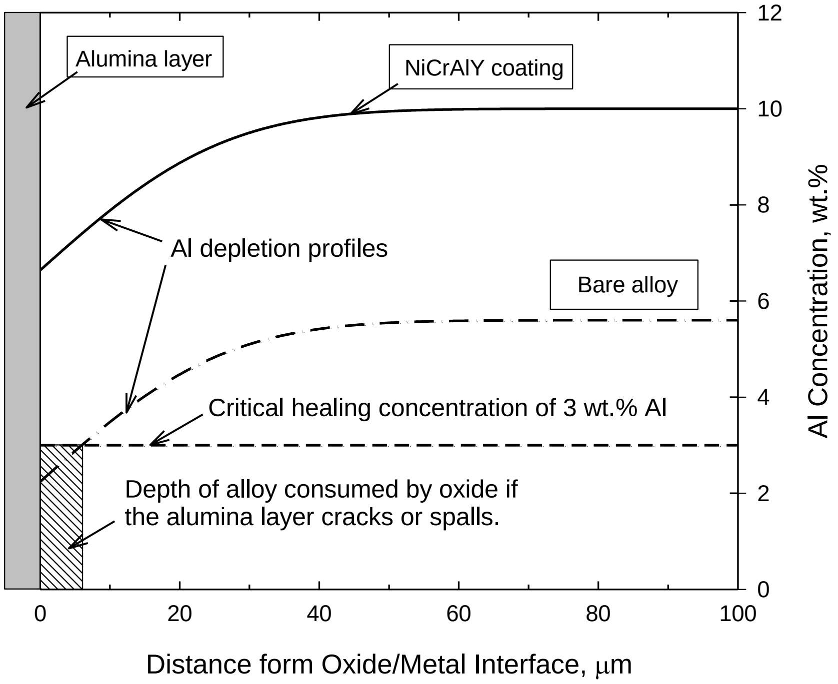

Figure 2.6: Depletion profile for aluminium during the formation of an oxide scale [36].

From this depletion profile it can be seen that for a typically used alloy the concentration of aluminium local to the scale falls below the 3wt%[38] required for re-healing after the formation of the oxide scale. This leads to the formation of rapidly growing mixed oxides, upon scale cracking, typically Ni containing, which consumes a greater depth of the alloy surface than the formation of alumina would. This then demonstrates the requirement of the application of an aluminium rich coating to the surface of the alloy to increase the size of the aluminium reservoir. Figure 2.6 also shows the depletion profile for an applied aluminium rich coating (solid line) and demonstrates that increasing the aluminium content to around 10wt% provides an aluminium reservoir to enable re-healing of the oxide. These coatings are therefore widely used to protect the bare alloys without having to increase the alloy aluminium content and compromise mechanical properties. These will be covered in the next chapter.

2.6 Oxidation of NiCoCrAlY Coatings

As has been discussed above, for oxidation protection at high temperatures of >900°C, a fully dense α-alumina scale is the preferred oxide due to its slow growth and dense structure. Also as seen in figure 2.6 a minimum concentration of 3wt% Al is required to provide a re-healing dense alumina scale on the surface, this assumes a bond coat chromium concentration of >10wt%[38]. Without the addition of chromium the critical aluminium content is 6wt%, this effect is likely due to the initial formation of chromia at the oxide metal interface which promotes alumina growth[38]. A typical NiCoCrAlY alloy will contain around 10wt% Al to provide an increased reservoir for rehealing of the oxide scale should any cracking occur.

Reactive elements such as yttrium, as used in these coatings, are added to these coatings, typically to aid adherence of the scale to the bond coat free surface[42-47]. Typically around 0.05-0.1wt% Y is added and is shown by several studies to increase scale adhesion and decrease the oxidation rate of the coating[45, 48-51]. However increasing the amount of yttrium added causes the formation of oxide pegs, typically yttrium aluminium garnet (YAG-$Y_3Al_5O_{12}$)[52]. These oxide pegs increase the apparent growth rate of the oxide, compared to lower additions of yttrium, when measured by mass gain due to their higher mass than alumina[45]. It has also been shown that having high yttrium concentration causes segregation of the yttrium to the oxide grain boundaries. This could increase the diffusion of oxygen along these grain boundaries and so increase the oxidation rate, compared to lower concentrations of yttrium[48, 49, 53]. The increase in adhesion of the oxide formed on a bond coat with yttrium addition was originally thought to be a consequence of mechanical keying provided by the formation of the oxide pegs[54]. However other studies have shown that additions of yttrium can increase scale adhesion without the formation of oxide pegs. Additionally some studies have linked the large size of YAG particles to increasing the susceptibility of the oxide to spallation[55, 56]. It is currently not known with certainty the effect that oxide pegs have on coating lifetimes.

2.7 Oxide Scale Stresses

The growth of a protective oxide scale on a metal surface at temperature is a beneficial property of the alloys and coatings used at elevated temperatures. However for the oxide scale formed to be beneficial it is important that it can withstand stresses both external from an applied loading during use and also internally produced stresses, which form during the oxidation processes. These oxide growth stresses can arrive from a number of areas, some of which will be discussed in the remainder of this section.

2.7.1 Volume Differences

The growth of an oxide scale on a metal surface naturally consumes part of the metal substrate surface in its formation. In addition the specific volume of the oxide forms rarely equals this volume of metal consumed. It is possible to quantify this as a ratio known as the Pilling-Bedworth ratio, which is defined below[18].

$$PBR = \frac{Vo_{ox}}{Vo_m} \tag{2.10}$$

PBR= Pilling-Bedworth Ratio

Vo_{ox}= Volume of Oxide formed

Vo_m= Volume of metal consumed to form that volume of oxide

For most metals, the volume of the oxide is greater than the volume of metal consumed, for example, a PBR of 1.28 for alumina and 2.05 for chromia, but there are cases (MgO, for example) where the PBR is < 1. For some years[57], it was thought that a volume expansion would result in compressive oxide growth stresses and a volume contraction, tensile growth stresses. However, it has long been recognised that this early view is simplistic and that stress development depends on a number of factors, such as the location of oxide formation and stress relaxation processes within the scale and substrate. If the oxide is formed at the oxide gas interface, for example, then no compressive stresses will form as the volume difference is shown in the oxide thickness[58]. Similarly, the formation of new oxide at the oxide/metal interface on a flat surface will not develop growth stresses either[58]. The situation is different for oxide growth on curved surfaces where growth stresses can develop for oxide formation at either interface[58].

2.7.2 Epitaxial Stresses

During initial nucleation of the oxide scale on the metal surface it is feasible for stresses to develop within the oxide due to differences in the lattice parameters between the oxide grains and the metal structure[9]. For oxides where the PBR value is >1 and the accommodation of the change in lattice parameter is within the oxide via dislocation formation, as for thin oxides, a compressive stress is generated[58]. Likewise for oxides with a PBR value of <1 a tensile stress is generated[58]. However modeling of this process by Fromhold[59] has suggested that the stresses generated decrease exponentially with increasing distance from the metal/oxide interface. Thus this effect is only likely to play a major role in thin oxides, this has been demonstrated for copper oxides[60], where these stresses have only been found within 30nm of the interface. It is unlikely to play a major role in total growth stress of a thick oxide layer for this reason.

2.7.3 Thermal Stresses

The growth stresses above are formed in the oxide during formation at the oxidation temperature. Considerable stresses, however, are also formed upon cooling of the metal and oxide due to the difference in thermal expansion coefficient between the metal and the oxide. This difference can often be as large as 4 times, for example for a CMSX4 superalloy a typical value would be 2.0x10^{-5} K$^{\grave{}1}$ compared to 7.9x10^{-6} K$^{\grave{}1}$ for α-alumina. The strain energy generated due to this thermal expansion mismatch can be calculated using equation 2.11[61].

$$W^* = E_{ox} h (1 - \nu_{ox})(\Delta T)^2 (\Delta \alpha)^2 \tag{2.11}$$

W*= Strain Energy
E_{ox}=Young's Modulus of the oxide
h=Oxide thickness
ν_{ox}= Poisson's ratio of the Oxide
ΔT= Change in Temperature
Δα= Difference in thermal expansion co-efficient

Using values of,
E=367GPa
ν_{ox}=0.3
ΔT= 1000K
α-Alumina = 7.9x10^{-6} K$^{\grave{}1}$
CMSX-4 Substrate = 2.0x10^{-5} K$^{\grave{}1}$

For an oxide thickness at 1µm the strain energy generated between an alumina oxide and superalloy substrate would be 37.61Jm^{-2}. This is far in excess of the fracture energy, 0.66Jm^{-2}[62] of the alumina on a Ni substrate and so should there be no mechanism of relaxation for this strain energy cracking will occur at the scale/metal interface.

3 OXIDATION PROTECTION FOR INDUSTRIAL GAS TURBINE APPLICATIONS

Early gas turbine engines operated at temperatures around 700°C due to the creep rupture strength of the materials. These engines created around 50 times less thrust than a typical modern engine[63]. The increase in thrust generated can be partly attributed to a doubling of the engine inlet temperature[63]. This increase in temperature has led to the development of newer alloys which have the capability of withstanding temperatures exceeding 1100°C. However these alloys are often far more prone to both type I and type II hot corrosion which initially limited their use[64, 65]. A solution to this problem came in the development of coatings which protected the substrate alloy and thus improved its hot corrosion resistance[65]. Further developments in these coatings led to the further application of a ceramic layer onto the original metallic coating to reduce the exposure temperature of the alloy[66]. These developments have led not only to an increase in engine inlet temperature but also to a reduction in the required cooling air to the engine components thus not only increasing the generated thrust but also the engine efficiency[63, 67-71].

The turbine alloy is optimised for mechanical properties, however the elements which provide these benefits conflict with the requirements for oxidation protection[72]. To overcome this coatings have been developed and are used in these applications[72]. These coatings can be broadly split into 2 categories, overlay and diffusion, this chapter will describe the major overlay coatings used as they are specific to this project; however diffusion coatings are widely used and will be briefly described.

3.1 Overlay Coatings

These coatings are deposited onto a substrate surface, with a minimal amount of interaction with the substrate; therefore the compositions of the coatings can be more carefully controlled[7, 72, 73]. Additionally these types of coatings can be much more flexible in terms of composition and allows for the addition of elements that cannot be applied to the substrate in the required quantities[7, 72, 73]. For high temperature applications as typically found in turbine blades these coatings are applied as a bond coat onto the substrate, with a ceramic topcoat applied afterwards to provide thermal protection as can be seen in figure 3.1. The topcoat is described later in section 3.4.3

Overlay bond coats traditionally have been formed from MCrAlY materials where the M is usually iron, nickel and/or cobalt[72-74]. These coatings do form large Al reservoirs and dense alumina layers. They tend to be less dense than the diffusion coatings because of the techniques used to apply them, and internal oxidation can occur within the coating[74].

Typical application processes involve physical techniques such as sputtering, ion plating, evaporation and most widely used is various spraying techniques[72]. Thermal spraying of coatings has been widely used for several decades and provides a relatively inexpensive way, equivalent to a platinum aluminide diffusion coating[72], of applying thick coatings of almost any composition to complex shapes. The main process involves heating a powder or solid substrate material[3], e.g. a wire, by electrical resistance or fuel burning. This molten/soft mixture is accelerated to a substrate using a gas stream[3], these coatings are termed air plasma sprayed(APS) coatings. Several variations of this technique exist which alter the properties and cost effectiveness of the coating being applied, some examples include Low Pressure Plasma Spraying (LPPS) where the coating takes place under a reduced pressure atmosphere, typically 5-7x10^{-3} Pa[7, 72, 73]. This coating type is typically used with coatings containing reactive elements such as Al or Y[72]. Vacuum Plasma Spraying (VPS) is carried out in a very low pressure inert atmosphere using the same technique to produce plasma from electric current. This technique produces dense coatings with no oxidation of powder particles so is ideal for powders containing highly reactive elements[3]. High Velocity Oxy Fuel(HVOF) involves the burning of a high pressure, oxy-fuel mixture into which the coating powder is added[72]. The burning mixture provides both the heat and velocity for coating. This can produce very thick coatings of >100µm that are typically very dense due to the high flow rate of the fuel and powder, typically 200m/s[72]; a full description of this coating type can be found in section 3.3.1. A similar technique using a fuel/oxygen mixture such as acetylene/oxygen which is detonated and accelerates the powder to the target substrate[3]. This method can produce temperatures of several thousand degrees and very high velocities to produce a coating of high density and strength.

More recently, a relatively new technique has been used, which involves using electron beam physical vapour deposition (EBPVD) to apply either a single or dual phase bond coat. This technique is described below in section 3.3.2. This coating is densified after application to provide a dense evenly distributed bond coat with a smooth interface as can be seen in figure 3.1.

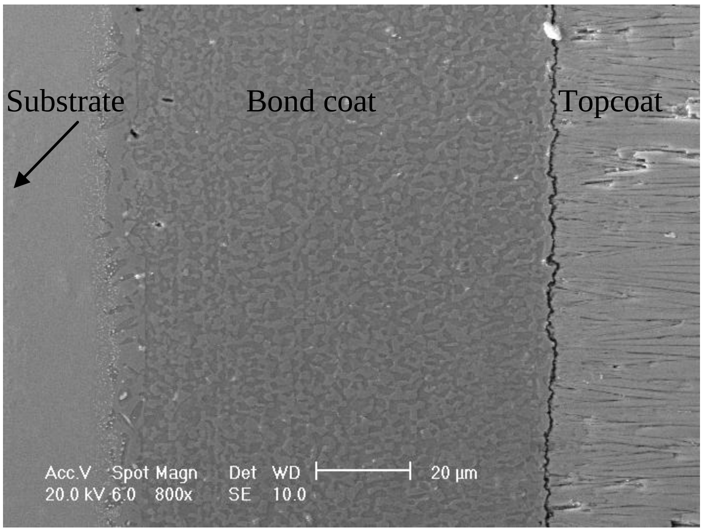

Figure 3.1: A scanning electron micrograph of a typical MCrAlY bond coat applied using the EBPVD technique.

3.2 *Specific Coating Application Methods*

This project has examined two coatings applied by different coating methods, namely HVOF and EBPVD. These are two widely used and important coating methods and are described below.

3.2.1 High Velocity Oxyfuel (HVOF) Spraying

In this technique a fuel and oxygen mixture is burnt producing a hot high pressure stream of gas. Powder or ingot materials of the coating are then fed into this stream either at a nozzle or into the combustion chamber and are then accelerated toward the substrate[3, 7, 72, 73, 75]. The heat of the combustion softens or melts the powder or ingot so that it splats onto the substrate to form an even coating[73, 75], figure 3.2 shows a schematic diagram of the set-up.

The temperature required to soften these coating materials can cause additional complications and so cooling in the form of a water jacket is required for the spray gun[75]. However this can be alleviated if the combustion is carried out remotely from the nozzle and compressed air is used in the combustion mixture to both accelerate the mixture to the nozzle and to cool the apparatus[75]. The coating can be fine tuned to the application by the alteration of several factors including the oxy-fuel mixture which adjusts both the heat and spray velocity. Also the feed powder size plays an important role in determining the coating structure[75]. This type of coating forms a near dense, well bonded coating with a relatively high degree of accuracy and due to its nature it can be carried out on complex, large components cost effectively[72, 76].

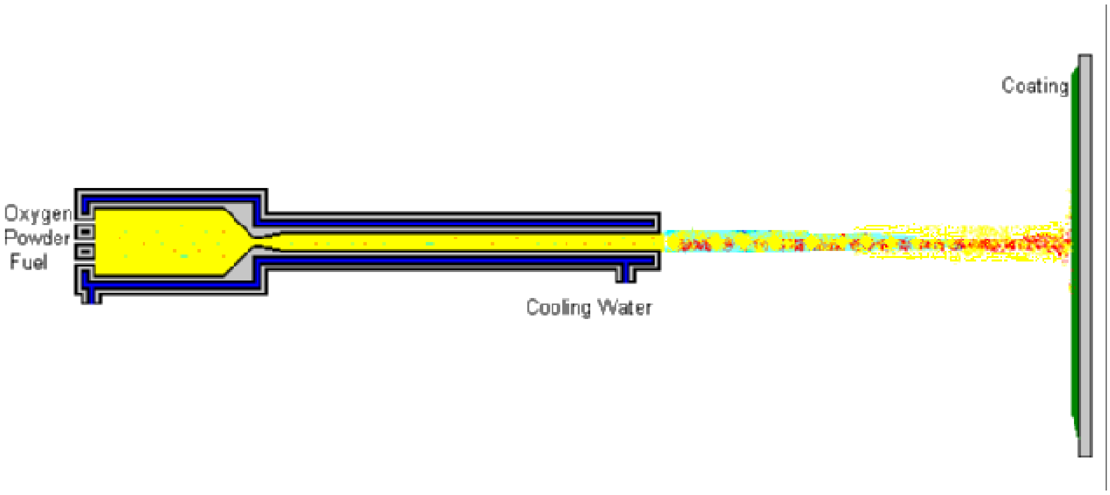

Figure 3.2: Schematic diagram of a HVOF coating set up [77].

3.2.2 Electron Beam Physical Vapour Deposition (EBPVD)

In this technique the substrate to be coated is placed into a vacuum chamber at a pressure of 10^{-2}-10^{-4}Pa and located onto a movable stage[73]. Within the chamber are several electron guns and source ingots of the material to be deposited onto the specimen or component[73]. After evacuation the ingots are bombarded with focussed electrons at around 20-30kV. This heats the ingots and forms a molten pool on the surface from which a vapour of the ingot material is formed in the vacuum. This vapour is directed onto the substrate material in a rotation fashion to form the correct composition[72, 73]. The processes of condensing the coating on the substrate is a line of sight process between the electron beam and the ingot as shown in figure 3.3, and so column like grains are formed on the substrate surface[1, 72, 73]. After coating these are densified using a shot blasting type process to remove any vertical grain structures. This type of coating forms an evenly distributed dense structure for metallic coatings. Additionally the deposition rate is related to the incident beam power and as such a very high deposition rates, in excess of 25μm/min can be achieved which is important for industrial applications[73]. However this process is a line of sight process in a very controlled atmosphere and as such the substrate size and shape are limited. This technique is used widely for the production of thermal barrier coatings due to its tight control on composition and high deposition rate[3, 72, 73].

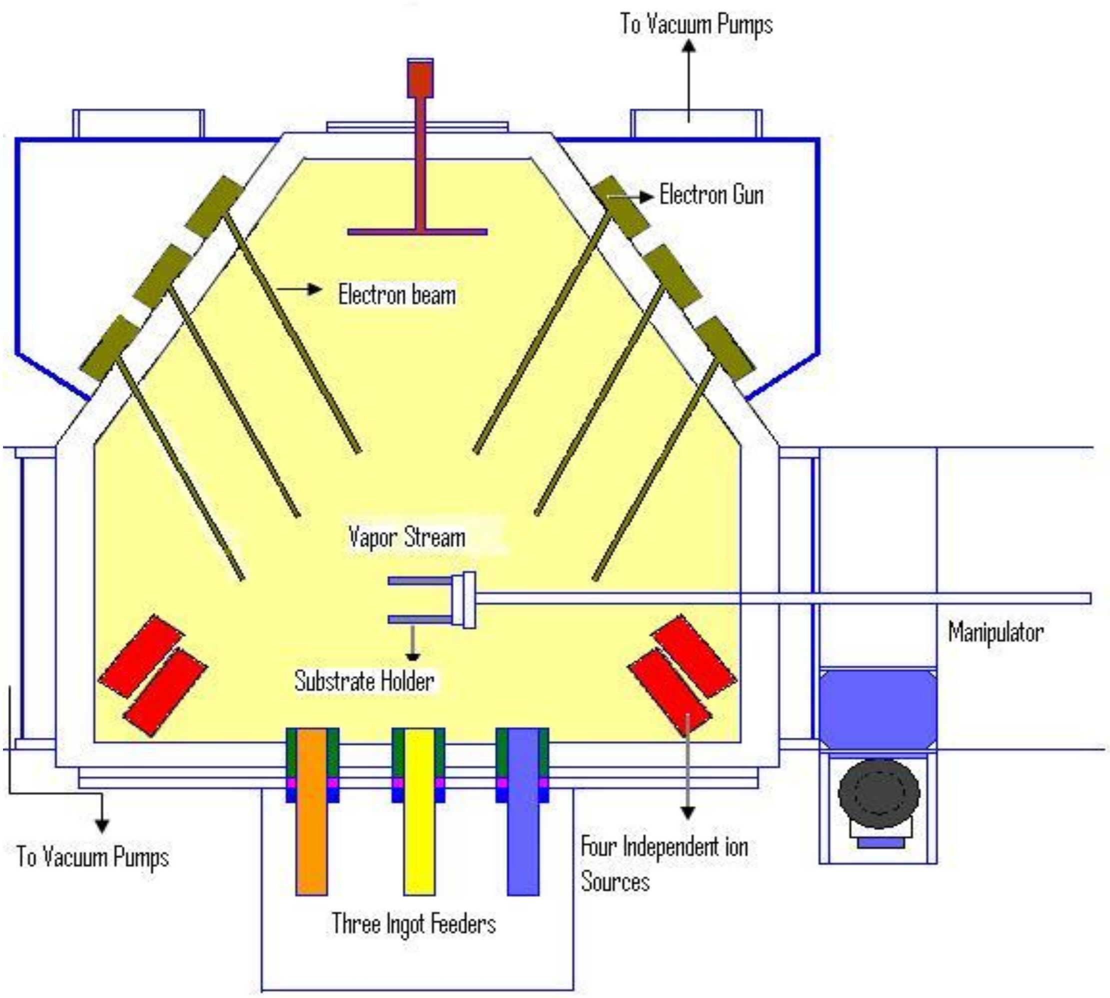

Figure 3.3: Schematic diagram of an EBPVD coating set-up.[78]

3.3 *Diffusion Coatings*

Although not studied as part of this project this type of coating is widely used for aerospace applications and so it is important to mention briefly here[3, 72, 73]. This type of coating is produced by the addition to the surface of the substrate of elements to improve the resistance to oxidation but also to maintain some of the substrate mechanical properties[1, 3, 63, 72, 73]. Typically this involves the diffusion into the surface of aluminium, chromium or silicon depending upon the application that has been deposited on the surface of the substrate[1, 3, 63, 72, 73]. The addition of these elements in the surface provides a large reservoir for the selective oxidation and thus formation of a protective oxide scale[1, 3, 63, 72, 73]. A large reservoir of the element to be oxidised is required to enable re-healing of the oxide scale due to damage or spallation. Diffusion coatings are usually manufactured by vapour deposition of the required element either within a pack or above pack. It is important to note that as this is a chemical vapour process at atmospheric pressure, it is not line of sight and as such allows coating of complex component shapes[1, 3, 63, 72, 73]. However other methods such as slurry coating and hot dipping may also be used but will not be discussed further here[1, 3, 63, 72, 73].

3.3.1 Chemical Vapour Deposition (CVD)

A typical example of this process involves immersing the substrate material in a series of powders which include Al[79], either pure or as an alloy, an activator, usually a halide, and an inert filler- usually alumina[79]. Upon heating to temperatures around 1000°C, the halide activator reacts with the Al to form a volatile aluminium halide with high Al content[79, 80]. The halide formed has a higher aluminium activity than the substrate so diffuses and deposits on the substrate surface[79, 80]. It then reacts with the surface and the aluminium is released and diffuses into the substrate[79, 80]. The coating process takes several hours depending upon the desired coating thickness and post coating heat treatment may be required to remove any brittle δ Ni_2Al_3 phases formed[79].

3.3.2 Typical Coating Materials Used for Diffusion Coatings

Pt-aluminide diffusion coatings are the typical diffusion coating used for aerospace applications[3, 7, 72, 73], they are usually predominantly β phase but some phase transformation can occur at temperature depending upon the alloy composition[1, 74]. These coatings are now usually created by platinum plating the component, subsequently a chemical vapour deposition (CVD) pack aluminising process at approximately 1050°C is performed for around 10 hours[79]. The high temperatures and long time of the process helps to provide a large aluminium store in the coating and also to maintain the mechanical properties of the substrate[79]. The existence of refractory elements in the substrate, their diffusion into the coating and also loss of Al through diffusion into the alloy substrate can impair the function of the bond coat[81-84]. One function of the platinum may be to inhibit diffusion of the refractory elements from the substrate but its main role is to stabilise the aluminium within the modified (Ni,Pt)Al β phase formed during this coating process, it is thought to achieve this through having a strong affinity with aluminium[81].

Newer coatings omit the aluminising process described above and instead rely upon the plating and diffusion of a platinum layer, these form a platinised γ/γ' bond coat [85, 86]

3.4 The Thermal Barrier Coating (TBC) System

For high temperature turbine applications a combination of a bond coat providing oxidation protection and a topcoat providing thermal protection is required. The typical structure consists of the overlay or diffusion bond coat applied to the substrate material. Some interdiffusion will occur at this interface with typically aluminium diffusion into the substrate and nickel diffusion out, leaving behind heavy element precipitates in the form of an interdiffusion zone(IDZ)[81, 84]. The size of the IDZ and its effects on the substrate mechanical properties will vary with the coating type, with overlay coatings providing the least interdiffusion in most cases as by their nature they are independent of the substrate[7]. Despite this some interdiffusion is desirable for adhesion of the bond coat and so interdiffusion does occur[7]. The exposed surface of the bond coat will form ideally a stable, protective, slow growing thermally grown oxide(TGO), which will increase in thickness with increasing exposure time[73, 87]. For high temperature applications the TGO will usually be α-alumina as discussed in section 2[1]. This TGO is first formed as part of the coating process as described in section 3.2 and 3.3. Onto this TGO the ceramic topcoat is applied to form the thermal barrier coating system as shown schematically in figure 3.4.

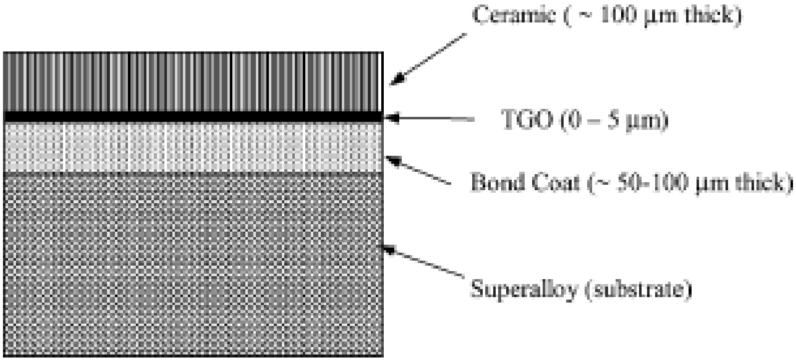

Figure 3.4: Schematic of a Typical TBC Structure [88]

3.5 Ceramic Topcoats

The application of a thermal barrier coating provides thermal protection of the substrate material from the atmosphere. This then allows for a reduction of internal cooling of up to 6% which corresponds to a significant increase in component efficiency[7, 68, 89]. It therefore requires very specific properties. It has a low thermal conductivity to create a thermal gradient[68, 89]. It must have good strain tolerance due to the differences in the thermal expansion of the substrate, bond coat, TGO and topcoat during operation[68, 89]. The topcoat is also required to be microstructurally and chemically stable at the proposed working temperature and at room temperature, over a period of time. In addition it must also be chemically compatible with, and able to adhere to the bond coat and TGO[68, 89].

3.5.1 Typical Ceramic Materials Used

The main material used for the topcoat in these systems is zirconia containing 7%± 1wt% yttria which stabilises the zirconia (YSZ) into the tetragonal phase and prevents the large volume change associated with its conformational change at temperature[74, 89]. This material has proven to be very thermally stable and strain resistant in temperatures up to 1200˚C[74]. However other materials have been considered for thermal barrier coatings at lower temperatures, including mullite. Some studies have shown that this material could be a viable alternative to zirconia at lower temperatures[89]. It is argued that mullite experiences lower stress relief than zirconia and so compressive stresses could be maintained within the coating[89]. The development of tensile stresses and associated cracking would then be limited. However mullite does not possess the same mechanical properties and more importantly thermal properties that zirconia has at high temperatures, including its low thermal conductivity, κ [89], with mullite having a typical κ of 3.2 $Wm^{-1}K^{-1}$ compared to 1.5 $Wm^{-1}K^{-1}$ of zirconia[90, 91].

For future use in high temperature applications two potential materials are being considered. The first is a doped variant of the existing YSZ technology with the addition of rare earth oxides (REO) such as Yb, Er, Gd and Nd[74, 92]. These appear to offer considerable advances in terms of thermal conductivity however there are currently issues with compatibility with the alumina TGO[74]. The second material is pyrochlore-type zirconates ($M_2Zr_2O_7$) which have shown considerably favourable thermal conductivity values of typically $1.3Wm^{-1}K^{-1}$[93]. However variations in manufacture have been found which create difficulties in analysing the results[74].

3.5.2 Topcoat Application

The material most widely used for the formation of a ceramic topcoat is YSZ, which has been used in this project. Other materials often require different application techniques but will not be discussed here.

To date there are only two main routes for depositing the yttria stabilised zirconia (YSZ) topcoats. Each have their own unique advantages and disadvantages both in terms of performance and ease of modification[74, 89]. The main deposition routes are electron beam physical vapour deposition (EBPVD) and air plasma spraying (APS).

EBPVD

Application and densification of the metallic bond coat provides a thin ~1µm thick alumina oxide on the surface of the substrate[73]. This preformed alumina aids the adhesion of the ceramic applied on top[73]. The YSZ topcoat is then applied using the procedure described in section 3.2.2 and is the same procedure used to apply the metallic bond coat tested in this study[73]. However for the production of a topcoat the deposition temperature is raised to 1000°C and a high pO_2 atmosphere is used. Also the densification process required for a dense bond coat is omitted and a columnar structure is therefore produced. Figure 3.5 shows an electron micrograph of the structure produced.

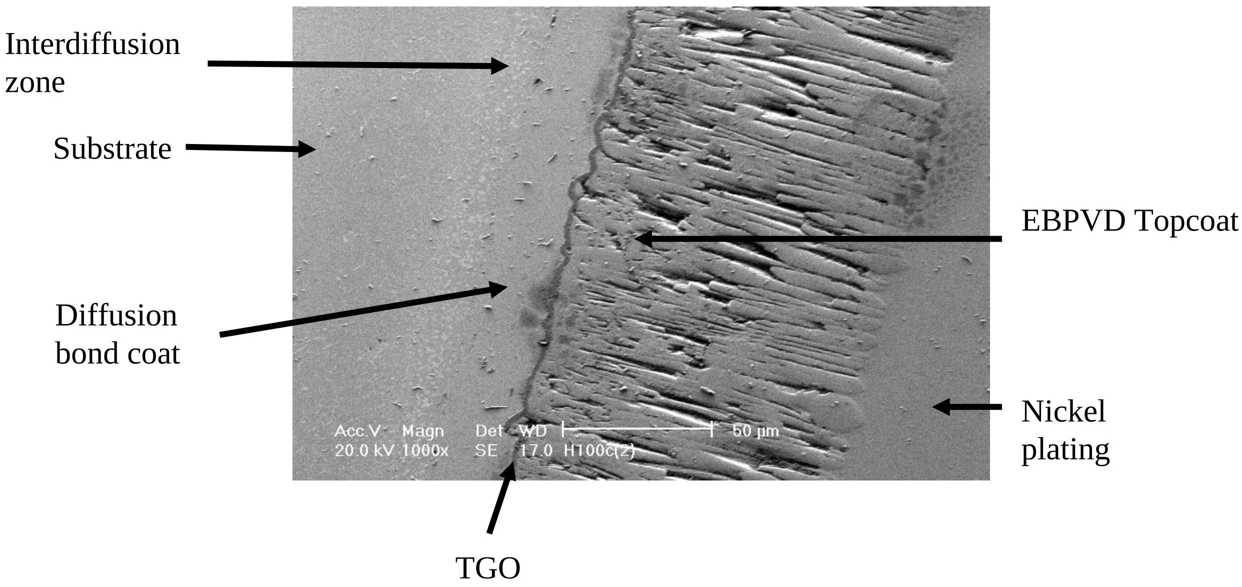

Figure 3.5: Electron micrograph showing a section through a TBC heat-treated at 1100˚C for 100hrs in air, showing the substrate, Interdiffusion zone, diffusion bond coat, TGO and EBPVD topcoat.

APS

As with the EBPVD process this is a line of sight technique[1, 7, 63, 72, 73, 76] in which powder particles ~60µm in diameter are passed through plasma created from Ar and H_2[7]. The semi-molten particles impact onto the substrate surface creating a characteristic horizontally layered structure of the YSZ material[73]. Figure 3.6 shows a typical structure of an air plasma sprayed coating in a TBC system.

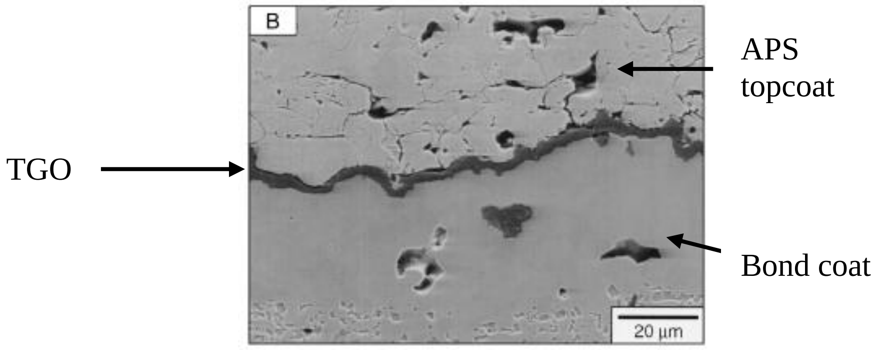

Figure 3.6: Scanning electron micrograph of an APS topcoat TBC oxidised for 216hrs at 1010˚C showing the bond coat, TGO and topcoat[94].

3.5.3 Properties of the Topcoat

EBPVD coatings are widely used because of the excellent durability when compared to APS coatings[74]. This is largely due to the open columnar grain structure created by this method, which is thought to allow for considerable strain relief of the topcoat[74]. However a collection of in house and literature failure times has shown that there is little difference in failure times associated with either of these coatings methods; this will be discussed later in section 8.7.8. APS coatings while not as durable do offer considerable improvements in thermal insulation with conductivity below 1 $Wm^{-1}K^{-1}$compared with typical EBPVD values of 1-2 $Wm^{-1}K^{-1}$[74, 89]. Both of these coatings do offer considerable thermal stability and strain tolerance at temperature and upon cooling as they are manufactured from the same material[74]. However, the columnar structure of EBPVD topcoats does mean that they are more tolerant to strain then APS coatings. Although both methods are now well established EBPVD topcoats are somewhat more expensive to create due to a large capital outlay in equipment and difficulties in applying the topcoat to large specimens when compared to APS topcoats.

4 DEGRADATION AND FAILURE OF PROTECTIVE COATINGS

One of the major stumbling blocks with the introduction of these coatings into service has been a continued problem with their endurance[67-71]. Considerable research effort over the last 40 years has aimed at discovering how and why these coatings fail, both prematurely and after considerable life. Many plausible mechanisms have been developed over the years and it is increasingly likely that most if not all of these methods have a part to play in the failure of these coatings, with some having more of an effect in particular coating systems than others.

Failure of the topcoat can be potentially catastrophic to the component and the remainder of the engine, as it leads to exposure of the bond coat to extremes of temperature and environment beyond its capabilities[64], leading to increased oxidation rates. This leads to failure of the bond coat and eventual failure of the component soon afterwards. Therefore the use of these coatings has been restricted both in the time and temperatures at which they are used[67-71]. To make these components more economically viable it is important to be able to understand their failure modes and so try to improve their endurance. Some of the main failure modes are described below, but it is important to remember that it is unlikely that these modes act alone, but in fact work together in causing coating failure.

4.1 Substrate/ Coating Interactions

Diffusion of elements at the substrate/ coating interface is a well known phenomenon and can have considerable impact upon the coating life. For example the coating contains considerably more of the reactive elements than does the substrate. These reactive elements, mainly tungsten, rhenium, tantalum and molybdenum are present in the substrate to increase the mechanical properties[81]. Many high temperature coatings have high levels of aluminium to form a stable alumina scale with a reservoir for re-healing due to the substrate having an insufficient amount of aluminium for protective scale formation. However the aluminium from the coating can lead to the formation of brittle topographical close packed(TCP) phases such as σ and μ, which can be a site of fracture in the superalloy[81, 84, 95]. These phases are rich, in comparison to the coating and substrate, in refractory elements such as rhenium, tungsten and tantalum. The solubility of these elements in the substrate is very low and the inward diffusion of aluminium from the coating leads to their precipitation [81, 84, 95]. These phases have been observed in a number of studies with a range of coating types[81, 84, 95]. The addition of platinum however appears to block the formation of these TCP phases and also the diffusion of reactive elements to the bond coat surface, where they could have a detrimental effect on the protective oxide[82, 83, 95]. In addition diffusion of the reactive element into the substrate also depletes the reservoir available in the bond coat which after lengthy exposure can lead to breakaway oxidation.

4.2 *Buckling*

Buckling occurs when the bond between the TGO and bond coat is poor, due normally to the presence of voids or impurities at the interface[96]. Differences in the thermal expansion co-efficient of the TGO, topcoat and bond coat lead to compressive stresses being set-up in the TGO during cooling[96]. This can lead to delamination at the TGO/bond coat interface[97] as shown schematically in figure 4.1 and a typical example is shown in figure 4.2. The exact mode and location of buckle propagation depends upon the bonding between the oxide and substrate and also on the mechanical properties of both layers, table 4.1[96, 98].

Table 4.1: Failure modes of a thin oxide film under a compressive stress, from [96] after work by [98]

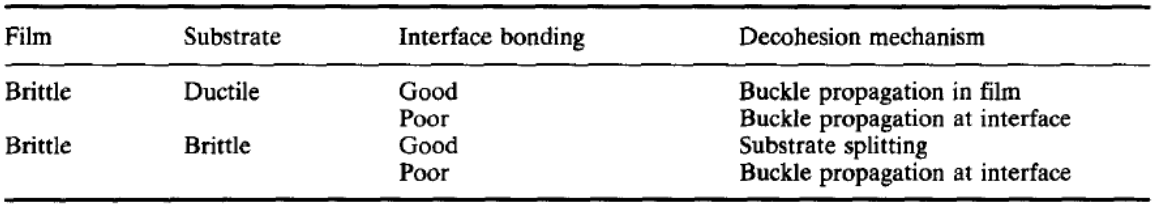

Film	Substrate	Interface bonding	Decohesion mechanism
Brittle	Ductile	Good	Buckle propagation in film
		Poor	Buckle propagation at interface
Brittle	Brittle	Good	Substrate splitting
		Poor	Buckle propagation at interface

Even with an area of decohesion present between the oxide and substrate buckling may not occur as the size of the decohesion must be such that sufficient stress is generated within the coating. This critical stress can be represented by equation 4.1 below, assuming solely plastic deformation and shows clearly that the ratio of decohesion size and oxide thickness is an important criteria to buckle propagation[61, 96].

$$\sigma_c = \frac{1.22E_{ox}}{(1-\nu_{ox}{}^2)}\left(\frac{\xi}{R*}\right)^2 \tag{4.1}$$

σ_c = Critical buckle propagation stress

E_{ox}= Young’s modulus of the oxide (367GPa for α-alumina)

υ_{ox}= Poisons ratio of the oxide (~0.3)

ξ = Oxide thickness

R*= Radius of the area of decohesion

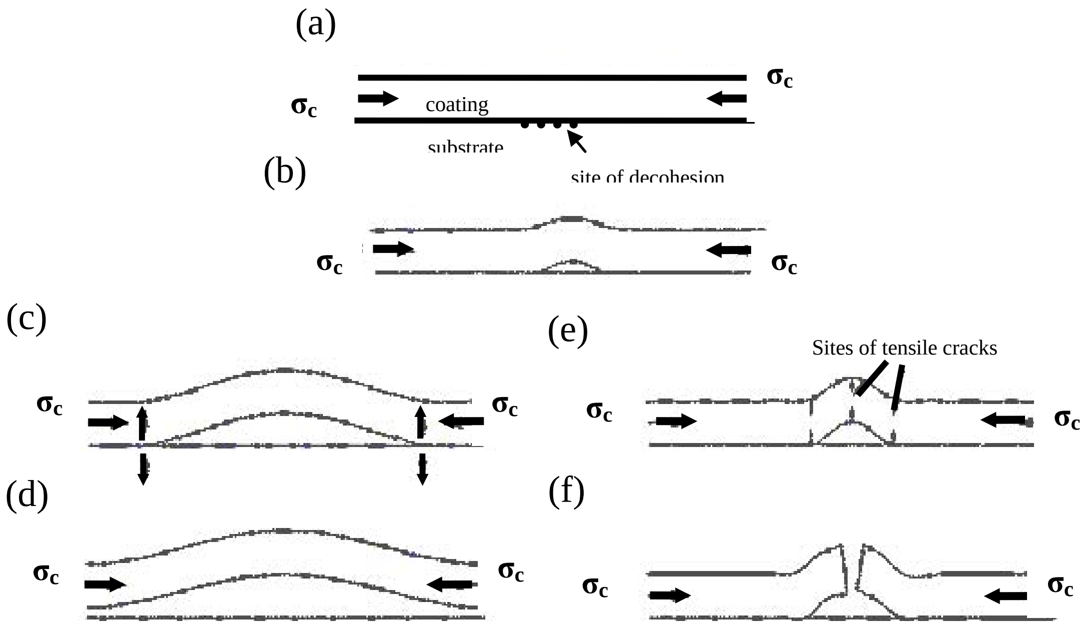

Figure 4.1: Schematic diagram showing the process of buckling [96]

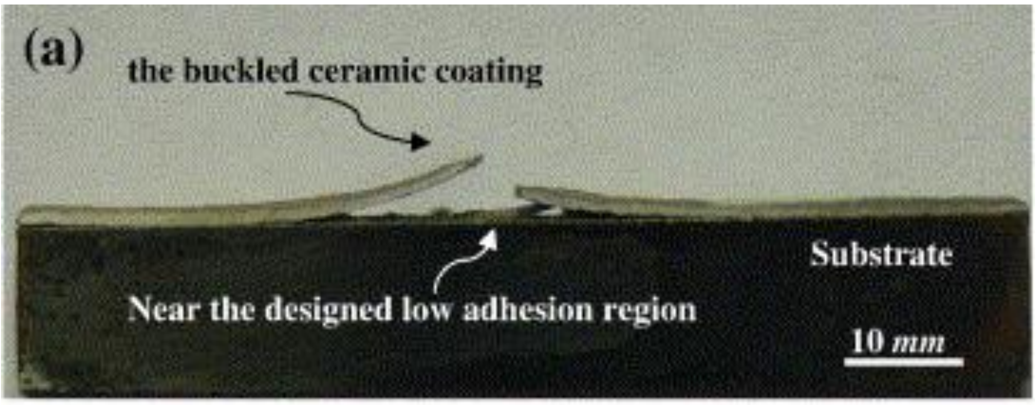

Figure 4.2: Typical example of a buckled topcoat after thermal cycling between 1280°C and 950°C.[99]

The presence of this mechanism is now supported by much experimental evidence[94, 96, 97, 100-102]. It is now generally accepted that this is the final mechanism by which de-lamination occurs in most TBC systems[88, 94, 103]. The main limitation behind this mechanism is the slow stage of sub-critical crack growth at the topcoat/TGO or TGO/bond coat interface that is necessary for the initial area of decohesion to form. Equation 4.1 shows that to generate a sufficient stress for buckle propagation a large area of decohesion and a thin oxide is usually required. It is as yet unclear how these areas of decohesion develop.

4.3 Wedge Cracking

Wedge cracking occurs at the TGO/bond coat interface when the cohesive strength of the TGO is less than the bonding strength between the TGO and substrate[61]. In this case compressive shear cracks develop in the coating as shown in figure 4.3(a) due to compressive stresses set up in the coating during cooling, because of the mismatch in thermal expansion coefficients.[96]

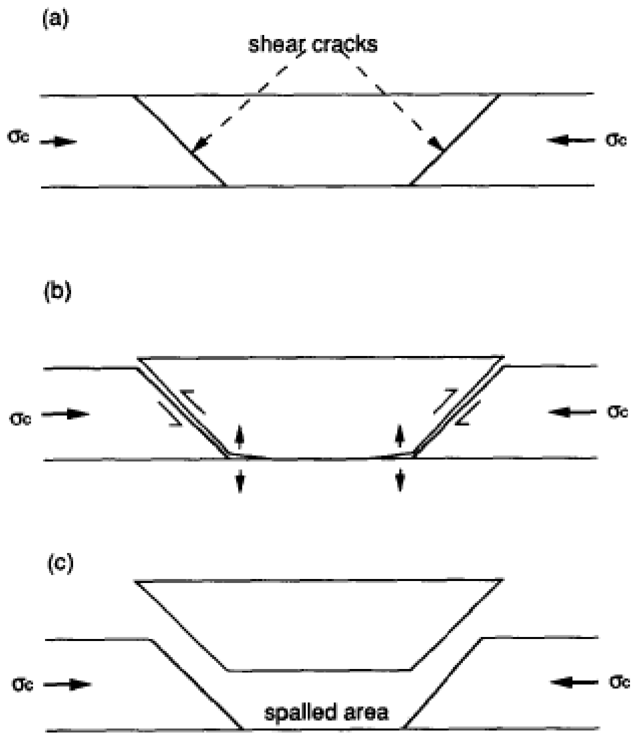

Figure 4.3: Schematic diagram of the mechanism of spallation by wedge cracking.[96]

Continued cooling leads to strain development in the region of the crack due to the deflection of the TGO. This deflection comes from the combination of shear cracks through the TGO and the compressive stress applied on cooling. This leads to the formation of wedges between the coating and substrate as can be seen in figure 4.3(b)[96]. Some of the stress developed is relieved in the bond coat through creep however as the temperature decreases further the compressive stress increases and the ability of the bond coat to creep decreases. When a critical temperature drop is reached enough stress is developed at the crack tip for propagation of the crack along the TGO/bond coat interface[96]. This mechanism has also been demonstrated under the constraint of a topcoat which could potentially restrict the formation of the wedge cracks. However the vertical displacement needed to form the cracks is very small in the region of a 50nm. Therefore modelling of the propagation of cracks with increasing temperature drop and with a compressive stress applied on top shows only restriction of the initial formation of the cracks but no restriction on rapid crack propagation. This mechanism requires through thickness cracks to develop in the TGO, examples of these cracks are rare but have been seen in previous work[104].

4.4 Chemical Failure

Formation of rapidly growing non-protective oxides, usually Ni and Co rich, at the bond coat surface due to localised aluminium depletion is termed “chemical failure”[105, 106]. It can lead to increased out-of-plane stresses within the TBC system and the development of delamination cracks, which can ultimately lead to buckling type failures. It is still unproven whether this mechanism occurs in EBPVD coatings and whether it leads to spallation of the TBC, it has however been shown in overlay MCrAlY coatings as a consequence of the formation of diffusion cells[105-108] which are isolated areas experiencing rapid Al depletion. A limited diffusion path usually caused by topographical features causes this. Once the Al content falls below the 2-4wt% minimum required to sustain an alumina scale, Ni and Co spinels will form. Air plasma sprayed and HVOF bond coats are typically particularly rich in these features due to the oxidation of the individual particles leading to isolated regions as shown in figure 4.4.

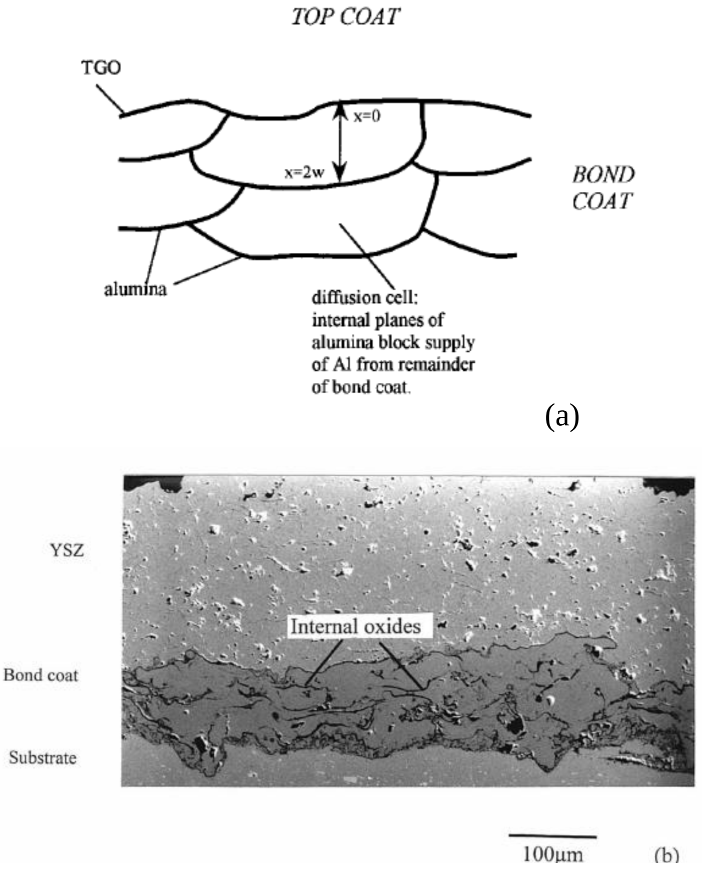

Figure 4.4: a) Schematic diagram showing diffusionally isolated regions of the coating, b) Scanning electron micrograph showing same feature.[107]

4.5 Bond coat Phase transformations

There are three main phases present in the bond coat of most Ni based TBC systems, these are the β (NiAl) phase, γ (Ni) phase and γ′ (Ni$_3$Al) phase. Figure 8.10 shows the distribution of these phases at 1150˚C and as can be seen from the phase diagram, a reduction in Al from the β-phase can lead to conversion of β to γ and/or γ′ phases. This reaction comes from the depletion of aluminium through formation of the TGO and interdiffusion with the substrate leads to a change from the β (NiAl) phase to the γ′ (Ni$_3$Al) phase[109-111]. This could lead to tensile stress being set-up at the interface between the phases due to the associated volume change and also through differences in the thermal expansion co-efficients of the two phases[5, 70]. This applies mainly to the (Ni, Pt) Al bond coats as they primarily consist of the β phase whereas the overlay and γ/ γ′ bond coats contain relatively small amounts or none of the β-phase. It is unclear however whether this transformation has much of an effect on TBC life as some studies have shown that despite a similar volume of γ′ (Ni_3Al) phase being formed in different alloys there is considerable variation in TBC lifetimes[110].

In addition to the phase transformation mentioned above, there are several observations of a further conformational change in the β (NiAl) phase, in which upon cooling it converts from a B2 structure to a distorted $L1_o$ martensite structure[5, 109, 112]. This transformation has associated changes in volume whereby the change from B2 to martensite results in a contraction of ~2%, thus exacerbating the effect of the mismatch in thermal expansion co-efficients[5, 109]. Figure 4.5 shows the percentage strain associated with this transformation both on heating and on cooling and shows that a higher strain with the substrate is maintained during the transformation associated with the volume change. There is also a rapid increase on heating in strain at the point of transformation and a rapid decrease on cooling also at the point of transformation. This mechanism cannot be applied to the γ/γ′ bond coats as they contain little or no β phase.

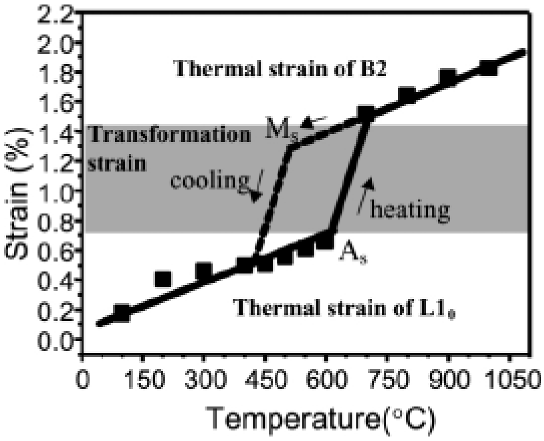

Figure 4.5: Chart to show the strain induced in the bond coat compared to the substrate during the B2 to $L1_0$ transformation in β (NiAl) phase bond coats[5, 109].

4.6 Non uniform oxide growth

In an ideal TBC system the bond coat will form a dense pure α-alumina TGO at its surface, which is protective and slow growing[100]. However, in some TBC systems other aluminas and even other fast growing oxides can form non-uniformly across the surface[16, 33, 35, 48, 53, 105, 106]. These transitional and peg oxides grow at a much quicker rate than the α-alumina, however after relatively short times at high temperature the transitional aluminas will convert to the more stable α form and in doing so undergo a volume contraction[35]. This can put the TGO under considerable tensile stresses, which can lead to crack nucleation at the TGO/topcoat interface. During the production of the bond coats, the heat treatments applied as discussed previously, lead to the development of α-alumina, however some meta-stable transitional aluminas can be present for many hundreds of hours depending upon the exposure temperature[35].

4.7 Growth on Non-planar Surfaces

Most of the failure methods described above are appropriate to flat planar surfaces; however the bond coat surface is never actually flat. In the case of sprayed coatings or CVD processes the surface is often roughened by grit blasting prior to coating in order to aid in coating adhesion[113]. Therefore the TGO grows on non-planar surfaces and so creates out of plane stresses around asperities[94]. Cracks can form at the asperity, when large out-of-plane stresses develop (figures. 4.6 and 4.7). These stresses develop due to the growth of alumina on the flanks of the asperities. The vertical component of this growth is less on these flanks than at the peaks or troughs as the alumina grows perpendicular to the bond coat surface. The displacement of the bond coat in this plane is governed by the oxide growth at the peaks and troughs. Therefore tensile stresses are developed on the flanks of the asperities which can cause cracking in the topcoat and TGO in this region. Figure 4.7 shows finite element modelling of the area around the TGO and demonstrates that significant out of plane tensile stresses can develop along the flanks of the asperities if the roughness amplitude to wavelength ratio is great enough.

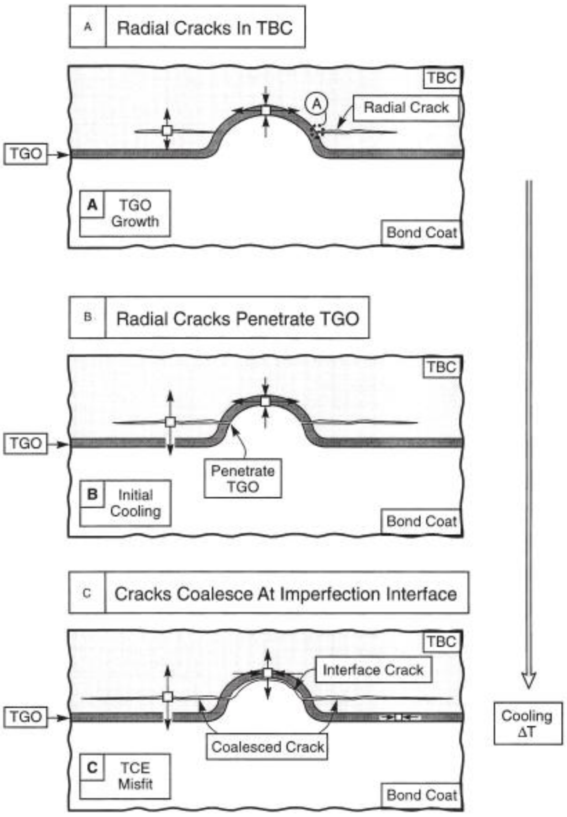

Figure 4.6: Schematic diagram showing the development of cracks due to out of plane TGO growth during cooling[94].

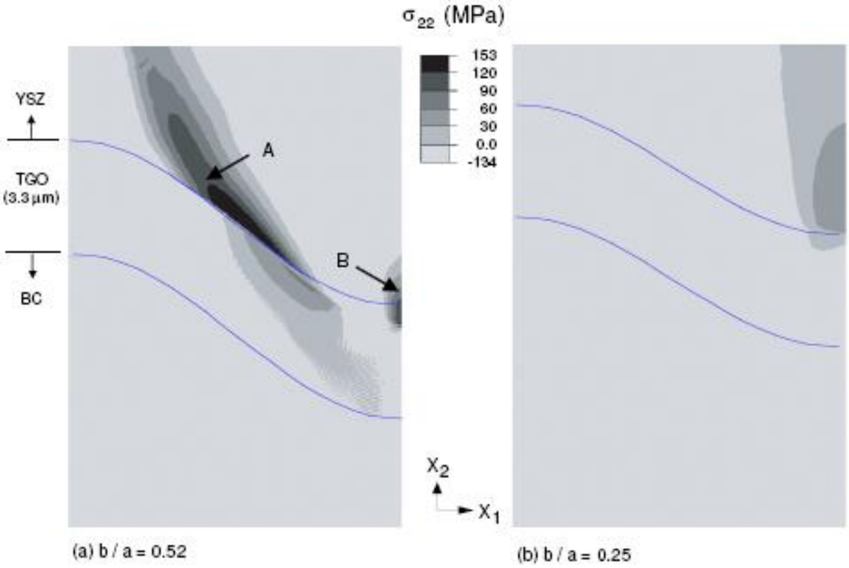

Figure 4.7: Contour of maximum out of plane principal stress near TGO layer at 1100 °C after 100 hours oxidation at 1100 °C in a TBC system when BC and TGO creep behaviour and topcoat sintering are considered. (a) b / a = 0.52 and (b) b / a = 0.25. a = Roughness amplitude, b = roughness wavelength[114]

Experimental evidence suggests that increased surface roughness prior to oxidation significantly decreases TBC life and these locations have been reported as sites of failure [94, 113, 115]

4.8 Ratcheting

Considerable stresses are developed in the TGO upon cooling due to the thermal expansion mismatch with the substrate. On a planar surface these stresses are purely biaxial in nature, however TBC coatings are often quite undulating in nature and are seldom planar, this roughness is often intentionally added to aid mechanical adhesion of the bond coat[116]. These undulations lead to shear stresses on the flanks of the asperities during cooling after growth of the TGO[116, 117]. If these stresses are greater than the yield strength of the alloy the undulation will increase in size due to plastic deformation of the bond coat[116, 117]. This process relies on thermal cycles with incremental increase in roughness with increasing cycles[116, 117]. This increased roughness can lead to decohesion at the base or peaks of the asperities and cause failure through buckling[117].

4.9 Rumpling

It has been shown that repeated thermal cycling of both diffusion and overlay coated bond coats with no topcoat results in a progressive roughening of the bond coat (BC) outer surface[67, 88, 100, 118-128]. This roughening/rumpling leads to characteristic wavelengths in the scale of 130-345μm[88]. It has also been shown that this rumpling is a phenomenon that occurs only in thermal cycled specimens and identical specimens that are isothermally tested do not exhibit this phenomenon[88, 118, 119]. Figure 4.8 shows visually the difference between two identical samples, one treated isothermally at 1150˚C for 100hrs the other with 1hr thermal cycle to 100hrs; clearly the thermal cycled samples exhibit greater roughness.

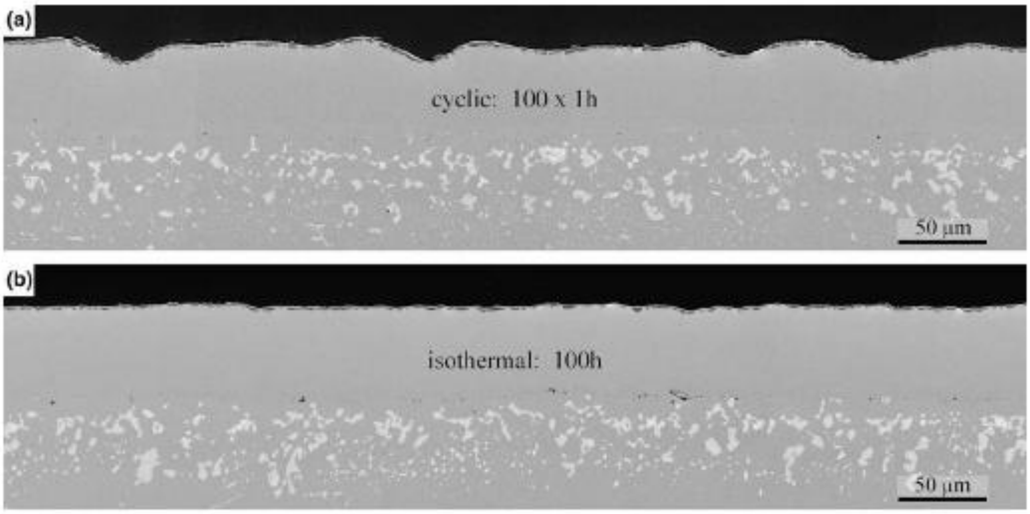

Figure 4.8: Two Scanning electron micrographs showing identical sections through diffusion bond coats without topcoat), a) has been cycled with 100 x 1hr thermocycles at 1150˚C, b) has been held for 100hrs isothermally at 1150˚C[118].

This effect as yet is not fully understood however, it potentially could be a relevant mechanism contributing to failure as most gas turbine engines components are thermally cycled in service[123-125, 127, 128]. Rumpling could be caused by a number of factors including thermal expansion co-efficient mismatch between the bond coat, topcoat and TGO, leading to contraction of the TGO which is accommodated by creep of the bond coat[103]. It does therefore depend upon having a bond coat weak in creep. To date, there is no clear evidence that this mechanism occurs in typically used coatings and this may be because of the mechanical constraint imposed by the outer ceramic layer. Table 4.1 gives the experimentally determined differences of co-efficient of thermal expansion (CTE) compared with the Al_2O_3 TGO. It shows that both phases have considerably different thermal expansions when compared to the TGO, the β- phase is representative of the beta diffusion bond coats and the other two are representative of the MCrAlY overlay and γ+γ′ diffusion bond coats respectively.

Table 4.2: Comparison of the co-efficient of thermal expansion of 3 different bond coats with alumina[129]

Alloy Composition	Thermal expansion co-efficient at 1150˚C, 10^{-6}°C	Alloy phases at 1150˚C
NiPt52Al	11	β
Ni20Cr19Al+Y	15	β + γ
Ni10Cr19Al+Y	13	γ+γ′
Alumina	7.9	α-Al_2O_3

This could cause a characteristic waviness of the coating, depending on the coating strength and the development of voids at the TGO/topcoat interface, as demonstrated schematically in figure 4.9.[119]

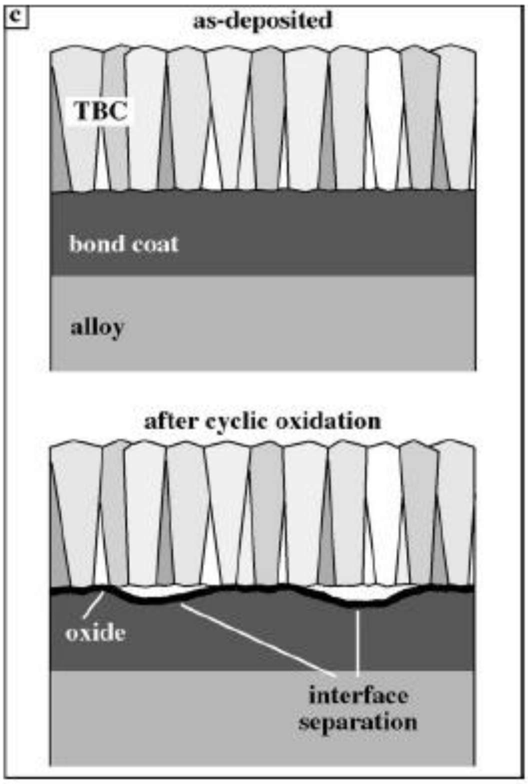

Figure 4.9: Schematic diagram showing how voids and TGO/topcoat separation could occur during rumpling[119]

It is also proposed that the volume contraction associated with phase changes in the bond coat, mainly the β-martensite transformation, could cause surface rumpling if it occurred adjacent to the TGO interface[103]. Rumpling could lead to small void like separations of the TGO from the topcoat[119]. If these small flaws were to coalesce they may lead to a large enough flaw to initiate buckling and spallation/ delamination of the topcoat at the topcoat/TGO interface[119]. However experimental evidence of TBC failures show that most failures occur at the bond coat/TGO interface therefore these flaws would need to initiate cracking through the TGO and as yet there is no evidence for this type of failure.

5 EXPERIMENTAL

5.1 Coating Detail

In the present study, two thermal barrier coating systems were analysed under an isothermal and cyclic testing regime. After oxidation the samples were prepared and examined in order to compare their oxidation kinetics and any damage to the coatings caused during the oxidation process. The two coatings tested in the present study were deposited on to a CMSX-4 nickel based superalloy a typical composition of this alloy is given in table 5.1. The first group of specimens had an overlay NiCoCrAlY coating applied by High Velocity Oxy Fuel (HVOF) spraying and the second group had a similar NiCoCrAlY overlay coating applied by Electron Beam Physical Vapour Deposition (EBPVD). Both sets of specimens had an identical EBPVD applied 7wt% yttria partially stabilised zirconia (YSZ) topcoat.

Table 5.1: Compositional data of a typical CMSX-4 nickel based superalloy in wt.% [130].

Ni	Co	Cr	Al	Ti	Ta	Mo	W	Re	Hf
62	9	6.5	5.5	1	6.5	0.6	6	3	0.1

The approximate compositions of the two bond coats, after deposition, is given in table 5.2. Both are NiCoCrAlY, having more Ni than Co, although the relative amounts of these elements varies in each coating. There is also more Cr in the HVOF bond coat and slightly less Al. There is a significant difference in the quantity of yttrium with the HVOF applied coating showing a higher bulk concentration in the centre of the coating. The HVOF specimens were produced by Siemens Industrial Turbomachinery in Lincoln, UK. The

EBPVD specimens were provided by Siemens of Finspong, Sweden. The coating parameters and pre-spraying compositions were not available from the companies. After the bond coats were applied the specimens were shot peened to flatten and densify the surface before application of the 7 wt% YSZ topcoat. A summary of the makeup of both coatings is given in table 5.3

Table 5.2: Measured average bond coat compositions for both groups of specimens in wt.%

Application Method	Ni	Co	Cr	Al	Y
HVOF	36.2	33.5	21.0	9.0	0.3
EBPVD	52.8	19.2	17.8	10.2	0.1

Table 5.3: Summary of the details of both thermal barrier coating systems studied.

	Substrate	**Bond coat**	**Topcoat**
Coating 1	CMSX-4 (Nickel based single crystal superalloy)	NiCoCrAlY coating applied by HVOF	YSZ deposited by EBPVD
Coating 2	CMSX-4 (Nickel based single crystal superalloy)	NiCoCrAlY coating applied by EBPVD	YSZ deposited by EBPVD

5.2 Specimen Geometry

Both groups of specimens were supplied as small circular buttons with a full coating on two sides only; the base of each button consisted of the bare superalloy. The geometry of the specimens can be found in figure 5.1. The specimens with the EBPVD bond coat were provided with a metallic peg welded to the bare superalloy side of each specimen, which is used to secure the specimen during the coating process, this was removed after testing.

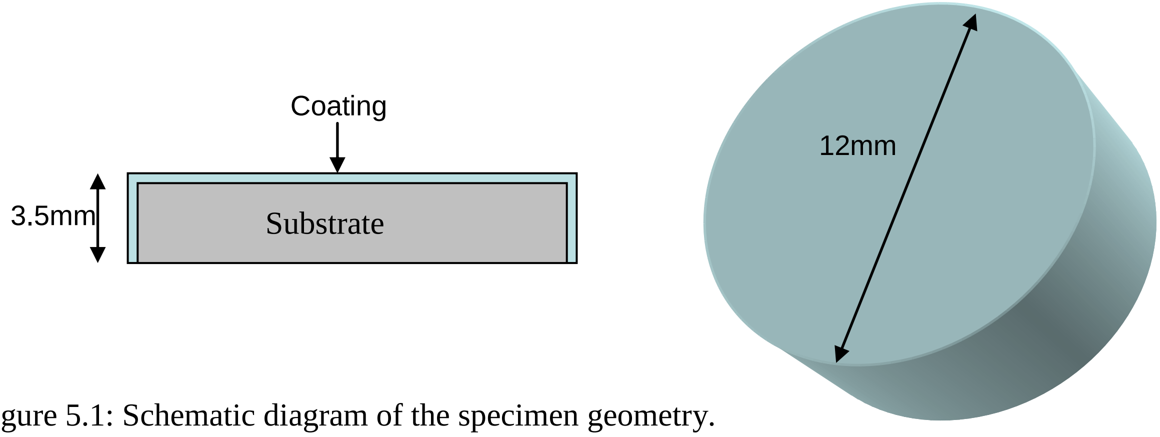

Figure 5.1: Schematic diagram of the specimen geometry.

5.3 Oxidation Testing

Both sets of specimens were oxidised using the same procedure as outlined in the following sections and in the same furnaces.

5.3.1 Isothermal Oxidation

Specimens were oxidised isothermally in laboratory air for up to 3000 hours at temperatures of 950°C and 1050°C in bench top furnaces with tests at 1150°C being carried out in a vertical furnace. Tests were also conducted at 1000°C and 1100°C in a bench top furnace for the HVOF applied bond coat only. Due to the limited availability of specimens with the EBPVD bond coat testing at these temperatures was not possible. The full test matrix for both coating systems is given in Section 5.7.

The specimens were first measured using a micrometer to assess the thickness and diameter before being cleaned ultrasonically in ethanol for 5 minutes. They were then placed onto a clean alumina boat of approximately 90 mm in length as can be seen in figure 5.2A. The furnace was preheated to the set temperature before the specimens were inserted using a metallic rod. This was done in 3 increments to prevent thermal shock of the alumina furnace tube and alumina boat. After the specimen was fully inserted, the end of the furnace was covered with alumina wool to maintain a consistent temperature but allow unrestricted air access. Figure 5.2 shows photographs of (A) specimen positioned in one of the alumina boats and (B) one of the bench top furnaces used.

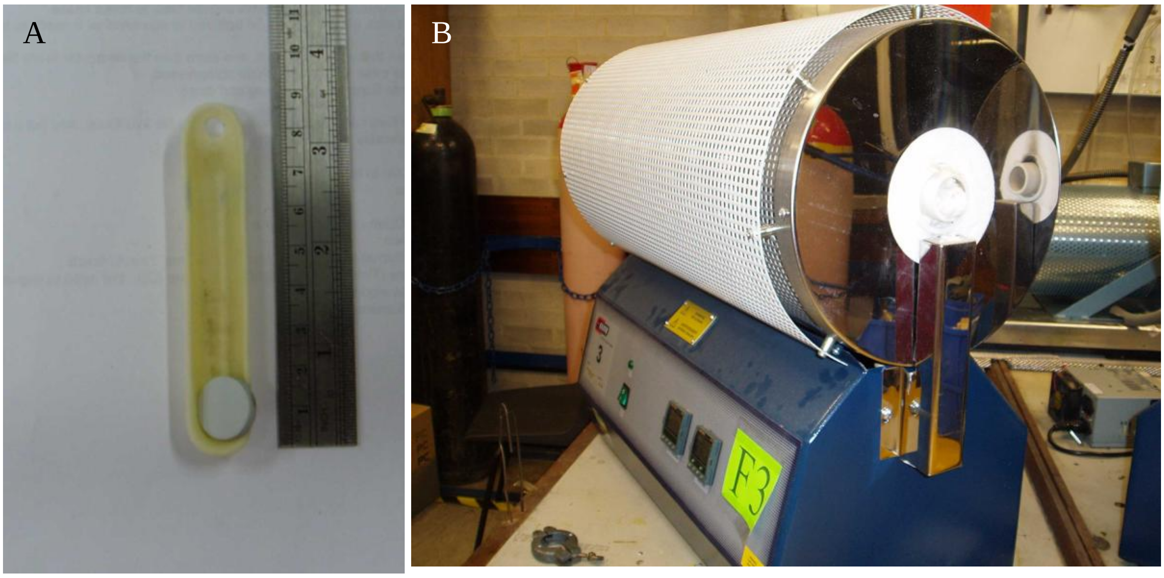

Figure 5.2: Photographs of the isothermal test set-up showing (A) a specimen positioned on an alumina boat and (B) an isothermal bench-top furnace.

After the allotted test time, the specimens were removed from the furnace and allowed to cool in the alumina boat in laboratory air to room temperature before being prepared for examination as described in Section 5.5.

5.3.2 Thermal Cycling

Surface rumpling has been cited as a potential failure mechanism for these coating types, Section 4.9. To ascertain whether this is the case the following testing regime was carried out on specimens from each coating type. Firstly, the topcoat on these specimens was removed from half of the top surface mechanically using wet and dry SiC paper. The exposed bond coat was then roughened using a grinding stone to more closely match the surface roughness of the bond coat section with topcoat attached. The specimens were sectioned using a slow speed saw with a cubic boron nitride (CBN) blade such that each half consisted of one section with a topcoat intact and the other section was exposed bond coat. One of these half specimens was examined metallographically in the as-received condition and the other half specimen was cyclically oxidised to failure by spallation of the remaining topcoat. The cycles consisted of 1 hour at 1170°C followed by 5 minutes cool down in laboratory air and 15 minutes standing in laboratory air. The cool down and standing procedure was carried out in the furnace tube with the furnace having been moved away. Examination of the specimen for spallation was possible after every cycle as a silica furnace tube was used for the majority of the cycles. Later cycles were carried out in an alumina tube with examination of the specimen taking place after each cycle through the end of the tube and a closer examination was carried out by removing the sample from the furnace tube after cooling. These tests were carried out in a horizontal furnace thermal cycling rig built for this project and a picture of the set-up can be seen in figure 5.3.

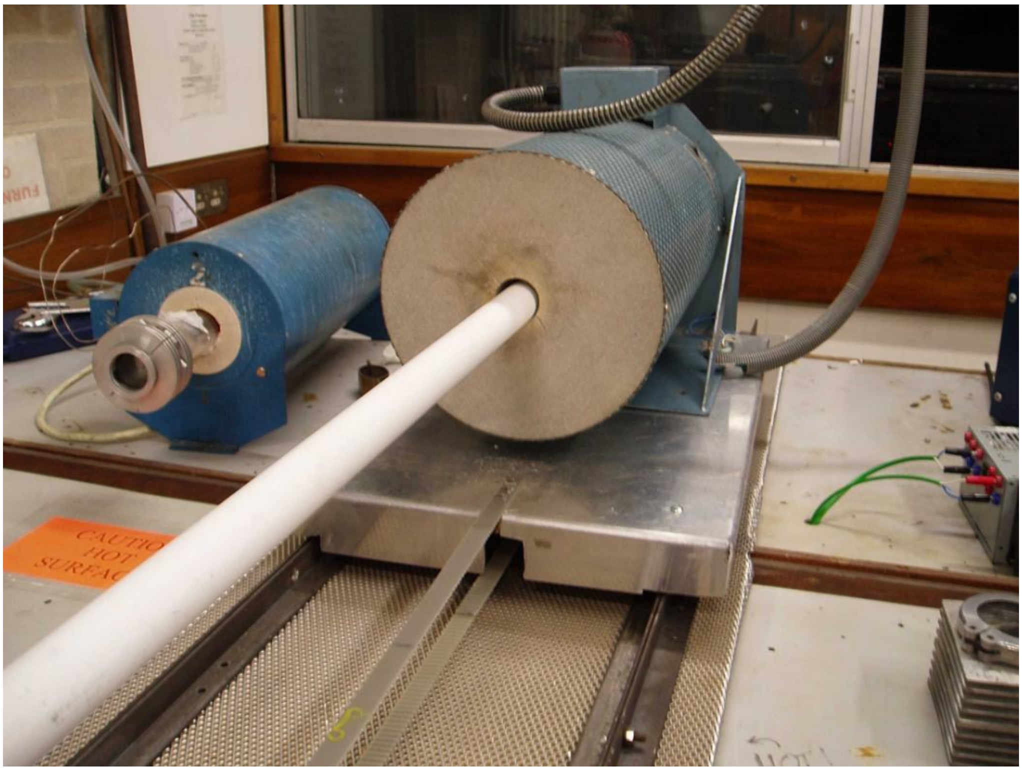

Figure 5.3: Photograph of the thermal cycling set-up created for this project.

5.4 Specimen Preparation

After testing and cooling to room temperature the specimens were vacuum impregnated in a low viscosity epoxy resin (Epofix, made by Struers) to protect the coating from damage from subsequent preparation. The specimens were allowed to cure for at least 24 hours before being sectioned perpendicular to the top surface using a CBN blade. To ensure that the specimens remained flat for the duration of the preparation they were mounted, with cut face exposed, in a high filler content epoxy resin with a much higher hardness than the Epofix resin. Once the resin had set, the specimens were ground to 1200 grit using wet and dry SiC paper and subsequently polished using diamond suspension down to ¼ μm finish. A short final polish using an alumina sol was performed immediately prior to examination; the time of this final polish was only a few minutes to minimise etching by the sol of certain phases within the bond coats.

5.5 Microscopy

Two different microscopes were used to examine the specimens. A Philips XL-30 microscope with a LaB_6 filament with a resolution of ~0.5µm was used for comparatively low magnification imaging for surface roughness measurements and for bond coat microstructural analysis using Energy Dispersive Spectroscopy (EDS). High-resolution images and detailed compositional analysis was provided by a JEOL 7000 microscope with a field emission gun, which provides a very stable high density, narrow electron beam and a resolution of up to 3nm, with a typical resolution for the specimens tested here of around 50nm. Microscopy was used to characterise the samples, measure the thickness of the TGO, identify sources of cracking, provide information on surface roughness and for compositional details.

An extensive study was made of the growth of the TGO as this is thought to be one of the important factors that affect coating life in service. Therefore it is important to identify the growth kinetics of the TGO over time at temperature. Ten images of sections through the coating were obtained at regular intervals across each tested coating using the JEOL 7000 microscope. Figure 5.4 shows an example of one of these images.

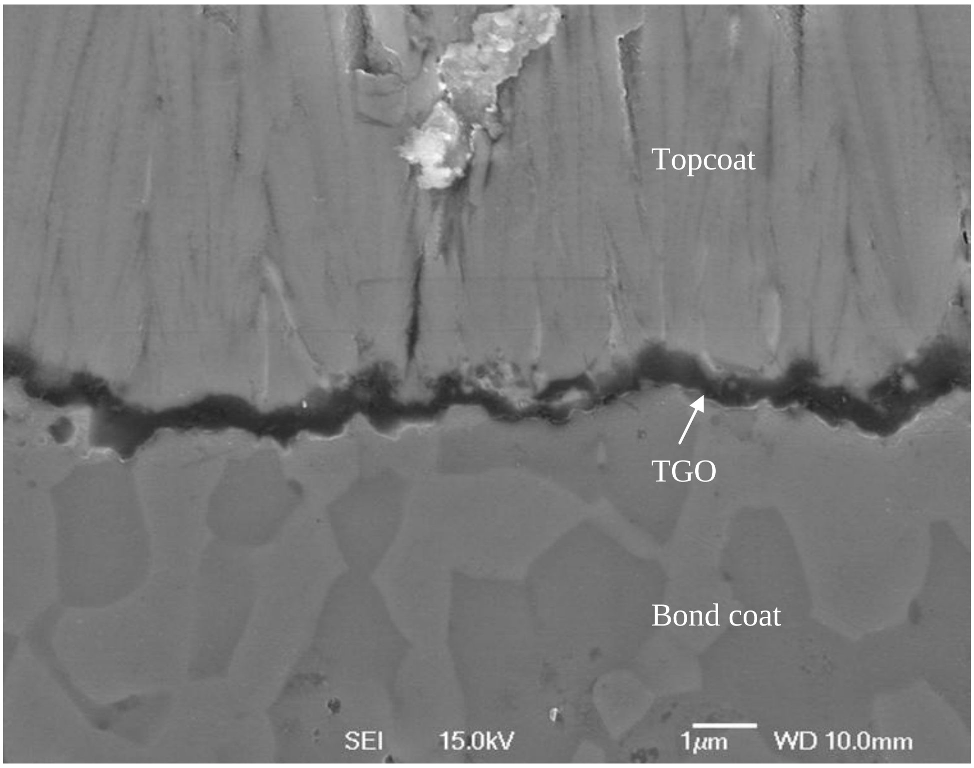

Figure 5.4: SEM micrograph of a section through a TBC with an EBPVD bond coat in the as-received condition showing details of the bond coat, topcoat and TGO interface.

Ten TGO thickness measurements were taken at equally spaced intervals from each image, i.e. in the growth direction of the oxide. This gave a total of 100 measurements for each specimen. These measurements were plotted onto a probability plot. The mean TGO thickness and standard deviation were also calculated.

A single representative specimen was selected to examine the structure in the as-received condition. This sample was used as a benchmark from which to provide an initial oxide thickness and surface roughness value for comparison and calculations of TGO growth rate during the laboratory testing. Ideally a starting thickness for each individually tested specimen should be used to accurately measure the thickness of oxide produced during testing. However, this was not possible as sectioning each sample would introduce additional stresses into the coatings and would also expose an uncoated superalloy section whereby oxygen could ingress and adversely alter the oxide growth. It was therefore decided that this was a good approximation and any variation between specimens would fall within the resolution of the measurements taken.

Common to all of the proposed failure mechanisms in these coatings is the nucleation and growth of micro-cracks. Therefore, one of the main tasks of imaging microscopy was to examine the cross sections for evidence of these cracks and, if found, to relate the location to any microstructural or topographical features.

Surface roughness has been cited as an important factor in several proposed TBC failure mechanisms, e.g. rumpling; therefore, the surface roughness was determined from sections taken through various specimens, including the thermally cycled specimens. Five low magnification micrographs were taken at representative regions across the bond coat interface and included the IDZ and part of the topcoat. An example is shown in figure 5.5; note that a straight line parallel to the TGO can be drawn at the IDZ / bond coat interface. This line was used as a reference line away from, and parallel to, the TGO surface. Measurements were taken from this line to the bond coat/TGO interface at 10μm intervals, figure 5.6. An average of these values was taken to identify the mean location of the surface as shown by the dashed line in figure 5.6.

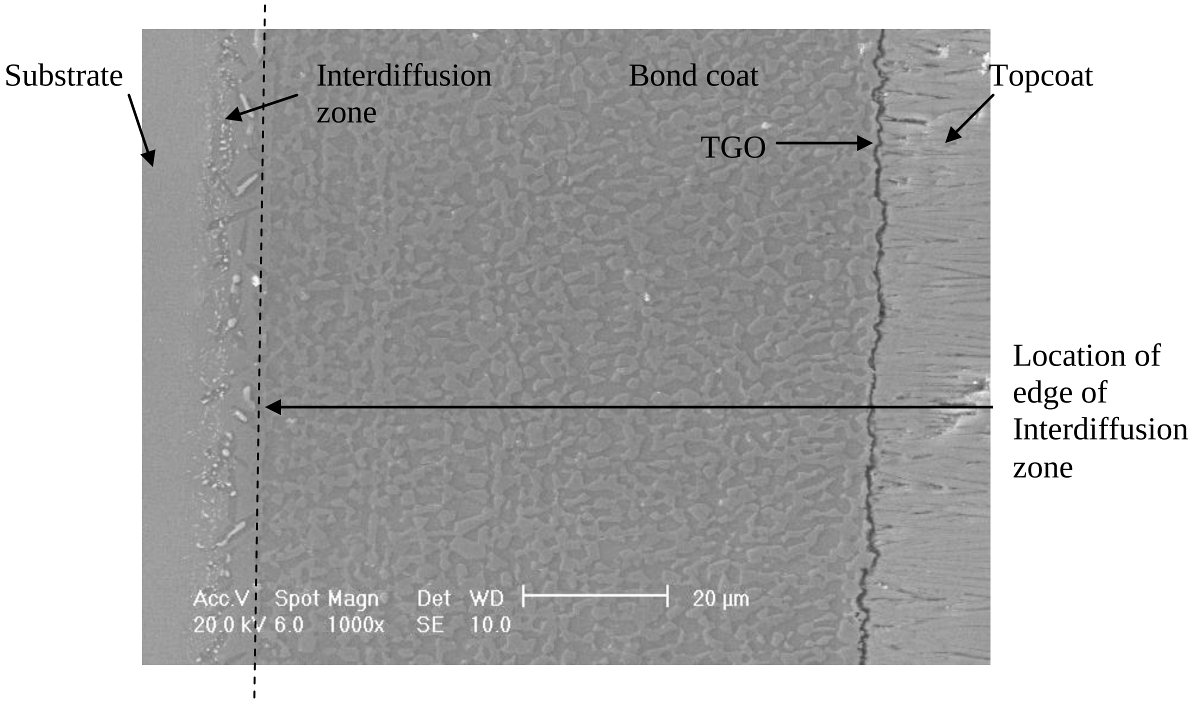

Figure 5.5: SEM micrograph of an as-received specimen with an EBPVD bond coat, showing the location of the reference line used to calculate surface roughness.

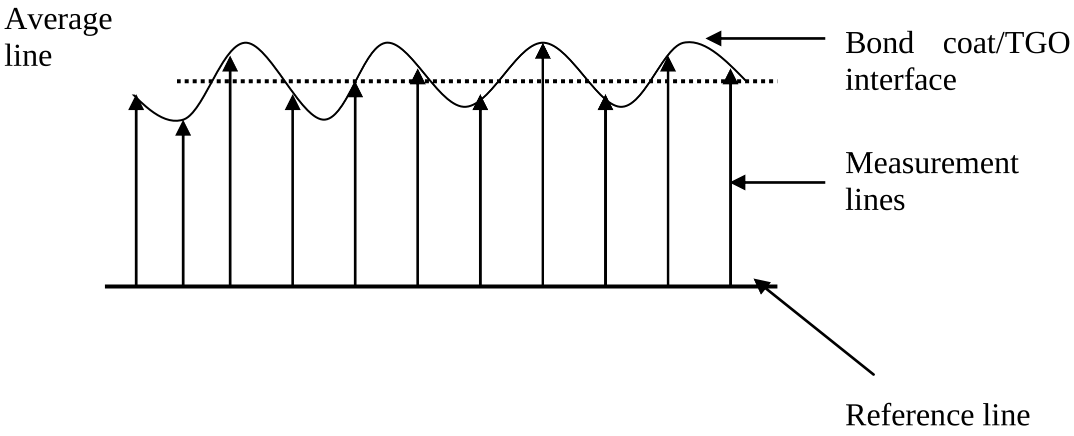

Figure 5.6: Schematic diagram of surface roughness measurement.

This mean point was subtracted from the original measurements to obtain a set of values of the distance of the actual interface surface from the average line. The R_a value could then be calculated using the procedure laid down in British Standard BS1134, thus:

$$\bar{y} = \frac{\sum_{i=1}^{n} y_i}{n} \tag{5.1}$$

$$R_a = \frac{\sum_{i}^{n} |y_i - \bar{y}|}{n} \tag{5.2}$$

Where,
R_a= Roughness average
n=number of sampling lengths
y=surface profile

In addition, the wavelength and amplitude of the surface roughness was measured in a number of isothermally oxidised specimens to give an indication of changes in surface roughness with time and temperature.

In order to characterise the microstructure of the alumina TGO and possible effects this might have on the oxidation kinetics and failure modes observed, an EBSD study was carried out using the JOEL 7000 SEM. Unfortunately sample preparation through mechanical polishing was not sufficient for this technique to be useful.

5.6 X-Ray Diffraction (XRD)

Phase analysis of the TGO and topcoat was carried out using X-Ray Diffraction. A section of spalled topcoat with TGO attached was examined using an incident X-ray beam at angles between 5 and 20°, to minimise the penetration depth of the incident beam. Peaks attributed to the YSZ were inevitable due to the thin TGO but could be easily identified and eliminated.

5.7 Test Matrix and Coding

The following tables show the isothermal test times and temperatures conducted in this study. For both coatings short term testing at the lower temperatures was omitted as the growth of the oxide would have been very small. Testing in all cases was stopped at the longer times when specimen failure by spallation occurred.

Table 5.4: Test matrix for the HVOF applied bond coat TBCs.

Time(h)/ Temperature	1	2	4	8	25	50	100	240	500	750	1000	2000	3000
950°C	⬛	⬛	🟩	🟩	🟩	🟩	🟩	🟩	🟩	⬛	🟩	⬛	🟩
1000°C	⬛	🟩	🟩	🟩	🟩	🟩	🟩	🟩	🟩	🟩	⬛	⬛	🟩
1050°C	⬛	🟩	🟩	🟩	🟩	🟩	🟩	🟩	🟩	⬛	🟩	⬛	⬛
1100°C	🟩	🟩	🟩	🟩	🟩	🟩	🟩	🟩	⬛	⬛	⬛	🟩	⬛
1150°C	🟩	🟩	🟩	🟩	🟩	🟩	🟩	⬛	⬛	⬛	⬛	⬛	⬛

Tested	🟩
Not Tested	⬛

Table 5.5: Test matrix for the EBPVD applied bond coat TBCs.

Time(h)/ Temperature	1	2	4	8	25	50	100	240	500	1000	3000
950°C	⬛	⬛	🟩	🟩	🟩	🟩	🟩	🟩	🟩	🟩	🟩
1050°C	⬛	🟩	🟩	🟩	🟩	🟩	🟩	🟩	🟩	🟩	⬛
1150°C	🟩	🟩	🟩	🟩	🟩	🟩	🟩	⬛	⬛	⬛	⬛

Tested	🟩
Not Tested	⬛

Due to the large number of specimens used in this study and the array of different cooling types and oxidation regimes a coding system was devised. This is indicated below and these codes may be found throughout this thesis to aid in descriptions of exact specimen conditions.

L NF 100 SC

Bond coat type
L=HVOF
F=EBPVD

Temperature
NF=950°C
T =1000°C
TF=1050°C
H =1100°C
HF=1150°C

Time Temperature
(Hours)

Special Code
SC=Slow Cooled
Q=Water Quenched
Pt=Platinum Coated
TC= Thermal Cycled

These extra codes where duplicated as necessary

6 RESULTS FOR THE TBC SYSTEM WITH THE HVOF APPLIED NICOCRALY BOND COAT

6.1 Introduction

This section contains the results of the testing described in section 5 on the TBC system with the HVOF NiCoCrAlY bond coat. The results of the testing performed on the TBC system with the EBPVD NiCoCrAlY bond coat are given in section 7. A comparison of the two coating systems is made in the discussion, section 8, which will also include information from the literature.

The growth of the TGO is dealt with first for each coating type as this is the main emphasis of this thesis. This naturally leads on to lifetime determination and prediction which, in turn, leads on to seeking an understanding of the mechanisms leading to spallation of the topcoat and thus failure of the coating system. Thus, sub-sections on analysis of oxide growth, surface roughness, composition and cracking are included.

6.2 Oxide Thickness Distribution

The oxide thicknesses measured from all the specimens examined as shown in section 5.7, were plotted on probability plots and were found to follow a normal Gaussian distribution, figure 6.1 shows three test temperatures with a fixed oxidation exposure of 4 hours. Shown in these plots are the actual data points plotted on to a predicted normal distribution curve obtained from the data. The good fit seen in these distribution curves and the lack of excessively thick oxides in these specimens demonstrates, along with the SEM examination, that no fast growing non-protective oxides were formed at any of the test times and temperatures. Such oxides, essentially Ni, Co and Cr spinels, are associated with topcoat delamination late in life and result from localised aluminium depletion within the bond coat[107, 131, 132]. Their absence in the present specimens indicates that this mechanism of failure did not operate in the present tests.

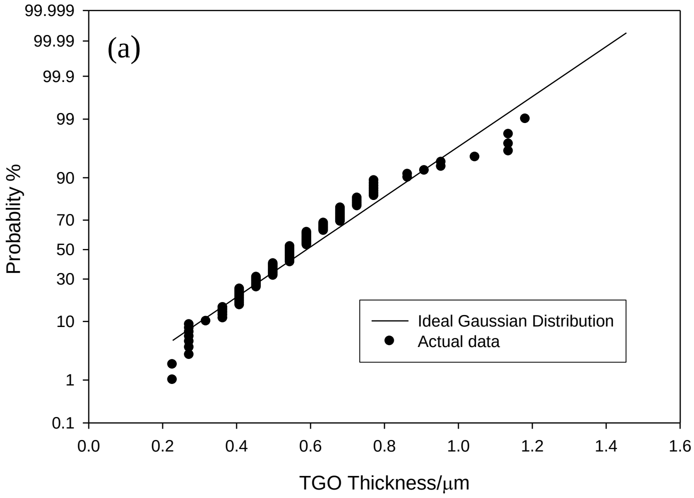

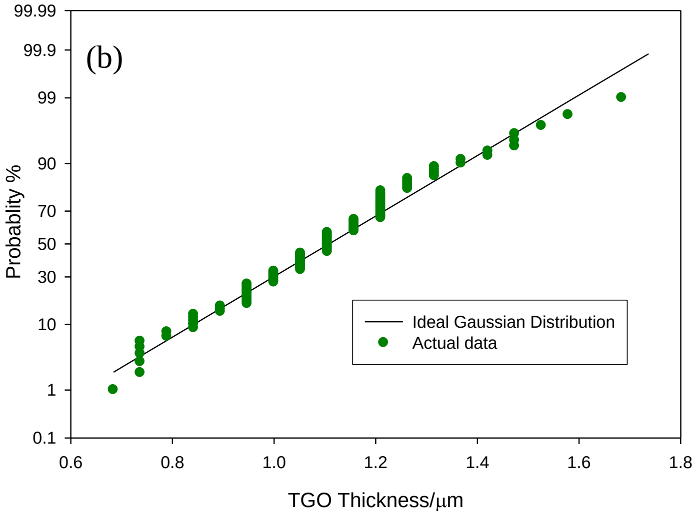

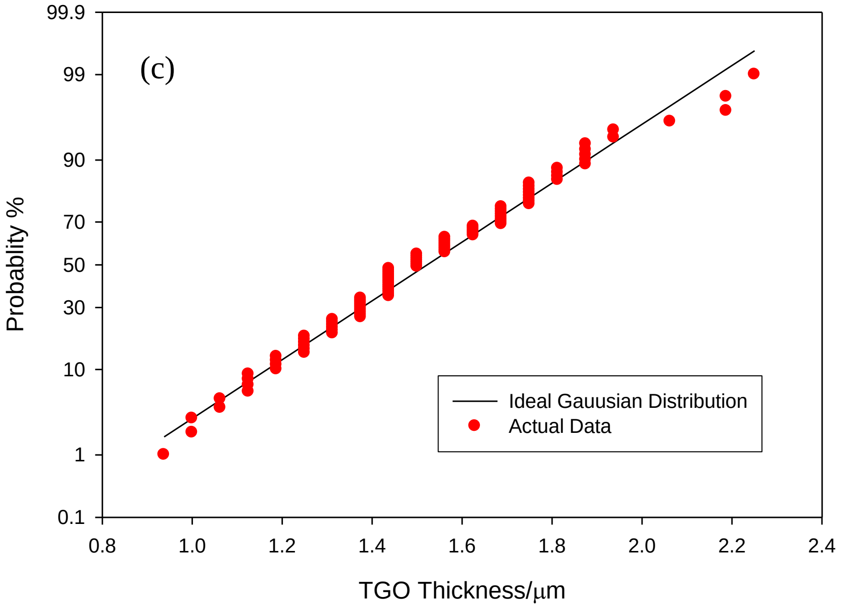

Figure 6.1: Probability plots showing a normal Gaussian distribution of TGO thickness for specimens tested for 4 hours at (a) 950°C, (b) 1050°C and (c) 1150°C.

A similar plot showing the influence of increasing exposure time at the highest test temperature of 1150^{o}C is shown in figure 6.2. Again, a normal distribution was observed even after extended exposure periods. It is also clear, however, that the standard deviation increased with increasing exposure time, see also table 6.1. An explanation of this trend may be that there is a persistent high and low alumina growth rates in localised regions of the bond coat surface. As each region continues to grow it does so at its own individual rate, thus producing the effect seen here. This may also be due to grain orientation differences within the alumina TGO, but the exact mechanism is not fully understood. Attempts were made to index the orientation of the alumina TGO using Electron Backscatter Diffraction (EBSD). Unfortunately, whilst it was possible to image some bond coat grains, it proved exceedingly difficult to mechanically polish the sectioned surface to the level necessary to obtain information using this technique. This is primarily due to the close proximity of three very different materials with different polishing requirements. This leads to the effect of relief being evident in the polished surface and insufficient index being obtained. This problem could possibly be alleviated in future work by the use of electro-polishing techniques or using the recently installed focussed ion beam scanning electron microscopy (FIBSEM). However insufficient time was available in this project for this to be attempted. An example of the polishing that could be achieved using this technique can be found in section 8, figure 8.4.

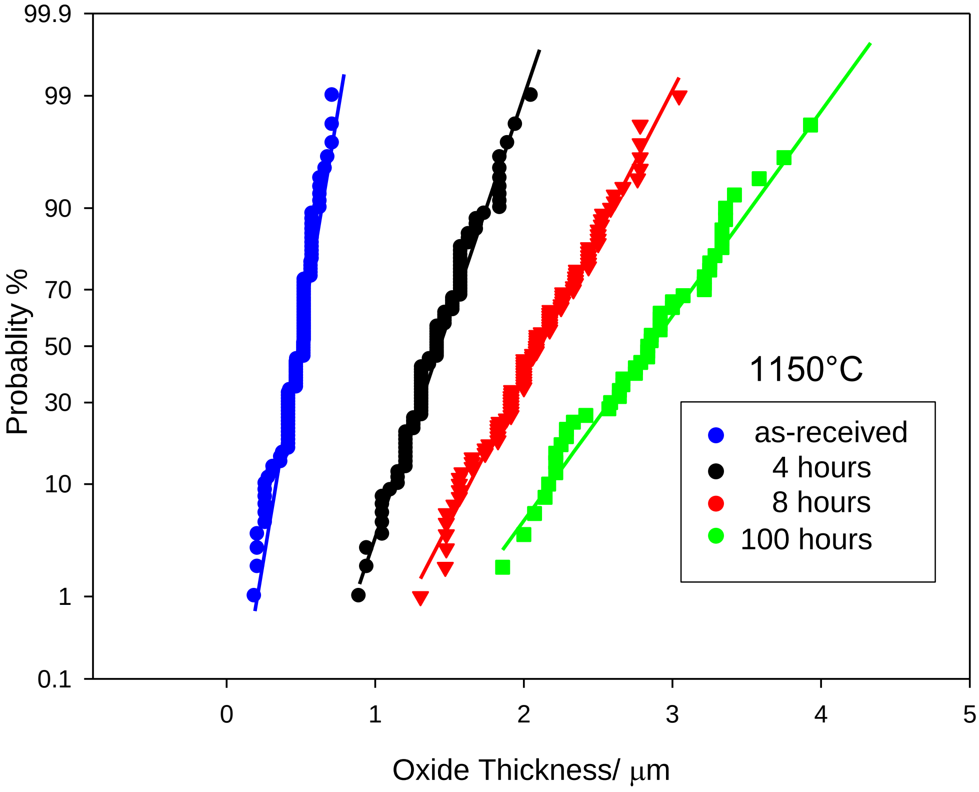

Figure 6.2: Probability plots of TGO thickness distribution in the as-received condition and after various exposure periods at 1150^{o}C. The change in slope of the curves indicates that the standard deviation of the distribution increases with exposure time.

In addition to the above, this observed increase in standard deviation could be attributed to an increase in surface roughness with increasing time at temperature. This would lead to localised angled slices of the TGO being taken during the cross sectioning procedure which would falsely indicate an abundance of thicker growing oxides. However, no increase in surface roughness was observed in these specimens as described later in section 6.4.1, therefore it is highly unlikely that this effect is being seen here.

Table 6.1: Mean and 2 standard deviations of the TGO thicknesses for the specimens with an HVOF bond coat at all times and temperatures, taken from 100 measurements per specimen. A summary of the cracking and spallation observations is also included.

Time/ h	950°C	1000°C	1050°C	1100°C	1150°C
0	0.49 +/- 0.24μm	0.49 +/- 0.24μm	0.49 +/- 0.24μm	0.49 +/- 0.24μm	0.49 +/- 0.24μm
1	NOT TESTED	NOT TESTED	NOT TESTED	1.04 +/- 0.68μm	1.05 +/- 0.38μm
2	NOT TESTED	0.87 +/- 0.28μm	0.95 +/- 0.41μm	1.06 +/- 0.68μm	1.36 +/- 0.39μm
4	0.57 +/- 0.33μm	1.01 +/- 0.41μm	1.11 +/- 0.41μm	1.44 +/- 0.49μm	1.43 +/- 0.49μm
8	0.94 +/- 0.39μm	1.15 +/- 0.38μm	1.37 +/- 0.54μm	1.51 +/- 0.59μm	2.11 +/- 0.75μm
25	0.96 +/- 0.34μm	1.39 +/- 0.53μm	1.56 +/- 0.66μm	2.06 +/- 0.69μm	DELAMINATED
50	1.05 +/- 0.46μm	1.58 +/- 0.54μm	1.93 +/- 0.67μm	2.41 +/- 0.78μm	SPALLED
100	1.17 +/- 0.45μm	1.83 +/- 0.61μm	2.01 +/- 0.62μm	SPALLED	2.85 +/- 1.05μm
240	1.49 +/- 0.56μm	2.05 +/- 0.58μm	DELAMINATED	SPALLED	NOT TESTED
500	1.94 +/- 0.59μm	DELAMINATED	SPALLED	NOT TESTED	NOT TESTED
750	NOT TESTED	2.36 +/- 0.75μm	NOT TESTED	NOT TESTED	NOT TESTED
1000	2.30 +/- 0.87μm	NOT TESTED	NOT TESTED	NOT TESTED	NOT TESTED
2000	NOT TESTED	SPALLED	NOT TESTED	SPALLED	NOT TESTED
3000	2.60 +/- 0.84μm	NOT TESTED	NOT TESTED	NOT TESTED	NOT TESTED

🟩	Sub Critical Cracking Observed
🟨	Delaminated at TGO/Bond-coat Interface
🟥	Spallation at TGO/Bond-coat Interface

6.3 Oxidation Kinetics

The oxidation kinetics was determined for five temperatures from the increase in TGO thickness as described in section 5.5. The TGO thickness present on the HVOF bond coat in the as-received condition was found to be 0.49 μm, figure 6.3. This is a characteristic feature of TBC systems which have an EBPVD topcoat and was formed during the topcoat manufacturing stage and is essential for bonding. This value was subtracted from all the TGO measurements taken from the tested specimens to give TGO growth rates for the oxidation test conditions.

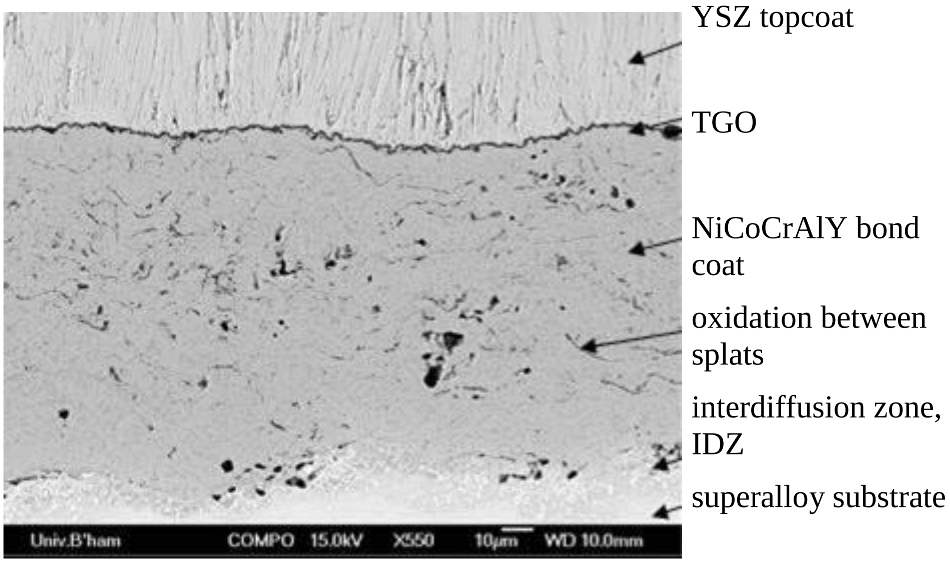

Figure 6.3: Scanning electron micrograph of a section through the as-received TBC system consisting of a NiCoCrAlY HVOF bond coat with an EBPVD topcoat. The thin (0.49 μm) alumina TGO layer, formed during processing, can be seen in dark contrast between the topcoat and bond coat.

Equation 6.1 describes the kinetics of oxidation growth for these systems[22].

$$\xi = (k_n t)^{1/n} + \xi_o \qquad (6.1)$$

Where, ξ is the measured average oxide thickness in metres, t is time in seconds, ξ_o is the average oxide thickness in the as-received condition, taken as 4.9×10^{-7}m for all specimens; n is a numerical constant and k_n is a rate constant.

Equation 6.1 as described in section 2.2.2 describes the sub parabolic oxidation of an oxide growing on a pre formed none protective oxide. It applies well to the coatings studied here due to the formation of the transitional alumina, θ-alumina, during the application of the topcoat. This transitional alumina, then transforms to α-alumina after a short time, typically 2 hours at 1100°C[133]. This transformation results in a volume contraction and resultant tensile stress in the order of 400MPa in the growing oxide[134]. This stress leads to through thickness cracks through the θ-alumina matrix and growing α-alumina nodules[133]. These cracks allow direct molecular gas access to the metallic bond coat surface and thus remove the protective nature of the oxide[133]. Subsequent oxidation fills the cracks with α-alumina but this can take as much as 250 hours at 1000°C[133].

Log/log plots of the increase in oxide thickness against exposure time at each temperature provides the time exponent, n, by taking the inverse of the slopes, figure 6.4. The values of n obtained in this way are given in table 6.2.

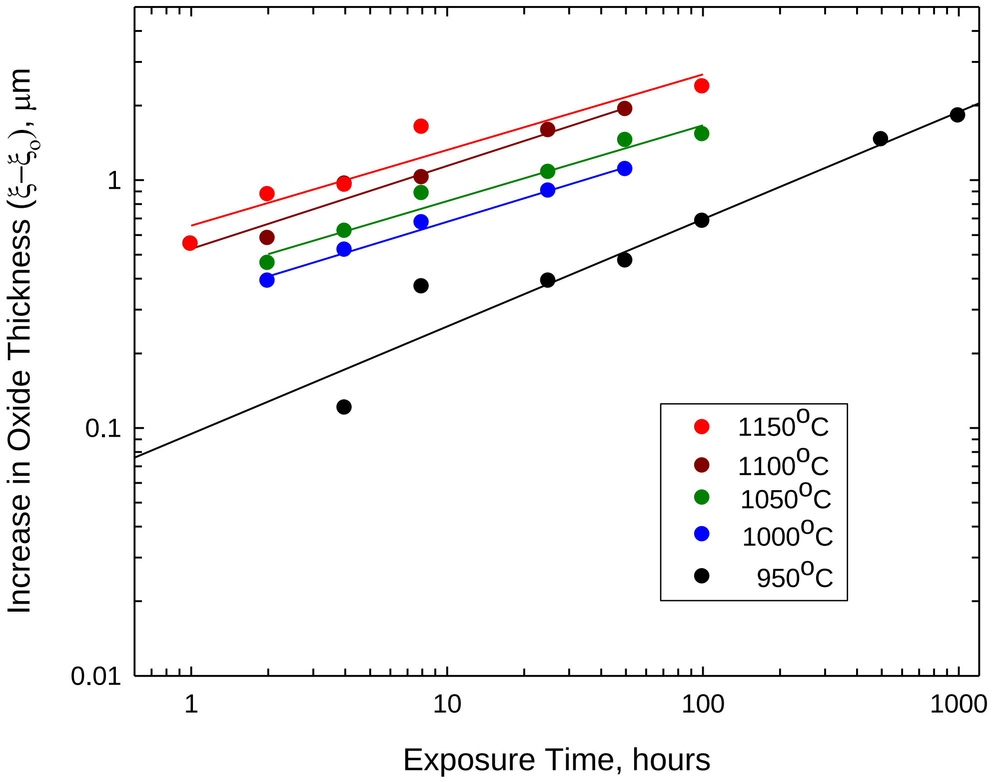

Figure 6.4: Plot of increase in TGO thickness growth kinetics for the five test temperatures plotted according to equation (6.1).

Table 6.2: Experimentally determined time exponents' n from equation 6.1 for the HVOF NiCoCrAlY bond coat.

Temperature, °C	Time exponent n
950	2.31
1000	3.18
1050	3.27
1100	2.99
1150	3.28

The time exponent, n, in all cases was found to be >2, demonstrating that sub-parabolic oxidation kinetics were observed. Such sub-parabolic behaviour is commonly observed in alumina-forming alloys [13, 15, 16, 24, 33, 135] and other systems [25, 31]. It has been attributed to various factors including the transformation from transitional aluminas such as θ or γ to α-alumina after a short time at temperature. Typically these transitional aluminas have a much increased rate of growth when compared to α-alumina[13, 33, 35]. At the elevated temperatures used in these tests this transformation would occur after a short period of time. In addition, the presence of an already formed dense α-alumina, as is the case here, would preclude formation of any further transitional aluminas and thus this mechanism is unlikely to cause the sub-parabolic behaviour seen here.

Alternatively, an increase in the average oxide grain size would lead to a decrease in the number of available grain boundaries within the TGO for short circuit diffusion[25]. It has been demonstrated that the rate of oxygen transfer across the TGO is higher than would be predicted through lattice diffusion of oxygen, therefore a short circuit pathway for oxygen diffusion must exist[25]. This is thought to occur along grain boundaries within the TGO, thus an increase in the average oxide grain size with time at temperature would cause decrease in oxygen diffusion and so a decrease in oxidation rate, as seen in these specimens. This is the likely cause of the sub-parabolic growth described here[25].

A continuous increase in compressive growth stress within the oxide layer has been demonstrated to reduce the growth rate of an oxide, likewise a tensile stress will increase the oxide growth rate[27-30]. This effect has been described and modelled by Evans et al for zirconia and agrees with the observations of the other systems cited above [31]. A stress in the order of several GPa has been measured indirectly for alumina growing in a coating however these results of at temperature growth stresses are difficult to determine.

The rate constant k_n was calculated by plotting the increase in oxide thickness raised to the value of n at each temperature against the oxidation time again using equation 6.1, figure 6.5.

The value k_n was determined from the slope of the resultant linear plot, the calculated values of the rate constants are given in table 6.3

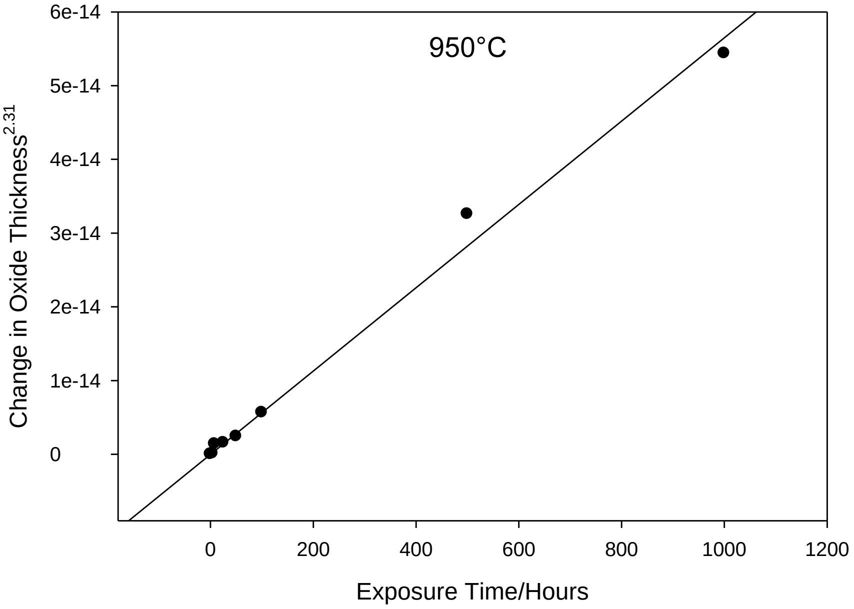

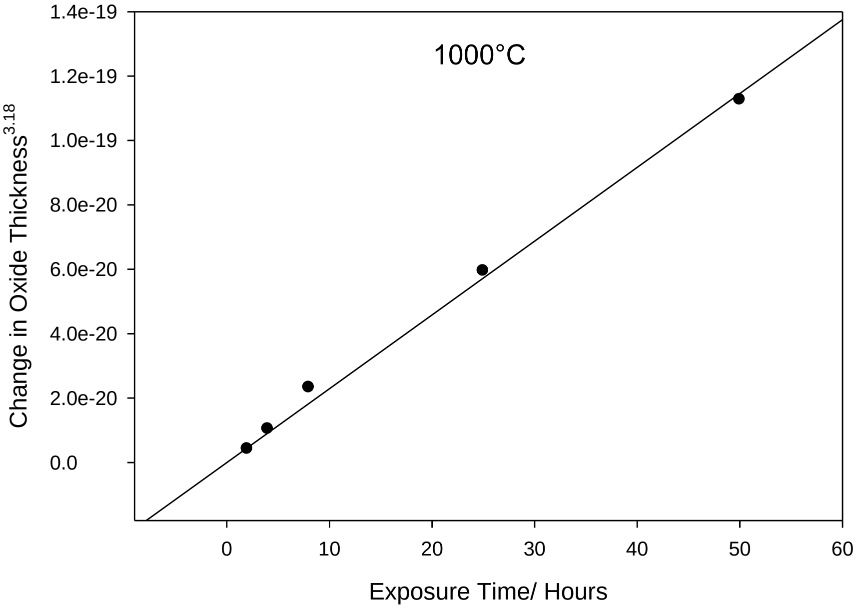

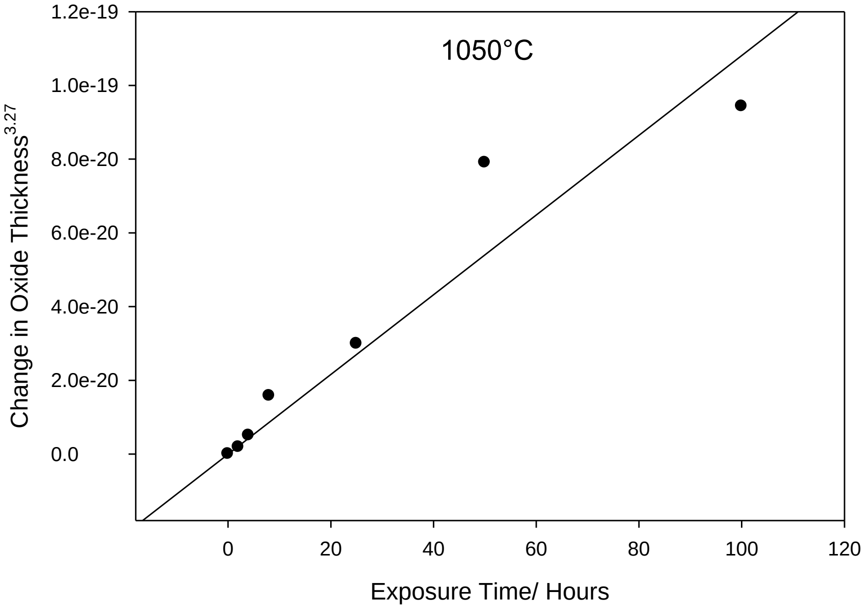
1050°C
Change in Oxide Thickness$^{3.27}$
1.2e-19
1.0e-19
8.0e-20
6.0e-20
4.0e-20
2.0e-20
0.0
0
20
40
60
80
100
120
Exposure Time/ Hours

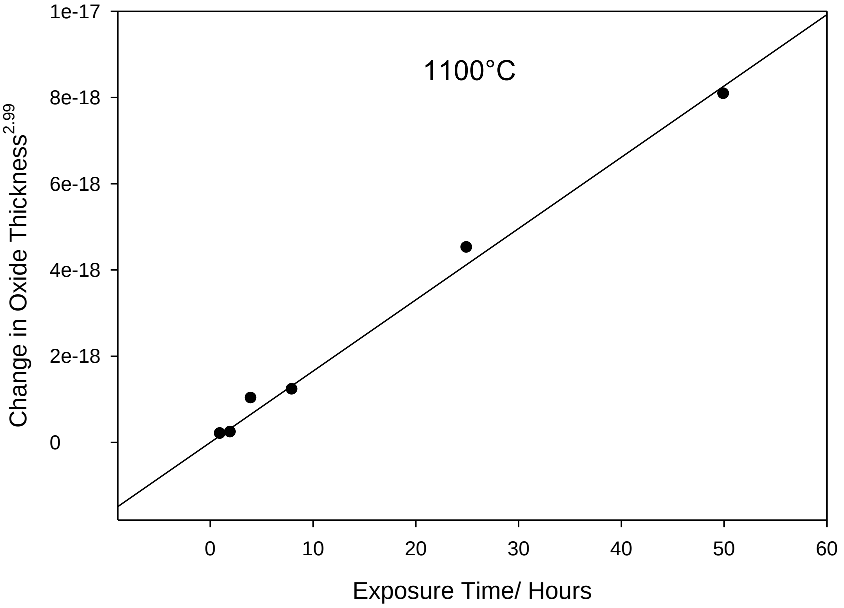
1100°C
Change in Oxide Thickness$^{2.99}$
1e-17
8e-18
6e-18
4e-18
2e-18
0
0
10
20
30
40
50
60
Exposure Time/ Hours

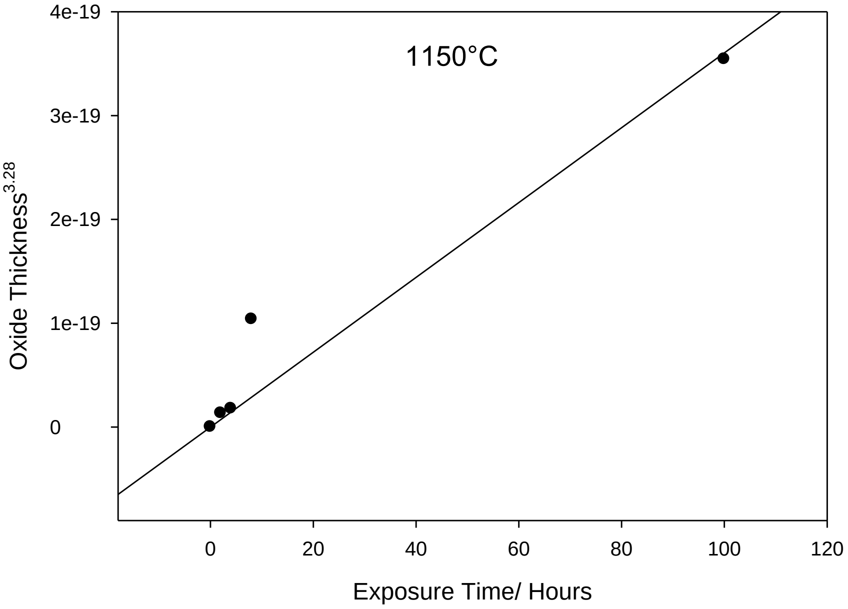

Figure 6.5: Plots for the determination of individual k_n values as each test temperature, results are displayed in table 6.1

Table 6.3: Experimentally determined kinetic parameters and pseudo-parabolic parameters from equation 6.1 for the HVOF NiCoCrAlY bond coat.

Temperature, °C	Time exponent n	Measured rate constant, k_n, m^ns^{-1}	Pseudo-parabolic rate constant, k_p, m^2s^{-1}
950	2.31	1.68×10^{-20}	9.33×10^{-19}
1000	3.18	6.93×10^{-25}	5.86×10^{-18}
1050	3.27	3.53×10^{-25}	6.38×10^{-18}
1100	2.99	4.93×10^{-23}	1.92×10^{-17}
1150	3.28	1.47×10^{-24}	1.34×10^{-17}

These values were used to produce oxide growth equations specific for each temperature by inserting the appropriate values of n and k_n into equation 6.1. Additionally taking a weighted mean of n to be 2.5 it is possible to produce a global temperature invariant equation from equation 6.1, equation 6.2. This allows for the calculation of a predicted oxide thickness at any time and temperature within the test range.

$$\xi = \left(2.61\times10^{-12}\exp\left(\frac{-216881}{RT}\right)\times t\right)^{\frac{1}{2.5}} + 0.49\times10^{-6} \tag{6.2}$$

It can be appreciated that the differing values of n and k_n for each test temperature preclude comparison within the data and with other published work. In order to permit such a comparison, the kinetics were assumed to be parabolic at all temperatures, i.e. n=2 in equation (6.1), and the best-fit parabolic rate constant, k_p, was evaluated for each data set, these values are given in table 6.3. This is a similar procedure to that used by Hindam and Whittle [136] when comparing the oxidation kinetics from diverse sources. The values of k_p for the present results are given in table 6.3 and plotted in the Arrhenius plot of figure 6.6 together with the mean trend line for a variety of alumina formers obtained from Hindam and Whittle[136]. It can be seen that the present data fit reasonably well to Hindam and Whittle's findings and indicates that the characteristically good protection offered by α-alumina is present in the TGO system tested here.

$$\mathrm{k_p} = 7.56\times10^{-7}\exp\left(-\frac{275000}{8.314\mathrm{T}}\right),\ \mathrm{m^2s^{-1}} \tag{6.3}$$

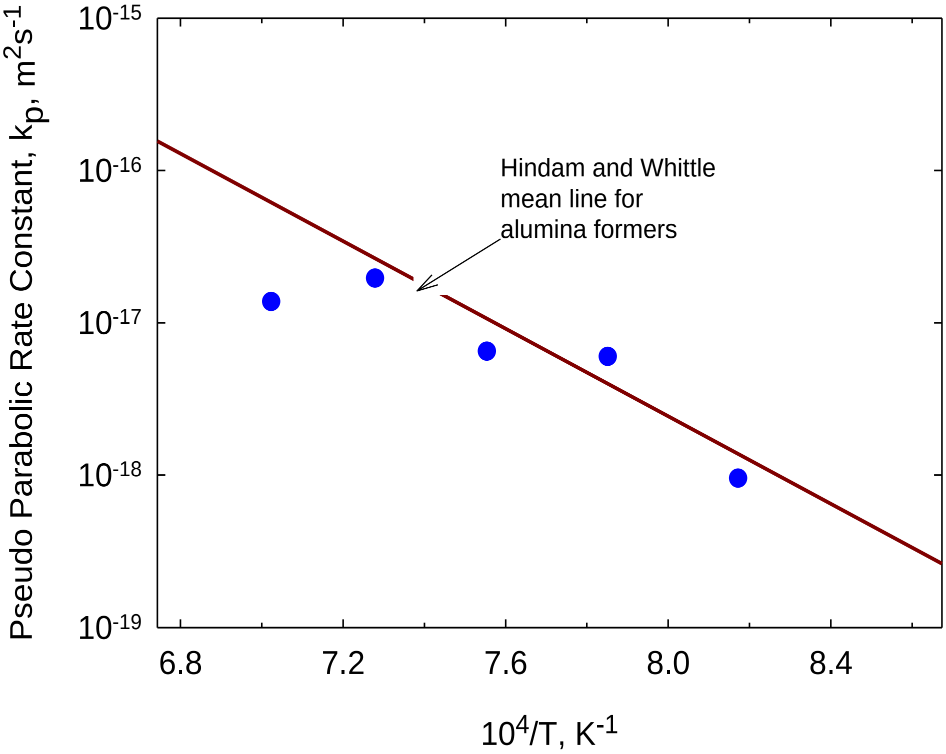

Figure 6.6: A comparison of the pseudo-parabolic rate constants fitted to the present data with the mean trend line for alumina-forming alloys obtained from the compilation by Hindam and Whittle[136].

6.4 *Bond coat Surface Roughness (Topography)*

Surface roughness at the TGO/ bond coat interface has been linked in the literature to numerous failure mechanisms including surface rumpling[120, 137-139]. However, as described in section 4.9 there is no substantial evidence to date of surface rumpling in systems containing a topcoat and / or a strong bond coat. The following results show the wavelength and amplitude of the bond coat before and after oxidation in selected specimens and were measured using the procedure described in section 5.5.

Analysis of the surface roughness from data obtained from the experiments as described in section 5.5 follow in the next two sub-sections. Firstly the amplitude and wavelength measurements taken from the as received specimen and a specimen oxidised isothermally for 100 hours at 1050°C. This is followed by a more detailed analysis of measured roughness average values performed on thermal cycled specimens.

6.4.1 Wavelength and Amplitude Measurements

The wavelength and amplitude of the bond coat surface roughness was measured from low magnification scanning electron micrographs of cross sections of two specimens with a NiCoCrAlY bond coat with attached YSZ topcoat as described in section 5.5. The two specimens examined were an as-received, untested specimen to get a base line measurement of the roughness prior to testing and a specimen oxidised isothermally for 100 hours at 1050°C. An example of the images used can be seen in figure 6.7. On examination of these specimens it was found that two scales of roughness were evident depending upon the magnification used. Firstly at a higher magnification a short range roughness was observed as indicated in figure 6.7. At a lower magnification a long range roughness or “waviness” was observed as seen in figure 6.8.

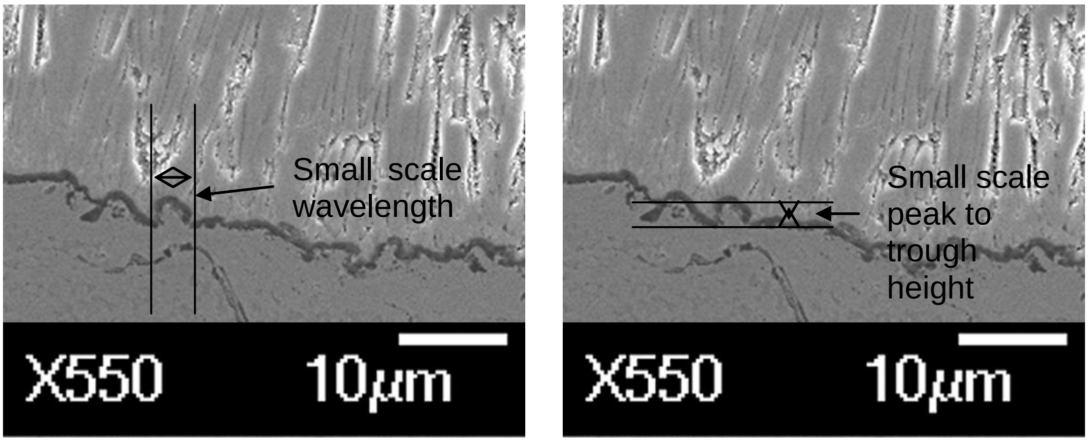

Figure 6.7: SEM micrographs of an as-received specimen showing measurements of the wavelength and amplitude of the small scale roughness.

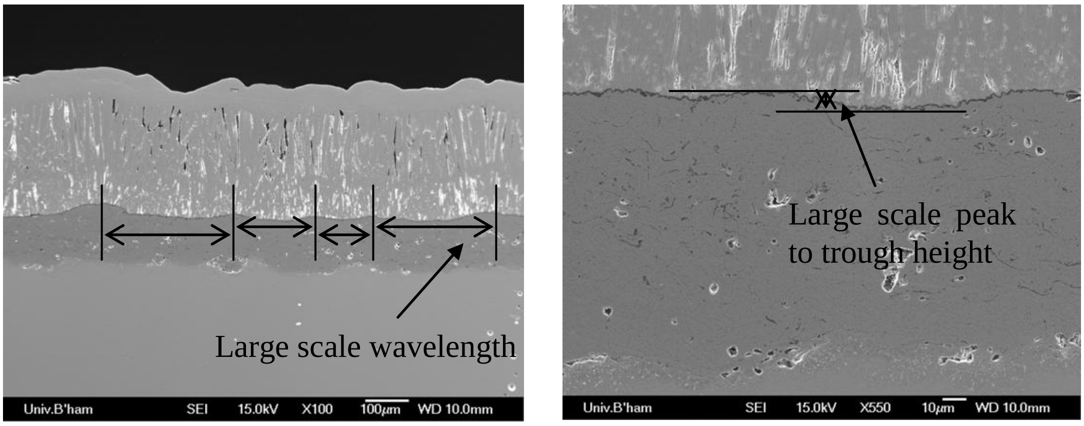

Figure 6.8: Scanning Electron Micrographs of sections through an as-received specimen showing the wavelength and amplitude measurements taken of the large scale roughness.

A small number of measurements, six in total, were taken of the wavelength and amplitude for both scales of roughness, table 6.4.

No significant difference between the as-received and oxidized specimens were observed, with any small differences being attributed to the resolution and accuracy of the method used in examination. Roughening of a bond coat surface upon oxidation is a well documented effect, in the absence of a topcoat and on relatively weak bond coats and substrates; these allow for deformation and creep to occur[67, 88, 120, 137-142]. The lack of this effect in this system is likely due to the mechanical constraint provided by the topcoat and the high creep strength of the bond. Further discussion with respect to the significance of these results can be found in section 8.8 of this thesis.

Table 6.4: Roughness amplitude and wavelength measurements of the bond coat for as received specimen and 100 hour oxidised samples at 1050°C. Samples with HVOF applied NiCoCrAlY bond coat.

		As-received	100 hours at 1050°C
Average small scale peak to trough height(μm)	6 Measurements	2.28	1.97
Average large scale peak to trough height(μm)	6 Measurements	16.12	18.15
Average small scale wavelength (μm)	6 Measurements	3.82	3.42
Average large scale wavelength (μm)	6 Measurements	199.58	203.61

6.4.2 Thermal Cycling

In order to assess the role of the topcoat on the suppression of rumpling in this coating system thermal cycle testing as described in section 5.5 was carried out. This would further examine the tendency of the HVOF applied NiCoCrAlY bond coat to roughen. This procedure involved 1 hour cycles, on a half sized sectioned specimen where the topcoat had further been mechanically removed from half of the specimen, at 1170°C until failure of the coating. An identical specimen half was stored and examined without exposure to provide a means for comparison. Roughness average values were measured as a basis for comparison of the specimen. It should be noted at this stage that obtaining a reference line for measurement of R_a was complicated greatly in these specimens by an uneven internal layer structure and as such the results obtained have a high standard deviation as shown in figure 6.9. For clarification of the results shown in figure 6.9, the term “topcoat removed” refers to the section part where the topcoat was mechanically removed. The term “topcoat intact” refers to the part of the specimen where the topcoat was left intact prior to cycling.

The results as shown in figure 6.9 show that there is no significant difference between the roughness of the specimen before and after thermal cycling. However a large difference can be seen between the areas with topcoat attached and the areas where the topcoat had been mechanically removed, with the intact section showing a greater roughness. This can be attributed to the difficulties in attempting to match the surface profile obtained from the spraying procedure using mechanical methods. The method used here to measure the roughness, by its nature of using relatively low magnification images, measures the large scale roughness referred to in section 6.4.1. It is this scale of roughness which is impossible to replicate using mechanical means as used for this testing.

These results indicate that whilst every opportunity was given in terms of cycling time and temperature no evidence of surface rumpling was seen. This could be attributed as described above to the creep strength of bond coat and substrate which does not permit significant deformation during thermal cycling. Equally however, factors such as microstructral stability of the bond coat could be important as no evidence of phase changes at the bond coat/TGO interface were observed. This is thought to be a contributing factor to surface rumpling.

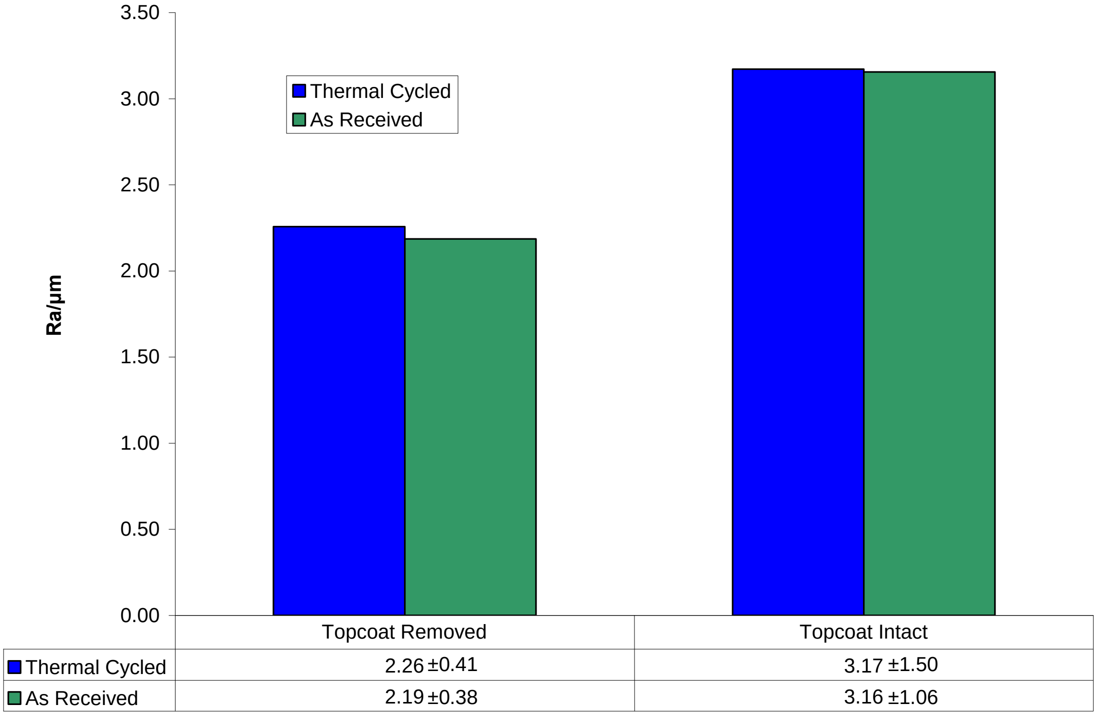

	Topcoat Removed	Topcoat Intact
■ Thermal Cycled	2.26 ±0.41	3.17 ±1.50
■ As Received	2.19 ±0.38	3.16 ±1.06

Figure 6.9: Plot of the roughness average values (Ra) measured before and after thermal cycling to failure at 36 hours at a temperature of 1170°C for samples with a HVOF bond coat

6.5 Microstructure and Composition

The microstructure and compositional development of both the TGO and bond coat are important factors potentially to coating lifetime. This section will examine first the bond coat microstructure and composition followed by that of the TGO. Examination was carried out by a number of techniques, as described in section 5, including scanning electron microscopy, energy dispersive spectrometry (EDS) and x-ray diffraction.

6.5.1 HVOF NiCoCrAlY Bond Coat

The general structure of the HVOF applied bond coat was essentially dual-phase, consisting of β-phase particles in a largely γ-phase matrix. This is shown in figure 6.10 along with the average compositions of each phase determined using EDS measurements from several points across each phase in the centre of the bond coat. These measured compositions were compared to the Ni-Cr-Al ternary phase diagram to identify the phases, section 8. However an added complication to this is the high concentration of cobalt in the bond coat. There is no quaternary phase diagram available for this system and combination of Ni and Co into a pseudo-ternary phase diagram is unsatisfactory, since each has a different effect on γ′ phase stability. The NiCrAl ternary phase diagram, figure 8.10, is used as an approximation in this discussion for guidance.

Even in the as-received condition a narrow β-depleted zone existed at the TGO/ bond coat interface as shown in figure 6.11(a). It is a consequence of aluminium depletion due to the formation of the alumina TGO during the topcoat deposition stage. As expected, this depleted zone increased in thickness with increasing time at temperature due to further depletion of aluminium as the alumina TGO continues to grow, figure 6.11b

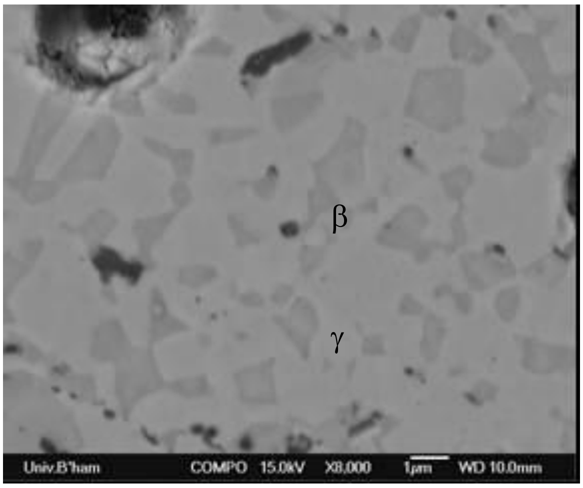

β-phase in wt %

Al	Cr	Co	Ni	Y
17.4	9.8	21.9	50.3	0.6

γ-phase in wt %

Al	Cr	Co	Ni	Y
5.8	22.6	33.9	37.5	0.1

Figure 6.10: Scanning electron micrograph of a section through a TBC with HVOF applied NiCoCrAlY bond coat oxidised for 8 hours at 1150°C and air cooled outside of the furnace showing the two phase structure and detailing the average phase compositions.

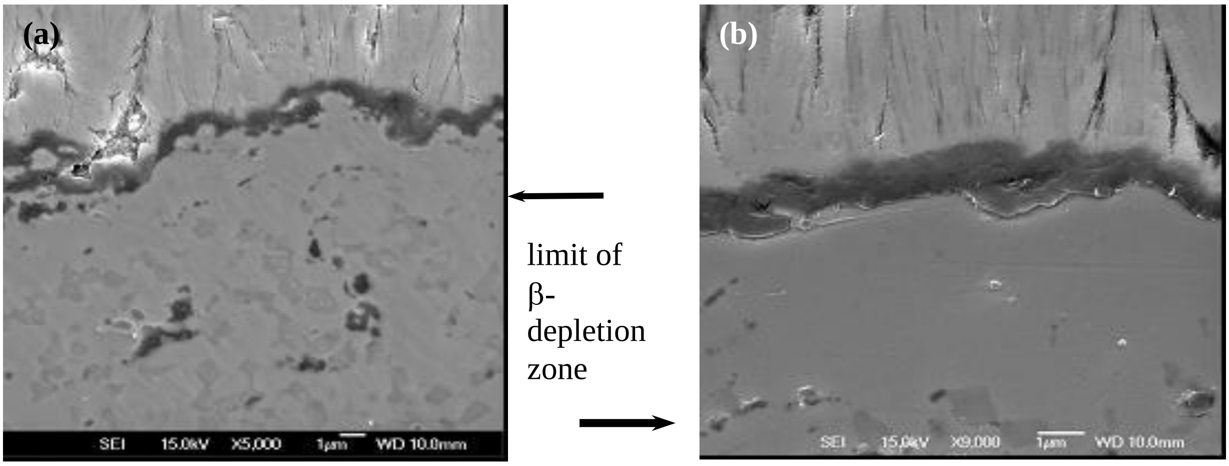

Figure 6.11: Scanning Electron Micrographs of a section through specimens showing the extent of β-phase depletion within the bond coat in the vicinity of the TGO in (a) an as-received specimen and (b) after 25 hours at 950^{o}C.

From the NiCrAl phase diagrams, figure 8.10, it can be seen that the γ′ phase field shrinks with increasing temperature. This could perhaps explain the presence of only β and γ phases in these coatings as the γ′ phase field at test temperature will be relatively reduced coupled to the relatively fast cool from temperature not permitting an equilibrium microstructure to form.

This hypothesis was tested by conducting a slow cooling and water quenched experiment. The specimens that were slow cooled were allowed to do so within the furnace after oxidation for 8 hours at 1150°C; this took several hours to reach room temperature as recorded by the furnace temperature thermocouple but not a directly attached thermocouple. The quenched specimens were again held at 1150°C for 8 hours before being quenched in cold water back to room temperature. These specimens were sectioned and the bond coat microstructure analysed. Table 6.5 gives the compositions of the bond coat phases for the slow cooled, normal cooled and water quenched specimens.

Table 6.5: Bond coat phase compositions after 8 hours at 1150°C and cooling under different regimes showing the effect of cooling rates.

β Phase

	Composition (wt%)				
Cooling	**Al**	**Cr**	**Co**	**Ni**	**Y**
Slow Cooled	17.91	10.66	20.92	50.39	0.13
Normal Cool	18.73	9.22	21.44	50.35	0.26
Water Quenched	17.45	9.82	21.85	50.33	0.55

γ Phase

	Composition (wt%)				
Cooling	**Al**	**Cr**	**Co**	**Ni**	**Y**
Slow Cooled	4.21	24.28	36.03	35.67	0
Normal Cool	5.25	24.16	36.30	33.89	0.40
Water Quenched	5.84	22.57	33.91	37.54	0.14

As can be seen from table 6.5 there is no significant difference in the composition of the phases related to different cooling regimes employed. This demonstrates that the compositions measured at room temperature are the same as those that exist at temperature for this system. Therefore the compositions and microstructure observed is likely to be the near equilibrium microstructure.

6.5.2 TGO composition

Analysis of the TGO developed at temperature, using XRD analysis, shows the formation of solely α-alumina. These measurements were taken from sections of spalled topcoat which retained the TGO. The sections were positioned in the XRD such that the TGO was exposed and low angles were used to limit penetration into the YSZ, an example of one such trace is shown in figure 6.12. This plot shows the presence of α-alumina peaks, ZrO_2 peaks but significantly the absence of any transitional alumina peaks. This result was as predicted as the specimens had received a pre-treatment at temperatures which would encourage the formation of α-alumina.

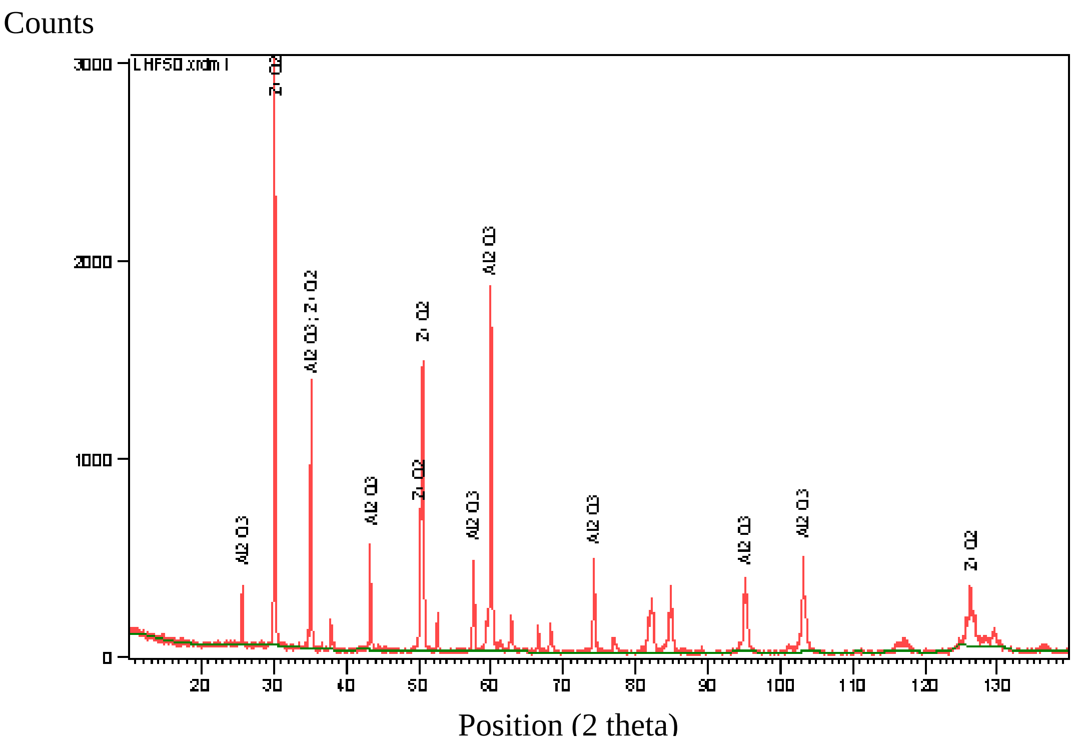

Figure 6.12: XRD spectrum of spalled ceramic topcoat with TGO attached from a specimen oxidised at 1150°C for 50 hours showing the principal peaks of α-alumina and zirconia. The remaining unidentified peaks can be attributed to minor peaks of α-alumina, zirconia and yttria.

6.6 Cracking and Failure

During the detailed scanning electron microscopy examination of all the specimens, an examination of the entire TGO was undertaken to look for the presence of any cracking which may be present. Additionally the morphology of any large scale cracking and the time to failure was recorded for all specimens where total coating failure occurred. A summary of the observed cracking and coating failure is given along with the oxide thicknesses in table 6.1. For the purpose of this project, initially a criterion of TBC failure was that greater than 20% of the topcoat had spalled. However it was observed that when failure of the coating occurred the complete ceramic topcoat and TGO would crack away typically in one piece, these specimens were described as “spalled” in table 6.2. On examination of some long life specimens after cross-sectioning it was further observed that full length cracks had occurred and as such the coating was classified as failing and described as “delaminated” in table 6.2. The results of the cracking observation for the HVOF applied NiCoCrAlY bond coat will be presented in the following section along with additional comments and explanation. A full examination of the significance of these observations can be found in section 8.7. The results are split into two sections, firstly an examination of cracking which did not lead directly to failure, called sub critical cracking and then an examination of coating final failure.

6.6.1 Early Sub-critical Cracking

Examination of sections of a range of specimens oxidised at different times at temperature demonstrated the presence of two distinct cracking mechanisms in these coatings. At relatively short times at 1050°C small cracks could be identified at the TGO/topcoat interface region and these extended within the topcoat and TGO. Examples are shown in figure 6.13 for the relatively short time of 2 hours at 1050°C. These cracks could be short, typically between 1-2μm in length, but some had coalesced/linked to form longer defects, as shown in figure 6.13. However, no further progression of these cracks was evident even after considerably longer times at temperature. This indicates that the driving force for the extension of these cracks was limited and, it is suggested, was localised to distances of similar magnitude to the bond coat surface roughness.

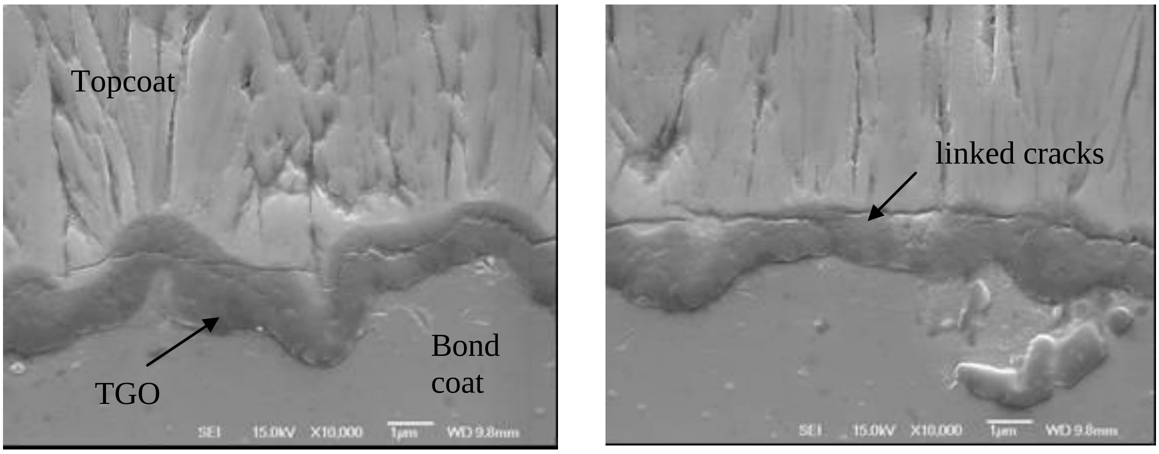

Figure 6.13: Scanning Electron Micrographs of two different areas through a specimen oxidised at 1050°C for 2 hours, showing cracking at the TGO/topcoat interfacial region and within the TGO.

Stresses of this type have been shown by finite element analysis of models of similar systems to occur near the flanks of asperities/roughness in the TGO at temperature [143, 144]. These show how the volumetric strains associated with the growth of the TGO result in the development of out-of-plane tensile stresses at the oxidation temperature. The severity of the stresses is increased by an increase in aspect ratio (amplitude/wavelength) of the asperities; therefore in order for these stresses to become significant a relatively high surface roughness is required, figure 6.14. The results from section 6.5 demonstrate that this coating system has a relatively high surface roughness. These stresses are located within the topcoat near the flanks of bond coat protuberances and extend over a relatively small distance as shown in figure 6.14[144]. On the basis of these results, it is suggested that the cracks shown in figure 6.13 nucleated within the topcoat at temperature but have limited scope for propagation, at least for the bond coat surface topology found in the present specimens. In cases where the bond coat protuberances are of high aspect ratio and closer spaced, extended cracking seems possible at the base of the topcoat [106], however the roughness in general in the coating system viewed here was not sufficiently large or too widely spaced to allow significant coalescence of cracks and lead to failure. It is expected that crack development is also aided by out-of-plane tensile stresses developed during cooling [106].

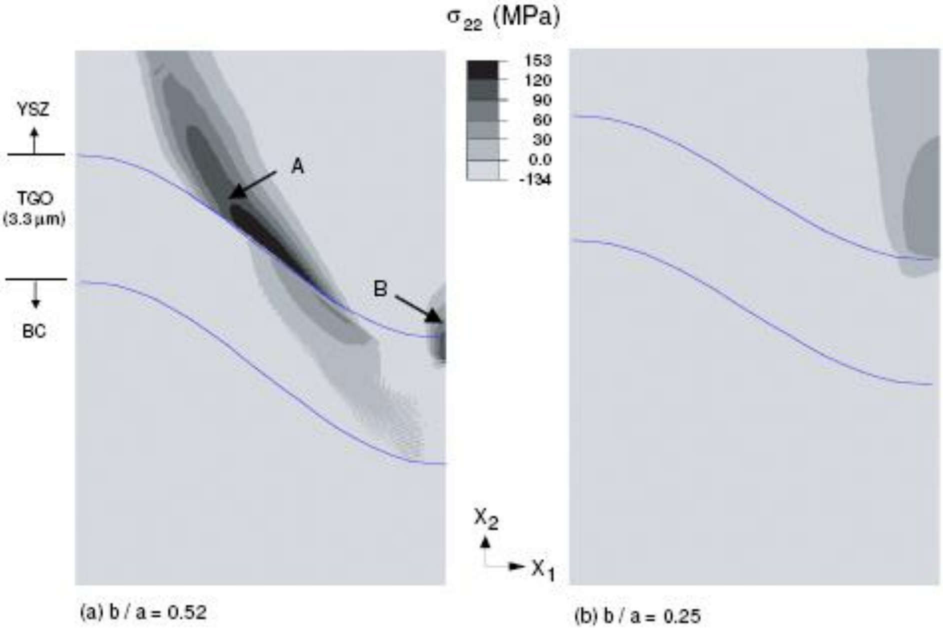

Figure 6.14: Contour of maximum out-of-plane principal stress near the TGO layer at 1100 °C after 100 hours oxidation at 1100 °C in a TBC system when BC and TGO creep behaviour and topcoat sintering are considered. (a) b / a = 0.52 and (b) b / a = 0.25 [144].

6.6.2 Coating Failure

At longer times, extensive cracking was seen at the bond coat/TGO interface, which leads to spallation or delamination of the ceramic topcoat and TGO from the bond coat. This enabled XRD analysis to be made of the then exposed TGO. Figure 6.15 shows an example of this crack development which occurred late in life. In the example given in figure 6.15 complete spallation had not occurred but the crack was extensive and ran the full width of the specimen.

Ultimately it is this cracking mechanism that leads to failure of the coating in all cases except at 950°C where failure did not occur over the time frame of the project. The failure seen at the other temperatures tested demonstrates that the release of strain energy within the TGO could be a significant driving force in the fracture process.

Large stresses are generated within the TGO specifically during cooling to room temperature, equation 6.4[61] gives an expression for calculating the strain energy generated within an oxide during cooling.

$$W^* = E_{ox}h(1-\nu_{ox})(\Delta T)^2(\Delta\alpha)^2 \tag{6.4}$$

W^*= Strain Energy
E_{ox}=Young’s Modulus of the oxide
h=Oxide thickness
ν_{ox}= Poisson’s ratio of the Oxide
ΔT= Change in Temperature
$\Delta\alpha$= Difference in thermal expansion co-efficient

Using values of,
E=367GPa
ν_{ox}=0.3
ΔT= 1000K
α-Alumina = $7.9\text{x}10^{-6}$ $\mathrm{K}^{-`1}$
α-CMSX-4 Substrate = $2.0\text{x}10^{-5}$ $\mathrm{K}^{-`1}$
α-NiCoCrAlY Bond coat = $1.52\text{x}10^{-5}$ $\mathrm{K}^{-`1}$
α-YSZ Topcoat = $1.03\text{x}10^{-5}$ $\mathrm{K}^{-`1}$

For an oxide thickness at 1μm the strain energy generated between the TGO and substrate would be 37.6Jm^{-2}. The work of adhesion for alumina on a Ni surface has been calculated to be 0.66 J/m^{-2}[62], which is clearly well below the generated strain energy. Therefore it can be deduced that a mechanism for relaxation of these strain energies must exist. This mechanism is likely to take advantage of creep within the bond coat which could absorb these stresses through deformation. Further discussion on this can be found in section 8.

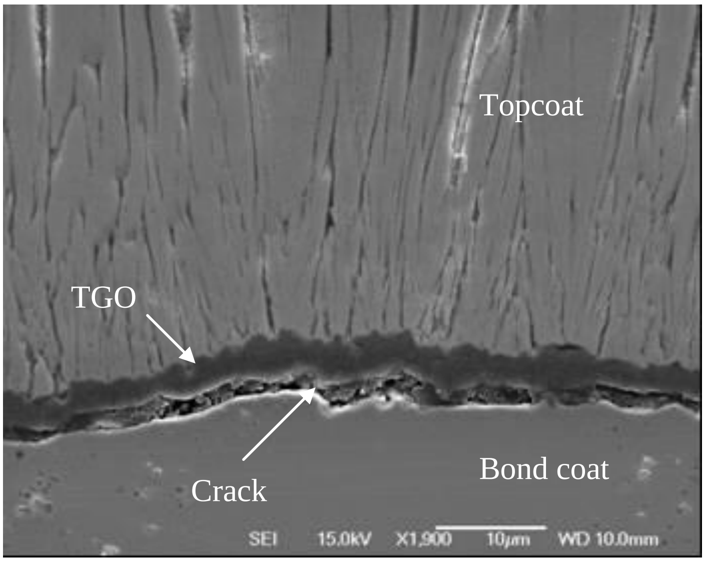

Figure 6.15: Scanning electron micrograph of a specimen oxidised at 1150°C for 25 hours, demonstrating an extensive crack at the bond coat/TGO interface.

Times to failure have been recorded for four temperatures out of the five tested as no failure was observed at 950°C over the timescale of the experiment. These data and those for the TBC system with the EBPVD bond coat are presented in Section 8 in the context of TBC lifetimes of conventional production-quality coatings available from the literature.

7 RESULTS FOR THE TBC WITH THE EBPVD APPLIED BOND COAT

7.1 Introduction

This section contains the results of the testing described in section 5 on the TBC system with the EBPVD NiCoCrAlY bond coat. A comparison of the two coating systems is made in the discussion section 8 which will also include information from the literature.

The presentation of the results in this section will follow the same format used in section 6 for ease of comparison. Thus to begin with the TGO thickness measurements will be shown followed by the kinetics derived from these data. Microstructure, composition, bond coat surface roughness measurements, etc. are then covered to more fully characterise the coatings and aid identification and elimination of possible failure mechanisms.

7.2 Oxide Thickness Distribution

As with the TBC specimens containing a HVOF NiCoCrAlY bond coat, the oxide thickness measurements on all the TBC specimens with the EBPVD NiCoCrAlY bond coat supplied by Finspong were found to fit a normal Gaussian distribution. Figure 7.1 show examples of the curves produced from specimens oxidised for 4 and 25 hours at 950, 1050 and 1150°C. These plots are of the actual data points, which have been plotted over a fitted normal distribution curve based on the data. The fit of the data to the curve is excellent across the whole range of measured thicknesses. This demonstrates that there are no detected areas of excessively thick oxides on the surface and therefore the TGO is relatively uniform in thickness across the surface. The lack of excessively thick oxides demonstrates that the TGO is also uniform in composition with no evidence of rapid growing oxides or spinels; this demonstrates good protection by the TGO to the underlying bond coat.

These plots also show the increase in the standard deviation observed with increasing time at each temperature as also seen for the HVOF bond coat. This effect is likely due to regions of alumina growing at a consistently faster rate than neighbouring regions which continue to grow at a slightly slower rate. The range of growth rates observed are within that recorded for alumina growth, as will be shown in section 7.3 and 8.3. This effect, in principle, could also be due to an increase in surface roughness with increasing oxide thickness, the subsequent geometrical effect of sectioning a rough oxide would show an increase in the variation in oxide thickness with some very thick oxides showing on the sides of flanks.

Table 7.1 gives the mean, together with ± 2-standard deviations, of the measured TGO thicknesses at the test times and temperatures. This presentation of the data further highlights the observed increase in standard deviation with increasing time at temperature. However, it can also be seen from these data that there is no correlation between the specific oxide thickness and the standard deviation value, for example at a time of 25 hours the standard deviation value at the three test temperatures is 0.51, 0.47 and 0.64μm respectively. This makes it unlikely that this effect of increasing standard deviation with increasing time at temperature is a geometrical effect as described above. Additionally no increase in surface roughness has been seen as described in section 7.4.

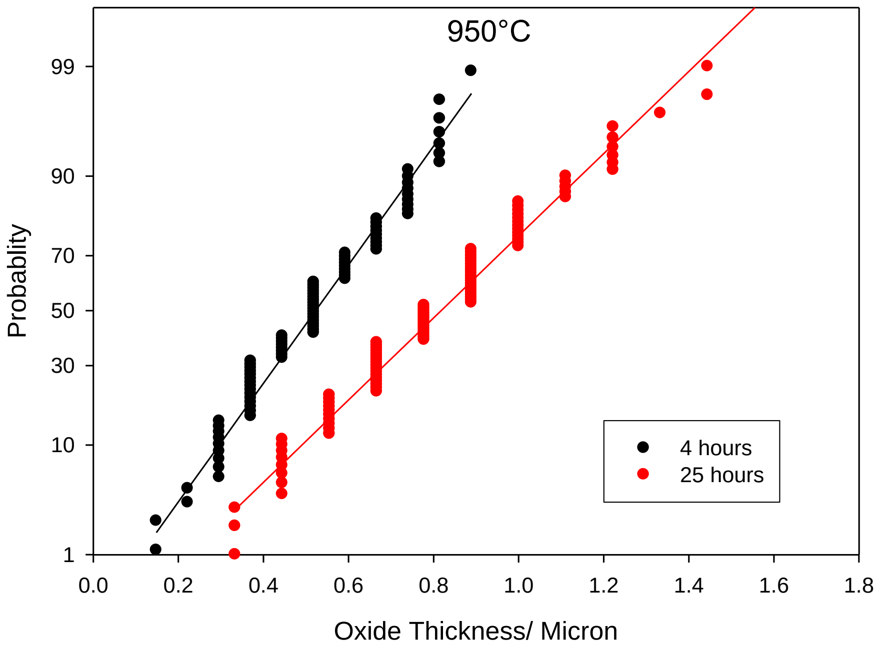
950°C
Probablity
99
90
70
50
30
10
1
0.0
0.2
0.4
0.6
0.8
1.0
1.2
1.4
1.6
1.8
Oxide Thickness/ Micron
● 4 hours
● 25 hours

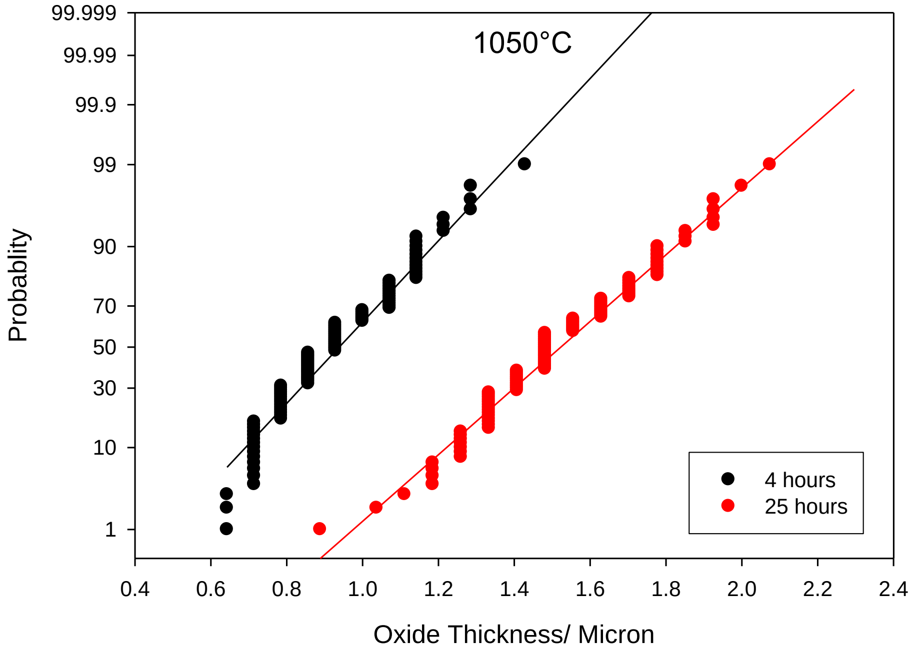
1050°C
Probablity
99.999
99.99
99.9
99
90
70
50
30
10
1
0.4
0.6
0.8
1.0
1.2
1.4
1.6
1.8
2.0
2.2
2.4
Oxide Thickness/ Micron
● 4 hours
● 25 hours

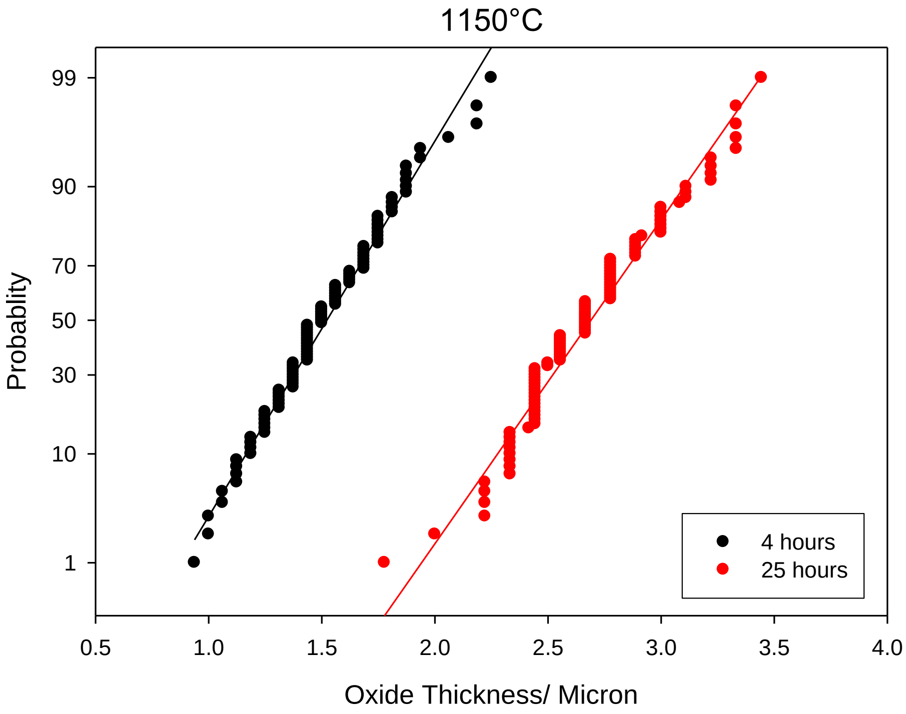

Figure 7.1: Probability plots of the oxide growth distribution of Finspong TBC specimens with an EBPVD bond coat oxidised for 4 and 25 hour at 950, 1050 and 1150°C

Table 7.1: Mean and 2 standard deviations of the TGO thicknesses for the Finspong TBC specimens with an EBPVD bond coat at all times and temperatures, taken from 100 measurements per specimen. A summary of the cracking and spallation observations are also included.

Time/ h	950°C	1050°C	1150°C
0	0.42 ± 0.28μm	0.42 ± 0.28μm	0.42 ± 0.28μm
1	NOT TESTED	NOT TESTED	1.08 ± 0.46μm
2	NOT TESTED	0.82 ± 0.44μm	1.33 ± 0.41μm
4	0.52 ± 0.35μm	0.94 ± 0.39μm	1.52 ± 0.56μm
8	0.70 ± 0.48μm	1.08 ± 0.41μm	SPALLED
25	0.82 ± 0.51μm	1.52 ± 0.47μm	2.69 ± 0.64μm
50	1.00 ± 0.52μm	1.93 ± 0.56μm	DELAMINATED
100	1.23 ± 0.57μm	2.29 ± 0.87μm	SPALLED
240	1.45 ± 0.53μm	SPALLED	NOT TESTED
500	1.68 ± 0.58μm	SPALLED	NOT TESTED
1000	1.87 ± 0.68μm	NOT TESTED	NOT TESTED
3000	SPALLED	NOT TESTED	NOT TESTED

🟨	Delaminated at TGO/bond coat interface
🟥	Spallation at TGO/bond coat interface

7.3 Oxidation Kinetics

The initial TGO thickness, as determined from a randomly chosen untested specimen, was found to be 0.42μm, table 7.1. This value for the TGO thickness in the as-received condition was subtracted from the mean TGO thickness determined from Scanning Electron Micrographs for each specimen tested, table 7.1. These adjusted data were used to determine the oxidation kinetics as described previously, using equation 6.1. Figure 7.2 shows the log/log plot of these data, from which can be determined the exponent factor, n.

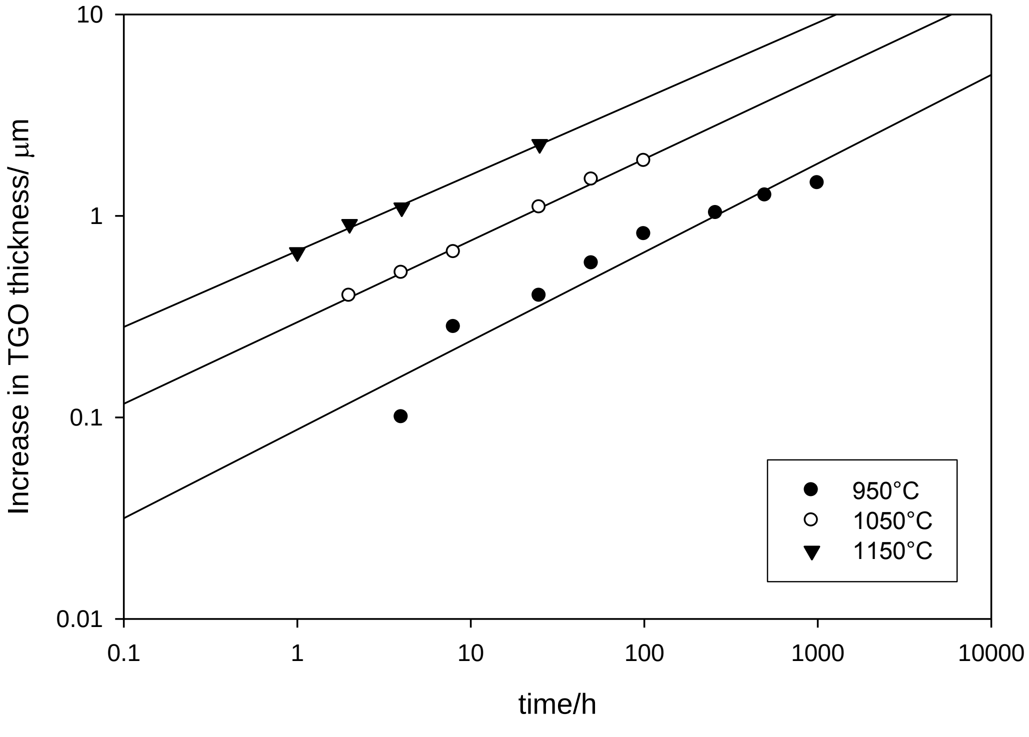

Figure 7.2: Log-log plot of data from table 7.1 used to obtain growth rate kinetics exponents.

The measured values of the exponent n from figure 7.2 obtained using equation 6.1 are given in table 7.2. This shows a small temperature dependence of n from a value of 2.3 to a maximum of 2.6. This small temperature dependence means that interpolation to other temperatures within this range adds a slight complication for extrapolation of the results but provides an adequate basis for the derivation of a general kinetic equation. An approach to providing a single equation to describe the TGO growth behaviour over the whole of the test range can be made through the use of a weighted, temperature-invariant value of the exponent, n, of 2.5. Using this value, the best estimates for k_n at each of the test temperatures are given in table 7.2.

Table 7.2: Experimentally determined kinetic parameters for the HVOF NiCoCrAlY bond coat.

Temperature, °C	Time exponent n	Measured rate constant, k_n, $m^n s^{-1}$	Pseudo-parabolic rate constant, k_p, $m^2 s^{-1}$
950	2.3	7.31×10^{-22}	6.81×10^{-19}
1050	2.5	1.36×10^{-20}	1.05×10^{-17}
1150	2.6	8.56×10^{-20}	5.84×10^{-17}

Using equation 7.1 an Arrhenius plot of these rate constants, normalised to n=2.5 was calculated, figure 7.3 and yields a global activation energy of ~347 $kJmol^{-1}$.

$$k_n = k_0 e^{-\left(\frac{Q}{RT}\right)} \tag{7.1}$$

Where k_n is the rate constant, k_0 is the pre-exponential factor, Q is the activation energy for oxide formation, R is the universal gas constant (8.314 $J.mol^{-1}.K^{-1}$) and T is the exposure temperature in Kelvin.

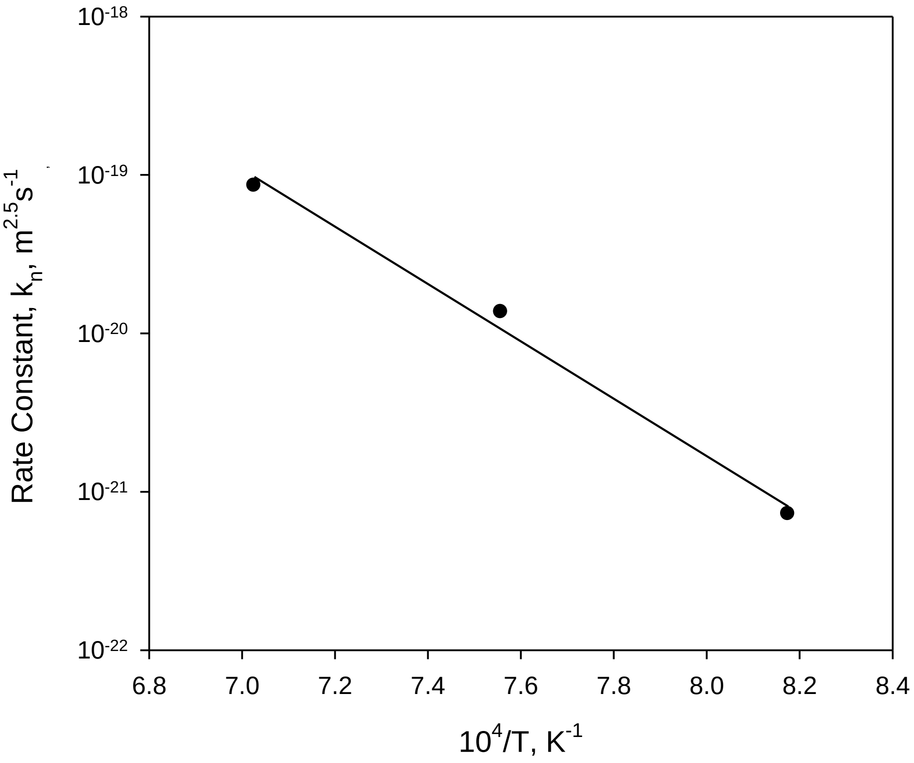

Figure 7.3: Arrhenius plot of the rate constants, k_n, at the three test temperatures, normalised to an n=2.5, producing an activation energy of ~347 kJ.mol^{-1}.

By combining equations 6.1 and 7.1 it was possible to produce an equation that describes the oxidation kinetics of this TBC system as follows:

$$\xi = \left(5.16 \times 10^{-7} \exp\left(\frac{-346652}{RT}\right) \times t\right)^{\frac{1}{2.5}} + 0.42 \times 10^{-6} \tag{7.2}$$

Where ξ is the oxide thickness in m, R is the gas constant, 8.314 J.mol^{-1}.K^{-1}, t is the exposure time in seconds, and T is temperature in Kelvin.

Using equation 7.2 it is possible to predict the oxide thickness for this system given the exposure time and temperature. Figure 7.4 shows the comparison between the predicted TGO thickness from this global equation and the measured values. The agreement is inevitably less good than that found using the specific values of n for each temperature but is, typically, within 10-20% of the measured means and always well within the values of 2-standard deviations given in table 7.1. This equation can thus be used to predict the oxide thickness within the range of times and temperatures study here. The accuracy may be less good outside this range.

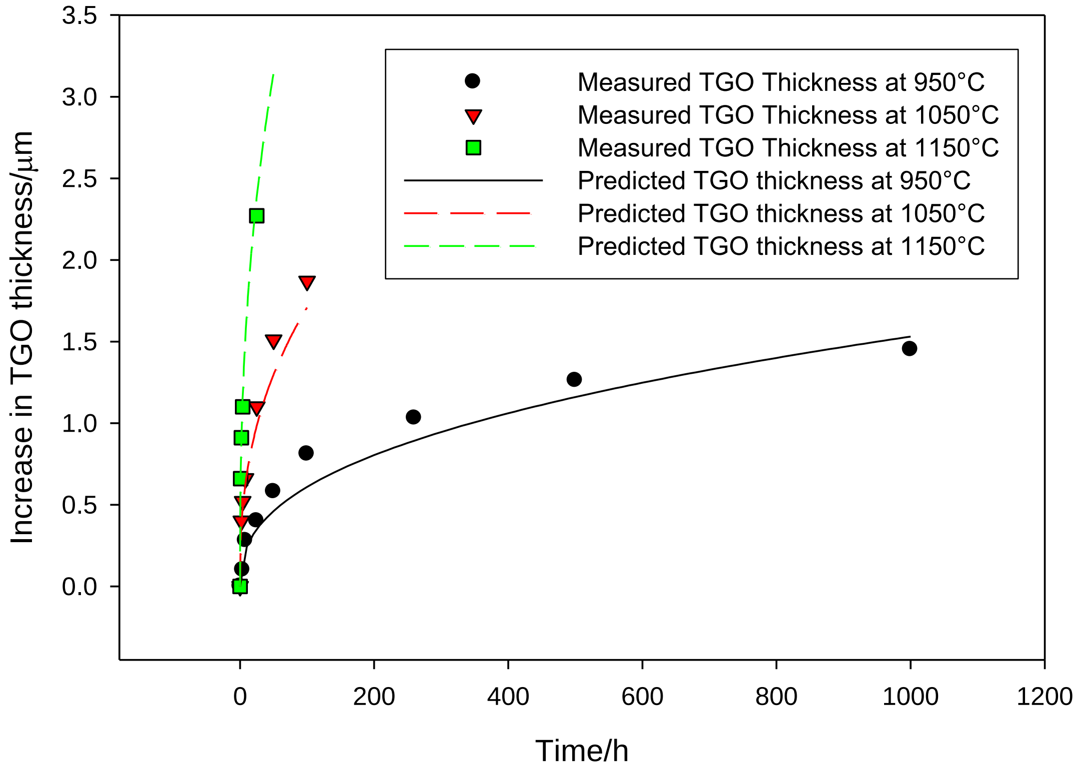

Figure 7.4: Comparison between the predicted increase in TGO thickness with time using the global equation (7.2) and the measured mean values at the three test temperatures.

Table 7.2 shows all the oxidation kinetics variables for this TBC system. From this it can be seen that the values of n were found to be sub-parabolic at each temperature. This is similar to the observations for the TBC coating with the HVOF bond coat, table 6.1. One possible explanation for the sub-parabolic behaviour is the role of grain boundaries in the kinetics of the system. Grain boundaries act as fast diffusion paths (section 2.2.2) and thus, if there is an increase in alumina grain size with increasing time at temperature, there will be a corresponding decrease in the number of grain boundaries available for short-circuit diffusion of oxygen across the oxide and thus a slowing of oxide growth. This will be expanded upon in section 8.3.

These sub-parabolic kinetics provide an additional complication in comparing these data with those from the literature for other alumina forming alloys, where parabolic kinetic behaviour is assumed. As described in section 6.3 one method for overcoming this is by forcing the data to fit pseudo-parabolic kinetics a as described by Hindam and Whittle[136]. When these points are plotted in conjunction with the mean line for typical alumina formers, Figure 7.5, a very good correlation between the two was found. This demonstrates that a fully dense, slow growing α-alumina oxide is likely to be forming in this TBC system.

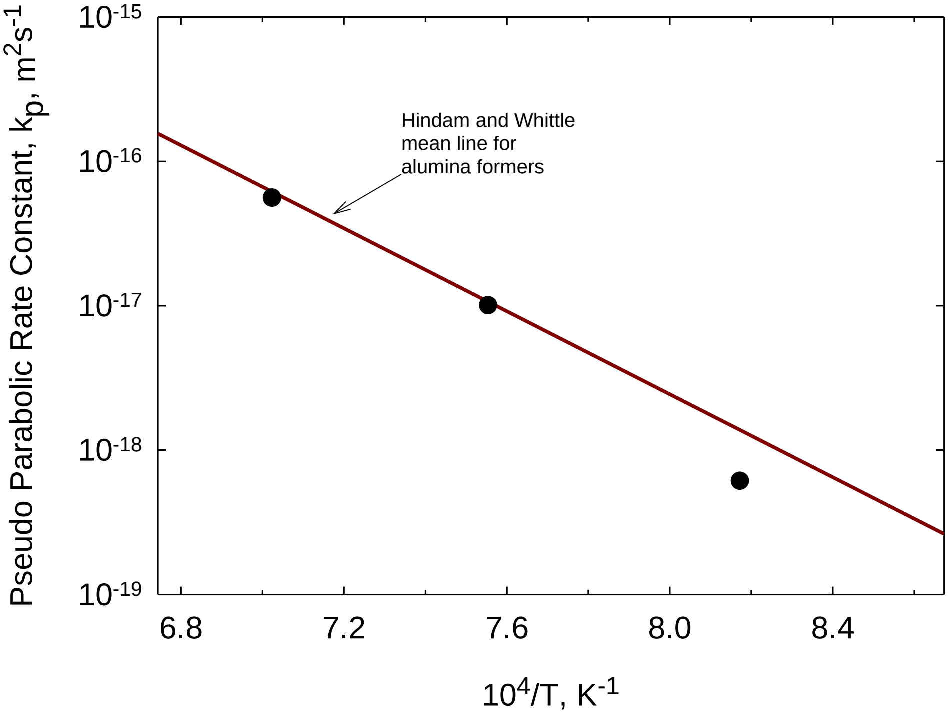

Figure 7.5: A comparison of the pseudo-parabolic rate constants calculated for the TBC with an EBPVD bond coat to the mean trend line for alumina-forming alloys obtained from the compilation of data produced by Hindam and Whittle [136].

7.4 Bond Coat Surface Roughness (Topography)

The bond coat surface roughness was measured using the procedure laid down in section 5.5. For the isothermally tested specimens an indication of the surface roughness was taken from measurements of the wavelength and amplitude whereas the Ra value was calculated for those specimens thermal cycled as described in section 5.5 whereby half of a sectioned specimen was thermal cycled and the other half examined in the as received condition as a control.

7.4.1 Wavelength and Amplitude Measurements

Unlike for the TBC with the HVOF bond coat, no large scale roughness was observed. This is a consequence of the differences in the coating procedures used to produce the two bond coat types. In the case of an EBPVD bond coat, a characteristically smoother surface is produced lacking the large scale undulations noted in the HVOF process. Therefore, only the short scale wavelength and amplitude were present as shown in figure 7.6. Measurements of wavelength and amplitude taken from micrographs are shown in table 7.3.

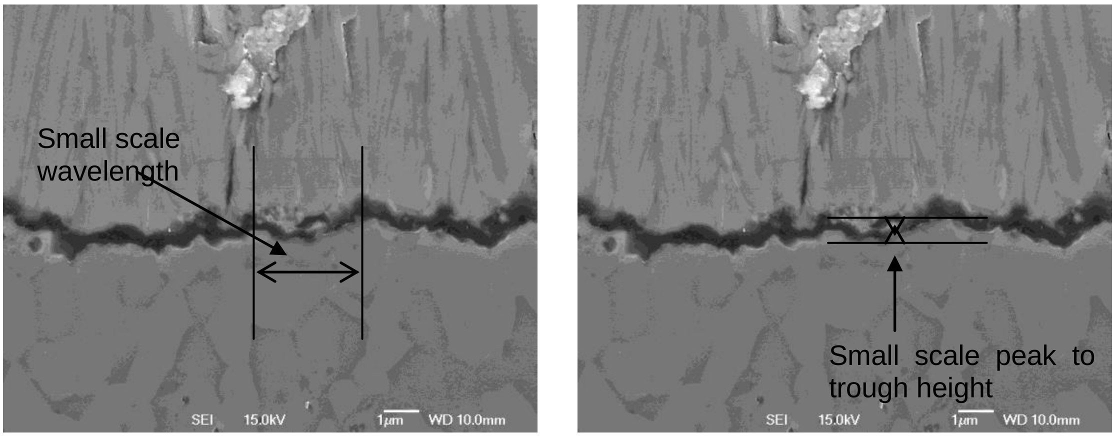

Figure 7.6: Scanning Electron Micrographs through the TBC specimens with the EBPVD bond coat showing the measurements taken of the wavelength and amplitude of undulations of the bond coat outer surface.

Table 7.3: Table showing the wavelength and amplitude measurements and standard deviation for both the as-received specimen and the specimens oxidised for 100 hours at 1050°C.

		As Received	100 hours at 1050°C
Average small scale peak to trough height(µm)	6 Measurements	0.59 ± **0.26**	0.71 ± **0.35**
Average small scale wavelength (µm)	6 Measurements	1.69 ± **0.63**	1.49 ± **0.61**

These results show that there is no significant roughening of the bond coat surface even after 100 hours of isothermal exposure.

7.4.2 Thermal Cycling

In order to assess the role of the topcoat on the suppression of rumpling in this coating system and to examine the tendency for the EBPVD applied NiCoCrAlY bond coat examined here to roughen during oxidation, testing and examination as described in section 5.5 were carried out. This procedure was carried out using 1 hour cycles on a half sized cross-sectioned specimen where the topcoat had further been mechanically removed from half of the specimen, at 1170°C until failure of the coating. An identical specimen half was stored and examined without exposure to provide a means for comparison. Roughness average values were measured as a basis for comparison of the specimen. For clarification of the results shown in figure 7.7, the term “topcoat removed” refers to the section part where the topcoat was mechanically removed. The term “topcoat intact” refers to the part of the specimen where the topcoat was left intact prior to cycling.

The results as shown in figure 7.7 show that there is no significant difference between the areas of the specimen before and after thermal cycling. However a larger difference can be seen between the areas with topcoat attached and the areas where the topcoat had been mechanically removed, with the removed section showing a greater roughness. This difference is the reverse of the HVOF applied coating seen in section 6.4.1 as the EBPVD applied coating is somewhat smoother than the HVOF applied coating. The difference between the sections can be attributed to the difficulties in attempting to match the surface profile obtained from the spraying procedure using mechanical methods. These results indicate that whilst every opportunity was given in terms of cycling time at temperature, no evidence of surface rumpling was seen. This could be attributed to the creep strength of the bond coat not allowing for significant deformation. Equally however factors such as microstructural stability of the bond coat could be important as no evidence of phase changes at the bond coat/TGO interface were observed. This is thought to be a contributing factor to surface rumpling where no topcoat is present.

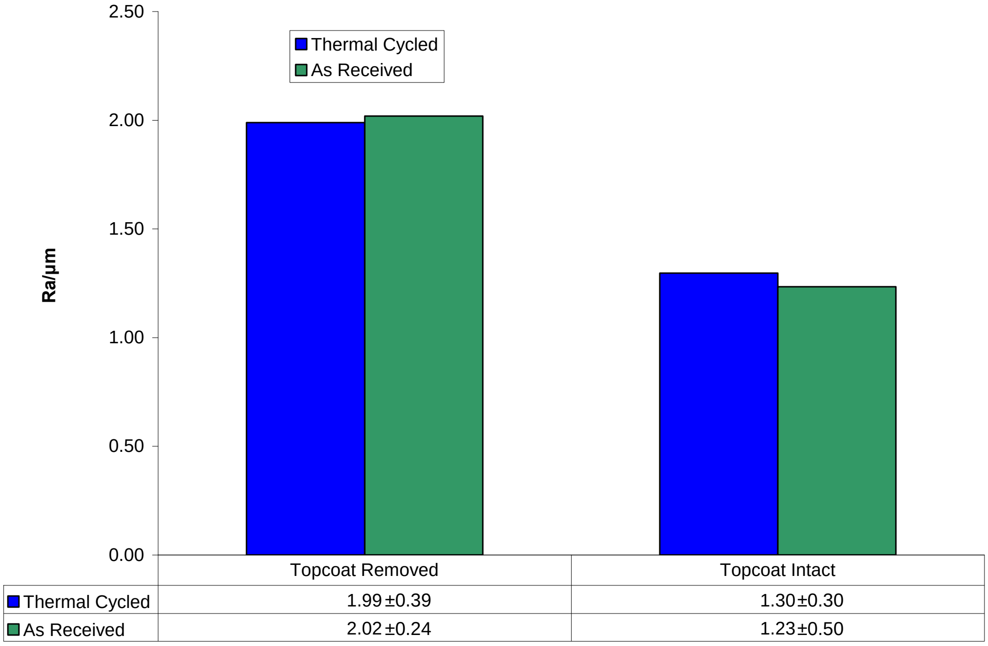

	Topcoat Removed	Topcoat Intact
🟦 Thermal Cycled	1.99±0.39	1.30±0.30
🟩 As Received	2.02±0.24	1.23±0.50

Figure 7.7: Plot of the roughness average values (Ra) measured before and after thermal cycling to failure at 36 hours at a temperature of 1150°C for samples with a HVOF bond coat.

7.5 Microstructure and Composition

7.5.1 EBPVD NiCoCrAlY Bond Coat

A section through a TBC specimen in the as-received condition is shown in figure 7.8. The columnar structure of the EBPVD YSZ topcoat can be seen with an underlying layer of thermally grown alumina, in darker contrast, produced during the coating process to aid adhesion between the topcoat and the bond coat. The duplex β (nominally, NiAl) plus γ (nominally, Ni) structure associated with NiCoCrAlY coatings can be seen. In addition, within the bond coat some α-Cr particles were also identified close to the substrate interface, again in keeping with these coating types. The bond coat is dense, approximately 120 µm thick and shows good adherence with the YSZ topcoat and the substrate. Interdiffusion between the bond coat and the substrate has occurred producing a mixed phase interdiffusion zone, including β (NiAl), due to aluminium diffusion from the coating into the substrate and precipitates of heavier elements derived from the substrate, visible in bright contrast, e.g. Ta, W, and Re.

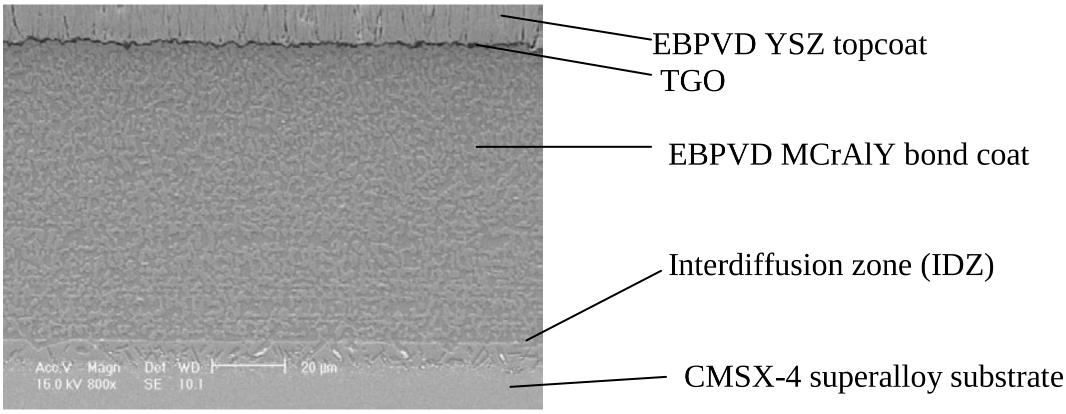

Figure 7.8: Scanning electron micrograph of a section through an as-received specimen, showing the topcoat, TGO, a β (NiAl) + γ (Ni) two phase bond coat, an interdiffusion layer (IDZ) and the substrate.

Examination of sections through tested specimens showed that, with increasing time at temperature, the thickness of the TGO increased with a corresponding increase in the thickness of the β (NiAl)- depleted region of the bond coat adjacent to the oxidising surface (figures 7.9 and 7.10). The interdiffusion zone (IDZ) also continued to develop with time with further heavy-element precipitation and β (NiAl) phase formation.

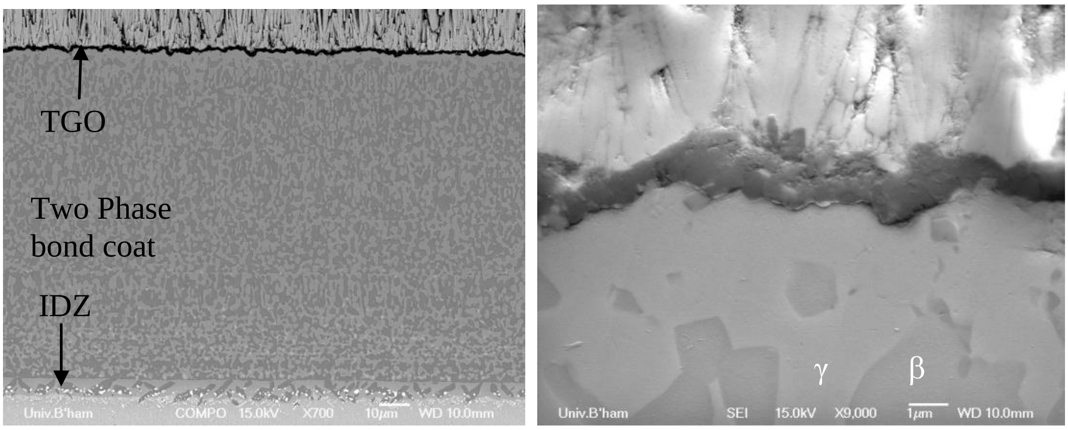

Figure 7.9: Scanning electron micrographs of sections, at low and higher magnification, through a specimen held at 1050°C showing the thick bond coat, IDZ with heavy element precipitates and the mainly two phase bond coat.

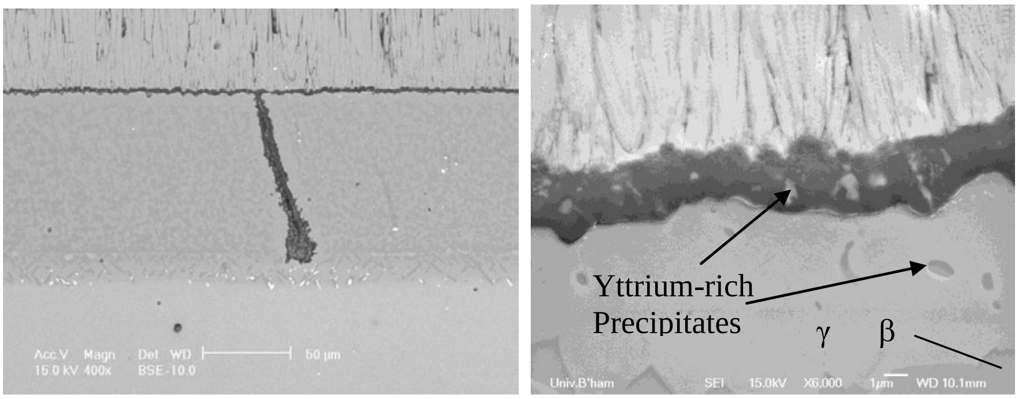

Figure 7.10: Scanning electron micrographs of sections, at low and high magnification, through a specimen held at 1050°C for 100 hours showing further increase in the TGO thickness, an increase in the β-depleted region and increase in the IDZ thickness. In addition, in this specimen, near-vertical full thickness cracks were dispersed throughout the bond coat, some showing signs of oxidation.

7.5.2 TGO Composition

The high-resolution images produced with current SEM technology make it possible to study the structure of the TGO in detail, figures 7.9 and 7.10. The TGO was essentially alumina but it was clear that, with increasing time at 1050 and 1150°C, it contained increasing amounts of another oxide phase, distinguishable by phase contrast, figure 7.11. These phases seemed to form pegs into the bond coat in the specimens tested at 1050 and 1150°C but were not seen in the specimens tested at 950°C.

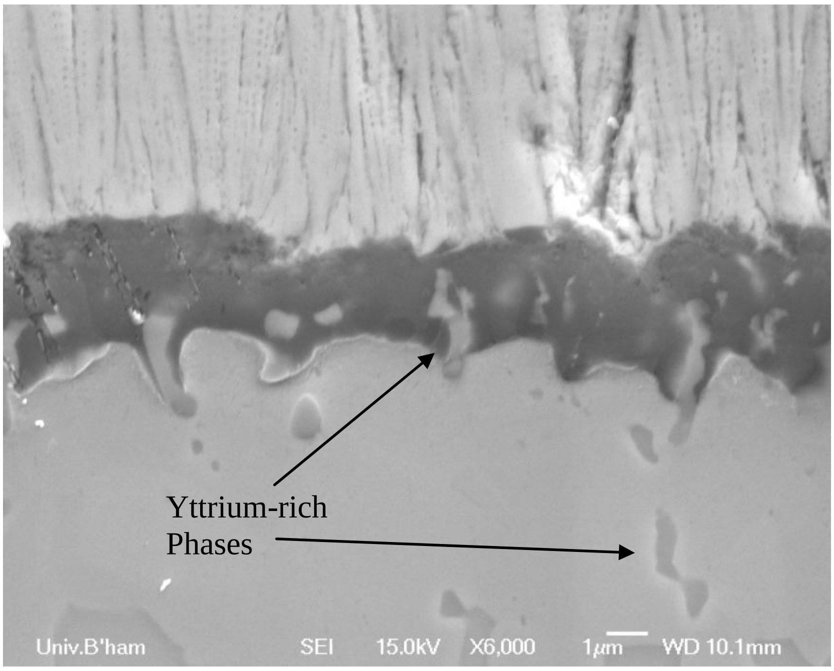

Figure 7.11: High magnification Scanning Electron Micrograph of the TGO region of the specimen held at 1050°C for 100 hours showing the presence of oxide pegs within the TGO.

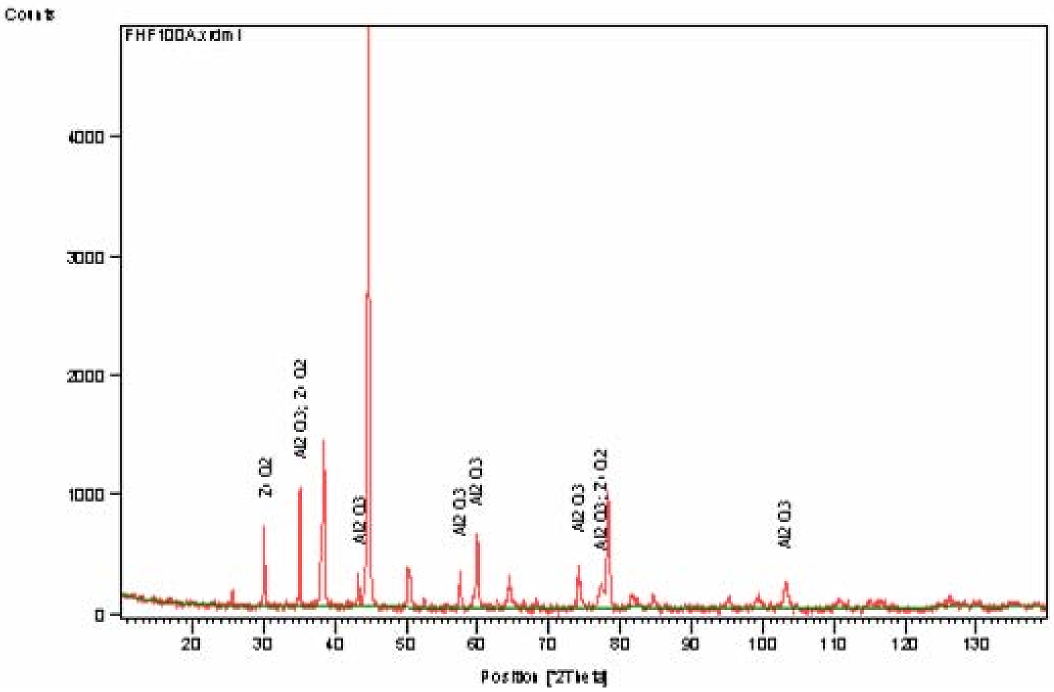

Figure 7.12: XRD spectrum of spalled ceramic topcoat with TGO attached from a specimen oxidised at 1150°C for 100h showing the principal peaks of α-alumina and zirconia. The remaining unidentified peaks can be attributed to minor peaks of α-alumina, zirconia and yttria.

XRD analysis of a spalled section of the TGO with attached YSZ, figure 7.12, shows that the TGO formed in these coatings is an α-alumina with no evidence of transitional alumina or other oxide peaks. EDS mapping of the TGO region, figure 7.13, showed that these pegs were yttrium-rich and were probably yttria alumina garnet (YAG). Other Y-rich phases were also found within the bond coat but without the associated oxygen signal found in the corresponding TGO phase, figure 7.11. This suggests that yttrium is diffusing in its elemental form through the bond coat to the oxidising surface where it reacts with the oxygen present to form YAG, (an yttrium, aluminium, oxygen compound). These oxide pegs have been seen in other studies and are believed to be due to an increase in the yttrium concentration in the EBPVD bond coats [145]. These oxides are known to be faster growing than the dense alumina and may have a detrimental effect on the adhesion of the TGO to the bond coat due to tensile stress generated between the alumina and the bond coat interface adjacent to the pegs. However, no evidence of a detrimental effect has been observed due to the presence of these pegs in this study.

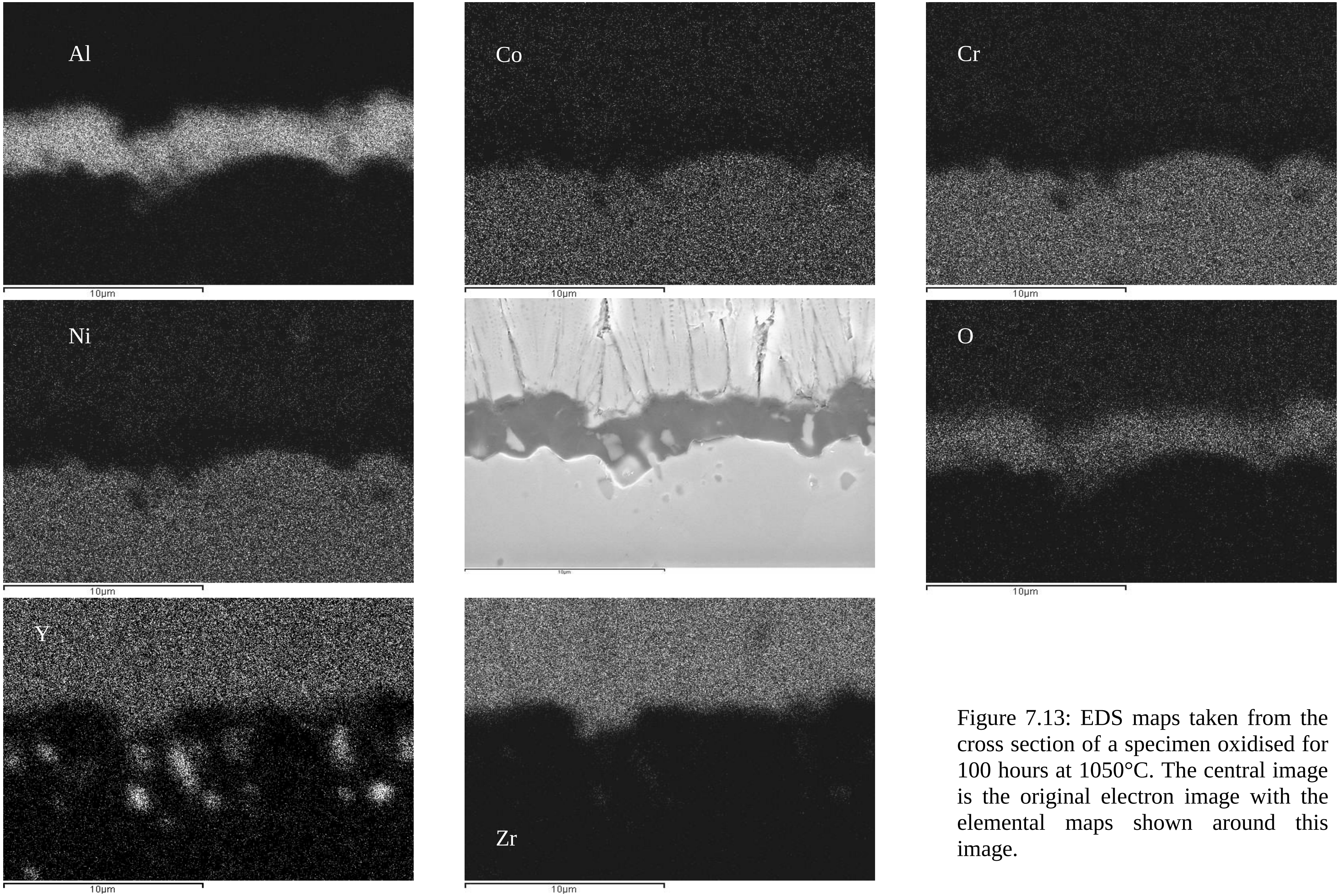

Figure 7.13: EDS maps taken from the cross section of a specimen oxidised for 100 hours at 1050°C. The central image is the original electron image with the elemental maps shown around this image.

7.6 Cracking and Failure

7.6.1 Sub-Critical Cracking

A significant observation, made in the sections of the specimen held at 1050°C for 100h, figure 7.10, and also in the as-received specimen, figures 7.14 was the presence of near-vertical cracks extending through the full thickness of the bond coat. The bond coat between these cracks was fully dense and intact. In the specimen examined in the as-received condition, no oxide was found within the cracks but in the specimen held at 1050°C for 100h, oxidation of the crack surfaces had occurred with an associated β (NiAl) phase depletion region in the adjacent bond coat. The oxidation of these features had not occurred in all cases. This suggests that some of these cracks are likely to intersect the outer bond coat surface allowing gas access and that others do not and are sealed. It is also worth noting that many of the cracks clearly extend the full thickness of the coating to the substrate but these cracks were not seen to extend into the IDZ or substrate. The effects of these features on the long term oxidation behaviour and on the delamination cracking within the TBC structure are not known.

It seems likely that this type of cracking is a result of the EBPVD coating process which produces a columnar structure. Post-coating densification is needed to close the interfaces between the columns which had not been fully achieved in these specimens. The numbers of specimens affected were few and possibly limited to one batch of specimens. Where it was believed that the features led to premature spallation of the topcoat repeat testing was performed. It was not possible to detect these cracks before testing and thus no further study of the effect they may have was carried out. The main result of these features is the observation that increased care is required in the manufacture of these coatings.

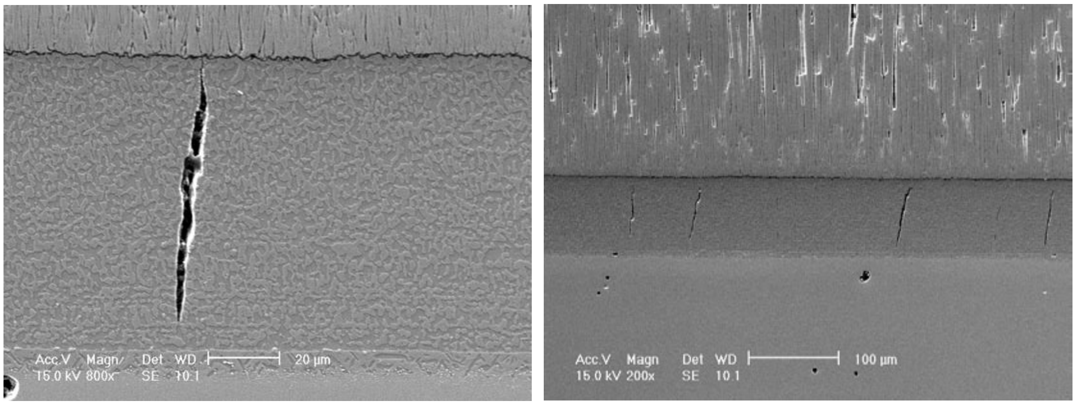

Figure 7.14 Scanning electron micrographs of a section through the as-received specimen showing the near-vertical cracks and their distribution throughout the bond coat.

7.6.2 Coating Failure

The criterion for failure in this coating system was set the same as for the TBC system with the HVOF bond coat, i.e. greater than or equal to 20% loss of the topcoat. It was observed that at all times when this criterion was met spallation occurred at the bond coat/TGO interface and on most occasions the topcoat and TGO spalled as a single piece. The spallation event occurred during the cooling stage of the test. The location of failure was at the bond coat/TGO interface and was consistent throughout; an example can be seen in figure 7.15 where it can be seen that total separation from the bond coat had not occurred. A low viscosity protective resin was used during preparation to maintain the integrity of the weakened structure to permit greater study. It should be noted that this specimen was not classified as having spalled and is listed in table 7.1 as delaminated as it is clear that the failure process is well advanced.

In addition it should be noted that despite examining a number of pre-failure specimens no evidence of sub-critical cracking was observed. This is consistent with the hypothesis made in section 6.6.1 that such sub critical short cracks require relatively large surface roughness to generate the out of plane stresses, this roughness is not present in these specimens.

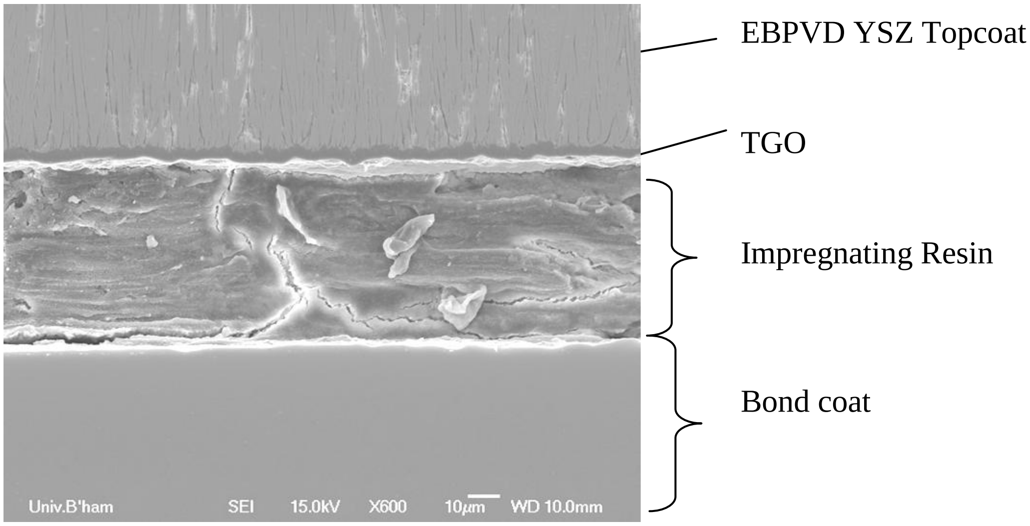

Figure 7.15 low magnifications SEM micrograph of a cross section through the TBC system with an EBPVD bond coat oxidised at 1150°C for 50hr, showing delamination at the TGO / bond coat interface.

This study indicates that crack development and propagation in these specimens occurs rapidly towards the end of life and during the final cooling transient. This is likely a result of the strain energy developed in the TGO during cooling due to the large mismatch in thermal expansion co-efficient between the substrate and TGO/topcoat. These strain energies within the TGO and topcoat can be calculated approximately using equation 6.4 at various temperature transitions, oxide thicknesses and thermal expansion co-efficient of the different layers. An example plot of the resultant strain energy generated at a fixed temperature drop of 1000K is given in figure 7.16. This gives the energy generated in the TGO and topcoat layers by the thermal expansion mismatch with the substrate. Here it is possible to see that greatest strain is developed within the topcoat. Whilst the substrate is not in direct contact with the TGO or topcoat it is still important to consider its affect as it makes up the majority of the specimens examined here. It would therefore exert a large influence over the total coating system. Failure of these coatings can be approximated to occur at an oxide thickness of 2.5µm as shown in table 7.1. It is clear to see here that the strain energies generated at an even smaller oxide thickness, however, are greater than the fracture energy required to cause cracking between the TGO and bond coat of approximately $0.66 Jm^{-2}$[62]. Therefore mechanisms for relaxation of this energy must occur to prevent failure of these coatings. It is likely that given, that the bond coat is capable of creep at high temperatures that this is the mechanism that allows for relaxation of the strain energy in the TGO. Also of importance here is the temperature drop which plays a significant role in the stress generation. At greater temperature drops the strain energy generated will increase whilst the capability of the bond coat to creep will fall. When the temperature reaches a critical level such that the stress generated after relaxation by the bond coat is greater than the energy required for crack propagation failure of the coating can occur through fast fracture, figure 7.17

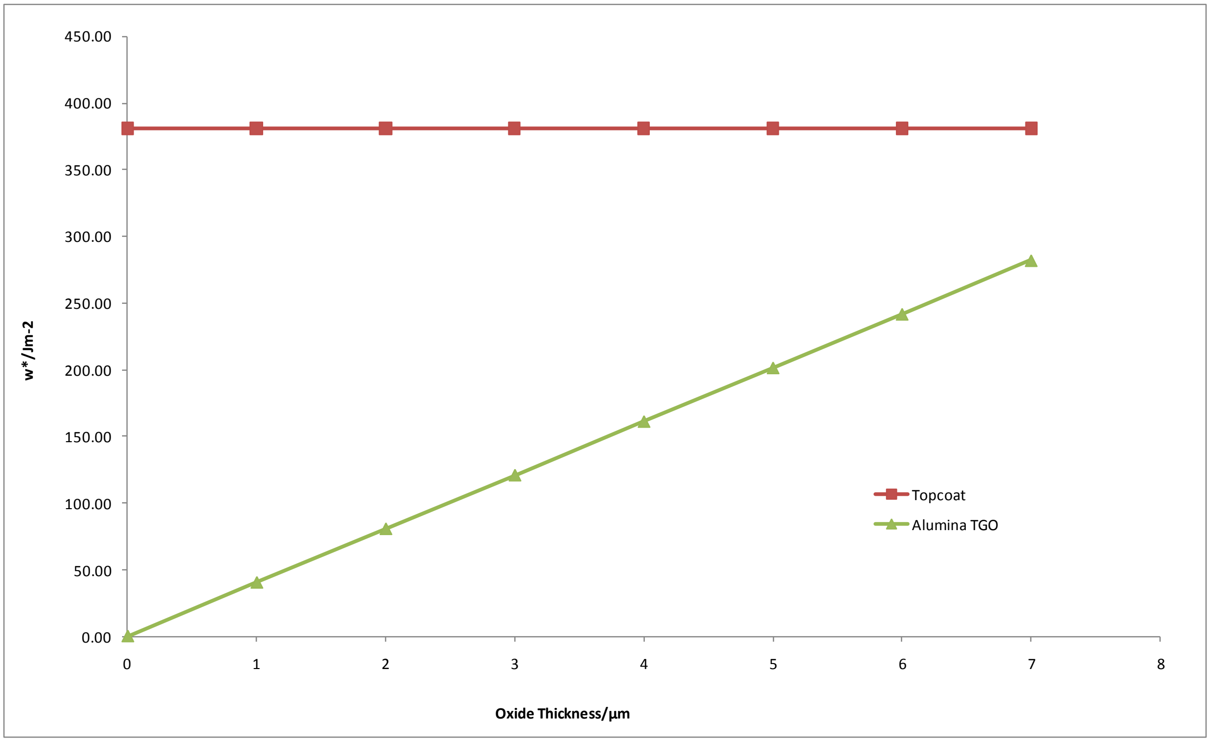

Figure 7.16: Strain energy formed in each of the TBC layers due to the thermal expansion miss match with the substrate after a temperature change of 1000K

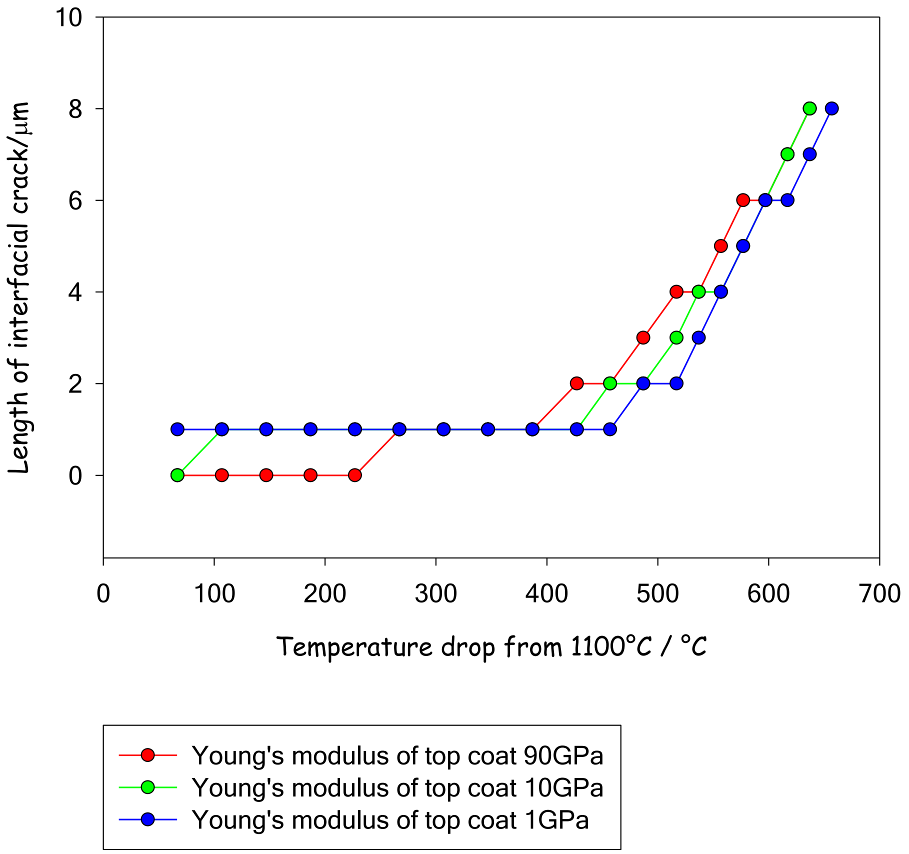

Figure 7.17: The kinetics of wedge crack growth during cooling a TBC system from 1100^{o}C at a constant rate of 40x10^{3} ^{o}C h^{-1}. The different curves correspond to different assumed values of the Young's modulus of the top coat[146].

The lifetimes of these specimens in the test conditions studied here are given in table 7.1 and, later in sections 8.7.8, figure 8.14, where a fuller discussion is given. Clearly the morphologies found in these two coating systems is similar and the results presented in sections 6 and 7 allow for further comparison and discussion of the coating systems. The next section, section 8, will seek to compare the two coating systems where possible but also draw conclusions as to the significance of these results.

8 DISCUSSION

8.1 Introduction

The previous sections have described the results obtained from the testing described in section 5 for both coatings. Whilst the two coatings studied here are somewhat different in terms of the method of application of the bond coat there are many factors which are identical between the two systems. The bond coats are from the same generic coating group, i.e. MCrAlY overlays and the compositions are very similar, table 8.1, the substrates are the same and produced in the same manner, table 5.1, the topcoats are also identical, yttria partially stabilised zirconia, and these are produced using EBPVD (section 5.1). A summary of the two systems is given in table 8.1. The experimental procedures were also held constant so that direct comparisons can be drawn between the two sets of data produced. The following chapter will explore the similarities and differences in the oxidation behaviour and failure mechanisms observed during this project and relate this to information from the literature.

Table 8.1: Bond coat Compositions for both coatings (wt%)

Application Method	Ni	Co	Cr	Al	Y
HVOF	36.2	33.5	21.0	9.0	0.3
EBPVD	52.8	19.2	17.8	10.2	0.1

8.2 Oxide Growth Distributions

An extensive investigation was performed on the distribution of the TGO thicknesses across the surface of the bond coat. Ten TGO thickness measurements were taken from each of ten micrographs, taken at regular intervals across the section from the whole specimen, to give a total of 100 measurements. Very few investigations to this level have been performed. This in-depth analysis has provided insight into the statistical distribution of the TGO thickness measurements for both coating systems.

During the course of this investigation care was taken such that the thickness of the TGO in the growing direction was recorded. In some cases this could be difficult due to the 3-D surface roughness of the bond coat. An increase in the surface roughness where the cross section is taken will tend to produce a thicker oxide measurement. This local surface roughness is a characteristic of the HVOF coating system and is necessary to improve the bonding between the bond coat and the topcoat. Although less severe in the case of EBPVD bond coats there remains some local surface roughness. In these coating systems the effect of surface roughness was minimised through careful sample preparation and measurement. The influence of surface roughness is discussed in terms of potential cracking at the interface in later sections 8.4 and 8.7.7.

The results as shown in sections 6.2 and 7.2 show that both coating systems followed a normal distribution of oxide thickness across the surface, with no evidence of rapid oxide growth or spinel formation, figures 6.1 and 7.1. Spinels are rapidly growing mixed oxides usually containing Ni, Cr and Co and their rapid growth is often a cause of failure in these types of coatings due to the stress developed in the topcoat by the upward localised growth of the oxide[105, 106]. Figure 8.1 shows an example of spinel growth on a bond coat surface from the literature; these features have not been observed in any of the specimens tested here.

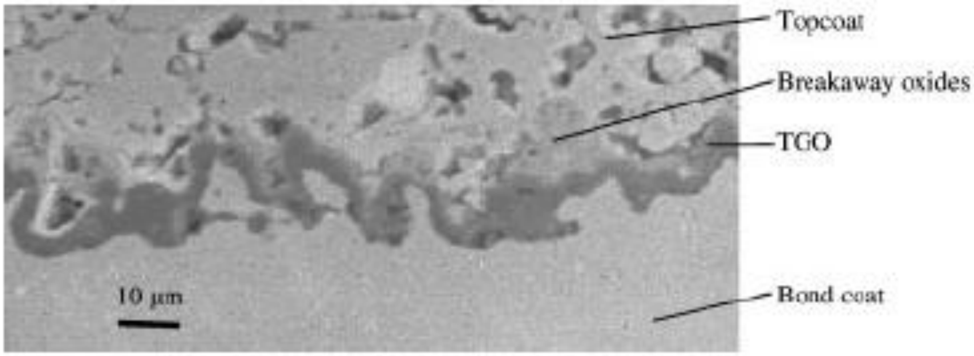

Figure 8.1: Example of a Spinel oxide formed on an electroplated NiCoCrAlY bond coat oxidised isothermally for 1000 hours at 1000°C. These oxides have not been observed in either coating studied here[106].

The lack of these features is likely to be a consequence of the relatively flat interface and few intersplat oxidation features which would restrict the diffusion of aluminium or lead to undercut oxidation, figure 8.2.

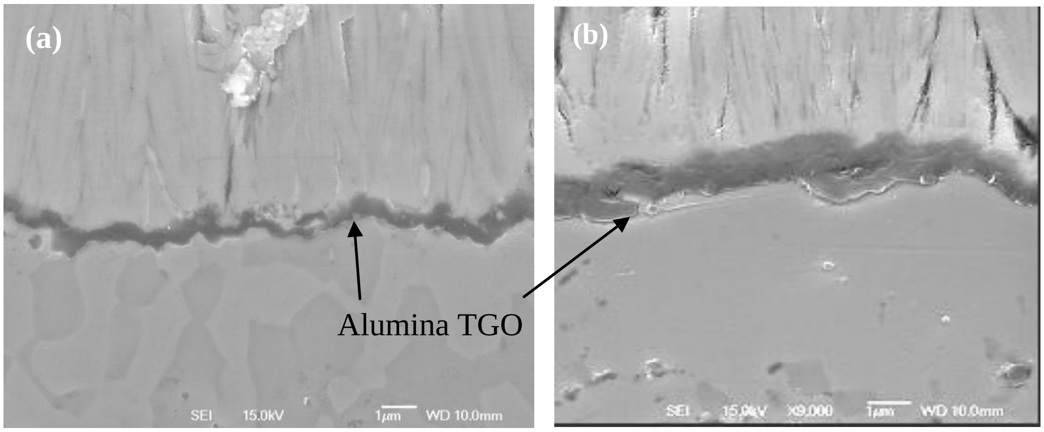

Figure 8.2: Scanning electron micrographs of the bond coat, TGO and topcoat of coatings with a) EBPVD applied bond coat and b) HVOF applied bond coat in the as received condition. Here the alumina TGO is visible in the as received condition.

Detailed analysis of the distribution of the oxide thicknesses shows an increase in standard deviation with increasing exposure time and temperature for both coatings. This can be seen in tables 6.1 and 7.1 which provide the oxide thicknesses and standard deviations for both coatings.

It is possible that this effect is caused by the geometric effect of cross sectioning of a rough bond coat. If the cross section falls across the flank of an asperity the oxide will appear thicker when measured at that location. However for this effect to be observed the surface roughness and thus distribution would need to increase with increasing time at temperature. In both of these coatings however the bond coat surface roughness is shown to not increase with time at temperature as shown in figure 8.3.

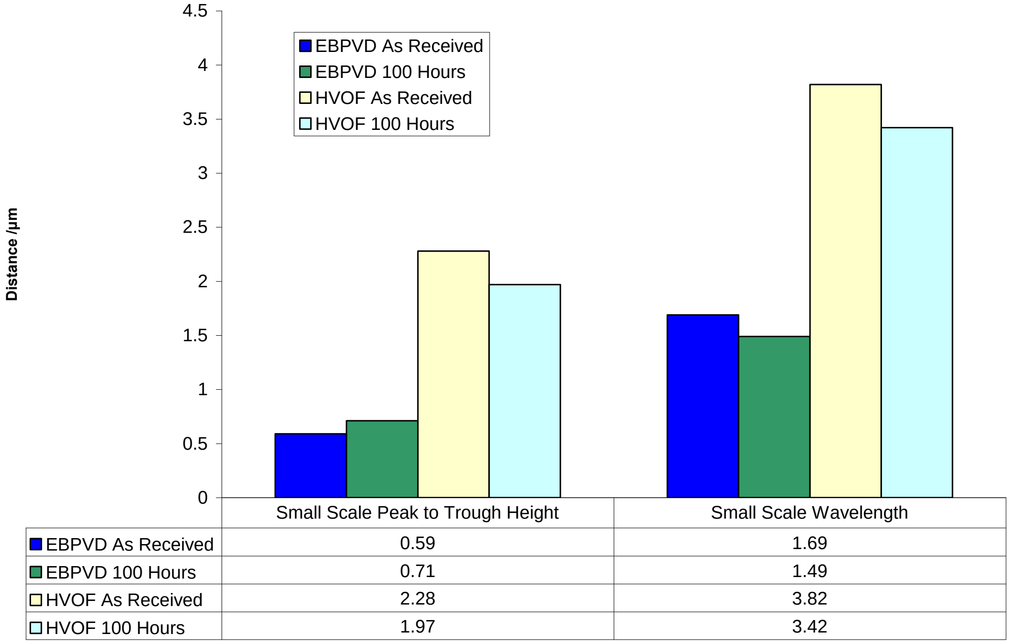

	Small Scale Peak to Trough Height	Small Scale Wavelength
🟦 EBPVD As Received	0.59	1.69
🟩 EBPVD 100 Hours	0.71	1.49
🟨 HVOF As Received	2.28	3.82
⬜ HVOF 100 Hours	1.97	3.42

Figure 8.3: Plot of peak to trough heights and wavelength measurements for both coatings in the as received condition and after 100 hours at 1050°C

It could also be possible that despite a dense alumina TGO being formed on both coatings as described in sections 6.5.2 and 7.5.2, that areas of the TGO grow with slightly different growth rates. It is then possible these localised areas of faster and slower growth rates continue to grow at their own localised rate and as such the standard deviation increase with increasing time at temperature. These localised growth rates could be caused by different localised concentrations of aluminium in the bond coat, with a localised decrease in aluminium leading to a slower growth rate in that area. However in the case of both coatings examined here this is unlikely to be the case as there is no evidence visually of phase differences within the bond coat adjacent to the TGO, this distribution of phases can be seen in the as received specimen for both coatings in figure 8.2

Another possible cause of the observation in both coatings of an increase in standard deviation in TGO thickness measurements is an uneven distribution of oxide grain size within the TGO. It is known that the rate of oxygen diffusion across the TGO is an important determinant in the growth rate of the TGO. Additionally, it is also known that for alumina oxides the rate of oxygen diffusion observed is greater than observed for pure lattice diffusion and so diffusion along oxide grain boundaries is likely to occur (section 2.2). This short circuit diffusion pathway is likely to be the dominant oxygen pathway and thus rate determining step for the growth of the TGO. Therefore any localised increase in size of oxide grains would lead to a localised decrease in oxide growth rate. It is likely that this mechanism plays a large part in the observations for both these coatings.

Measurements of the oxide grain size and distribution were attempted using electron backscattered detection (EBSD); however this technique requires an atomically smooth surface to be able to obtain good patterns. The process of polishing both coatings to a sufficiently smooth surface was complicated by the layered structure of these coatings, with layers of differing hardness and properties. Therefore it was not possible to obtain sufficiently good spectra from either coating using the mechanical polishing techniques available. However for future work it may be possible to use a newly installed focussed ion beam SEM (FIBSEM) to polish the coatings to a sufficient level. Unfortunately this equipment was not installed and available for this project but figure 8.4 of the EBPVD applied bond coat specimens shows that this technique could be used in future work.

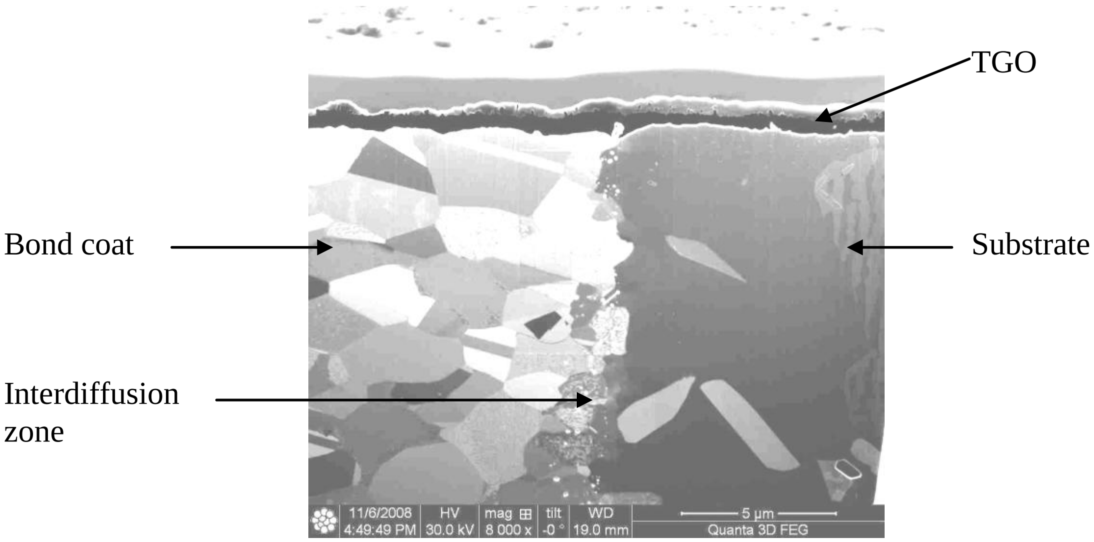

Figure 8.4: Cross section scanning electron micrograph of an EBPVD bond coat specimen observing the bond coat, interdiffusion zone and substrate, polished using a FIBSEM (image courtesy of Dr M P Taylor, University of Birmingham).

The range of TGO thicknesses obtained from each specimen, the lack of any evidence of other oxide formation from EDS analysis of sections through the specimens and some, all be it limited XRD, and the fact that the standard deviation increases with increasing time at temperature does show that there are a range of alumina growth rates for the alumina forming bond coats across the surface, table 8.2. These high and low K_p values have been calculated using the same procedure for the values given in section 6.3 and 7.3. The low K_p was calculated from oxide thickness taken at the 10 percentile from the normal distribution, whilst the high K_p values were taken as the 90 percentile.

Table 8.2: High and Low K_p Values for EBPVD and HVOF bond coats at 950°C

K_p at 950°C	**EBPVD Bond coat (m^2s^{-1})**	**HVOF Bond coat (m^2s^{-1})**
High	7.78×10^{-19}	1.33×10^{-18}
Mid	6.81×10^{-19}	9.33×10^{-19}
Low	4.21×10^{-19}	6.68×10^{-19}

Another possibility is that the growth rate of the alumina changes, all be it slightly, over the course of its life, i.e. one region may start off at the lower end of the alumina growth rate range but as the time increases the growth rate of that region may increase, or vice versa. Reasons for a decrease in the growth rate could be an increase in the average local grain size of the alumina, i.e. the width of the alumina grains. This would decrease the number of grain boundaries and thus a decrease in short circuit diffusion paths. An increase may be due to an increase in grain boundaries as would occur in regions of equiaxed grains. However such an effect is likely to even out the oxide growth across the surface and not show the increase in standard deviation seen in these coatings.

The likely cause therefore of the increase in observed oxide thickness standard deviation in both of these coatings is the differential growth rates of alumina across the surface. This is likely due to variations in the grain size distribution across the TGO, however the grain size could not be mapped for this project so this hypothesis could not be confirmed.

8.3 Oxidation Kinetics

After examination of the oxide growth distributions the kinetics of the oxide growth were calculated from the average thickness measurements. Both coatings observed sub-parabolic kinetics at all temperatures. However they demonstrated a wide variation in their time exponent (n) values with the HVOF bond coat showing cubic kinetics at all but the lowest temperature(table 8.3) and the EBPVD bond coat showing n values of around 2.5

Table 8.3: Values of the time exponent, n, and rate constant, k_n, calculated at each test temperature. (Note: temperatures of 1000°C and 1100°C were not tested for the EBPVD bond coat)

Temperature/ Coating	Time Exponant, n		Rate Constant k_n ($m^n s^{-1}$)	
	EBPVD Bondcoat	**HVOF Bondcoat**	**EBPVD Bondcoat**	**HVOF Bondcoat**
950°C	2.3	2.3	7.31×10^{-22}	1.68×10^{-20}
1000°C	NA	3.2	NA	6.93×10^{-25}
1050°C	2.5	3.3	1.36×10^{-20}	3.53×10^{-25}
1100°C	NA	3.0	NA	4.93×10^{-23}
1150°C	2.6	3.3	8.56×10^{-20}	1.47×10^{-24}

This apparent discrepancy of the n value at 950°C for the HVOF bond coat could be explained by erroneous points at the short test times. This is not unexpected as the oxide thickness at this time of 4 hours at temperature is very thin and approaching the limit of resolutions for the tests carried out here. Taking this into account it is reasonable to approximate the kinetics for the HVOF bond coat to be cubic. Using the data from table 8.3, it is possible to plot the oxide thicknesses against the oxidation time, figure 8.5. This demonstrates that at all but the lowest temperature tested here the EBPVD coating has the fastest growth rate.

It should be noted that while data for oxide thickness at 1150°C has been plotted to 100 hours for simplicity, this is an extrapolation from 25 hours. Failure of both coatings at 25 hours oxidation at this temperature means that the oxide growth kinetics were only calculated for data up to this point.

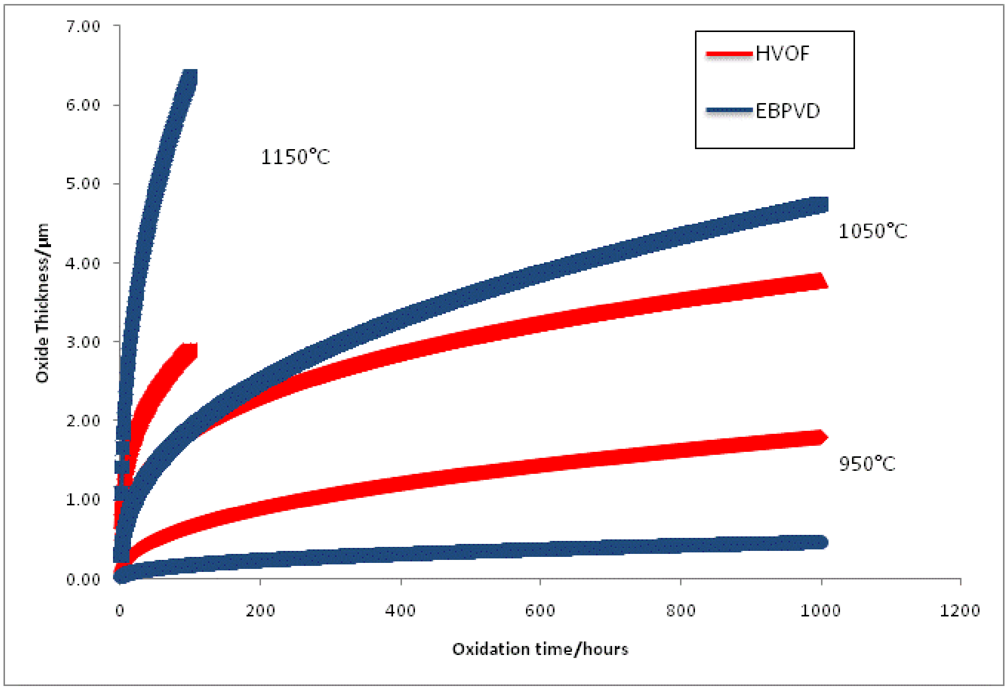

Figure 8.5: Plot of predicted oxide thickness at 3 temperatures within the tested range, obtained from data in table 8.3.

To aid the comparison with literature sources the pseudo parabolic kinetics were calculated at each test temperature using the method described by Hindam and Whittle[136]. Both coatings fitted well to literature results when using these pseudo-parabolic kinetics data indicating that for both coatings the oxide growth mechanism was typical to that seen in other related coating systems and an α alumina oxide is likely to have been formed. This is demonstrated when plotting this calculated kinetics against a mean line for alumina formers from Hindam and Whittles work (figure 8.6).

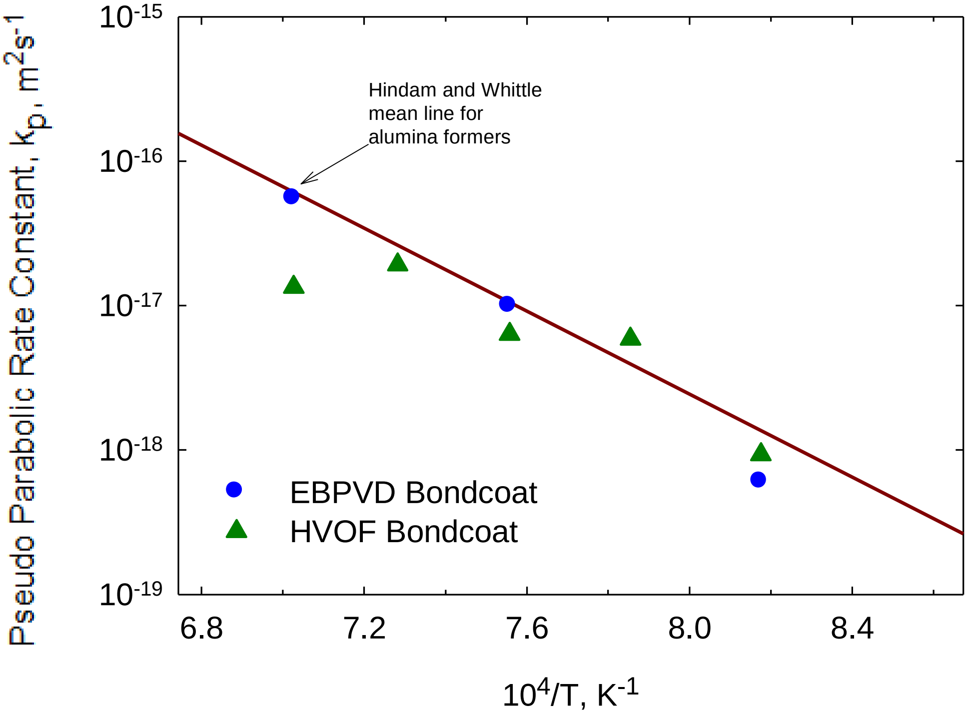

Figure 8.6: Plot of Pseudo-parabolic rate constants for both coatings compared to the predicted rates from work by Hindam and Whittle[136].

The sub parabolic kinetics observed here is typical of MCrAlY TBC systems and has been seen in a number or other studies[13-16]. There are a number of possible mechanisms for this type of growth kinetics. Firstly the transformation of transitional isoforms of alumina such as θ or γ to α-alumina has been described to form these sorts of kinetics[33, 35]. These transitional aluminas are known to have a higher growth rate than α-alumina and their gradual transition to α-alumina results in sub parabolic growth kinetics. However at the elevated temperatures used in this study α-alumina is the most stable isoform and as such any transitional aluminas would quickly transform. Additionally both of the coating systems examined here have a preformed α-alumina TGO from the application of the EBPVD topcoat. Therefore this mechanism is unlikely to be occurring in either coating type studied here.

A continuous increase in compressive growth stress within the oxide layer has been demonstrated to reduce the growth rate of an oxide, likewise a tensile stress will increase the oxide growth rate[27-30]. This effect has been described and modelled by Evans et al by considering the affect of the stress on vacancy transport. When comparing this model with data for the oxidation of for zirconia on zircaloy-2 a good agreement is observed[31]. This model however requires relatively thick oxides which are not seen in the present study[31].

The most likely cause of the observed kinetics for both of these coatings then is the increase in average oxide grain size. This occurs through the formation of larger oxide grains during continued oxidation because of preferred nucleation at the TGO/bond coat interface. This increase of average grain size at temperature will reduce the number of available grain boundaries at the TGO/bond coat interface for short circuit diffusion of oxygen to the TGO/bond coat interface. This effect will then reduce the growth rate of the oxide and lead to the sub parabolic kinetics observed here for both coatings.

8.4 Bond coat Surface Roughness

The surface roughness of the bond coat is thought to be an important factor in failures of some types of coatings, in particular an increase in surface roughness has been observed in some coatings with increasing time at temperature, section 4.9[120, 121, 123, 126-128, 137, 138, 147]. To examine this effect in the coating systems studied here two experiments were conducted as described in section 5.5. Briefly, cross sections of the as-received and the isothermally oxidised for 100 hours at 1050°C specimens were examined and measurements of wavelength and amplitude were taken. Additionally specimens were thermally cycled in 1 hour cycles at 1170°C to failure as described in section 5.3.3. These specimens had half the topcoat removed mechanically and were sectioned prior to testing. These specimens were then mounted in cross section and the roughness average (Ra) value was calculated at each area to British Standard BS1134, i.e. with and without the topcoat and before and after testing. This was carried out on both coating systems.

The calculation of the Ra value for each coating required the identification of a reference line from which a mean surface profile could be measured. This reference line for both coatings was taken to be the bond coat/substrate interface where precipitation of heavy elements from the substrate into the interdiffusion zone created a clear boundary (figure 5.6). In the case of the EBPVD bond coat this interface provided a good reference point in both specimens. However the HVOF applied bond coat is applied to a roughened substrate surface to provide mechanical keying. Therefore the interface contained considerable roughness in itself and made obtaining a reference line a challenging task. It was decided to use the peaks of the waviness at this interface as the reference line as a best approximation (figure 8.7). In terms of the Ra value calculated the most important requirement to this reference line is that it is parallel to the measured surface which this technique provided.

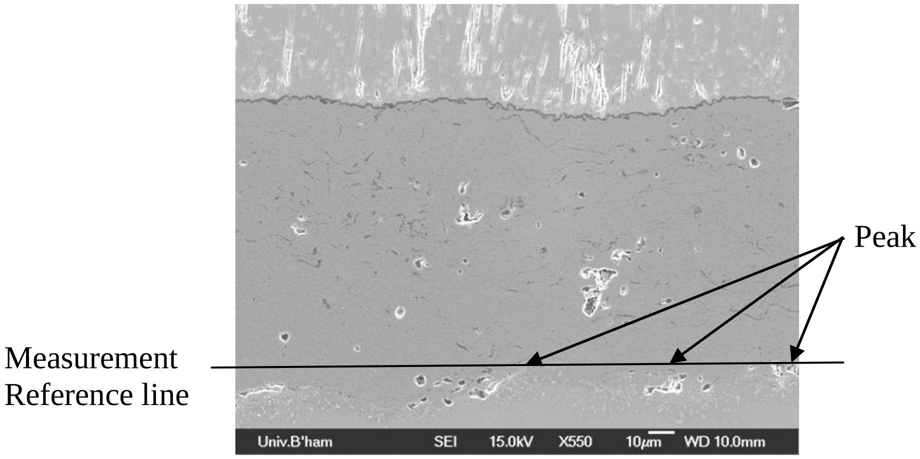

Figure 8.7: Scanning electron micrograph of an as received specimen of the HVOF applied bond coat for surface roughness measurement

An alternative and more accurate method of measuring the surface roughness would have been to use a Talysurf or atomic force microscope (AFM) to record the surface profile both before and after oxidation. However, this approach requires an exposed bond coat surface on which to perform the measurements and in the case of the specimens available for this project this was not possible due to the presence of the topcoat. Further the EBPVD process used to deposit the topcoat onto the bond coat modifies that surface, e.g. an alumina layer is grown on the bond coat. Any attempt to remove the topcoat and TGO either mechanically or chemically is likely to have altered the bond coat surface through relaxation of any constraints, therefore any results obtained would not be representative of the bond coat surface in a full coating system.

The results of this testing can be found in sections 6.4 and 7.4 for the HVOF and EBPVD bond coats respectively. The following two sections will look to draw comparisons between these results of both coating systems.

8.4.1 Wavelength and Amplitude Measurements

Whilst surface roughening has been seen in a number of overlay coatings without topcoats during oxidation, neither of the coating systems here showed an increase in surface roughness with time at temperature. It is likely that the topcoat provides mechanical constraint to the system and prevents any significant roughening of the surface. Additionally the strength of the bond coat is important to consider, for rumpling of the bond coat it must be compliant enough to creep at temperature. It is possible that the bond coats tested here had a creep strength at temperature that is too high for significant deformation and roughening.

A significant difference has been observed between the two coatings in that the HVOF coating exhibits a large scale surface roughness even in the as received specimen. This is not seen in EBPVD coating and may be important in terms of coating adherence and cracking. Additionally it can be noted from table 8.4 that the short scale roughness of the EBPVD coating is smaller in height and has a much shorter wavelength than the HVOF applied bond coat The difference can also be observed in figure 8.8 below in which the as-received oxide cross section of both coatings is shown. The rougher interface of the HVOF bond coat, as typical in thermal spray coatings, is evident.

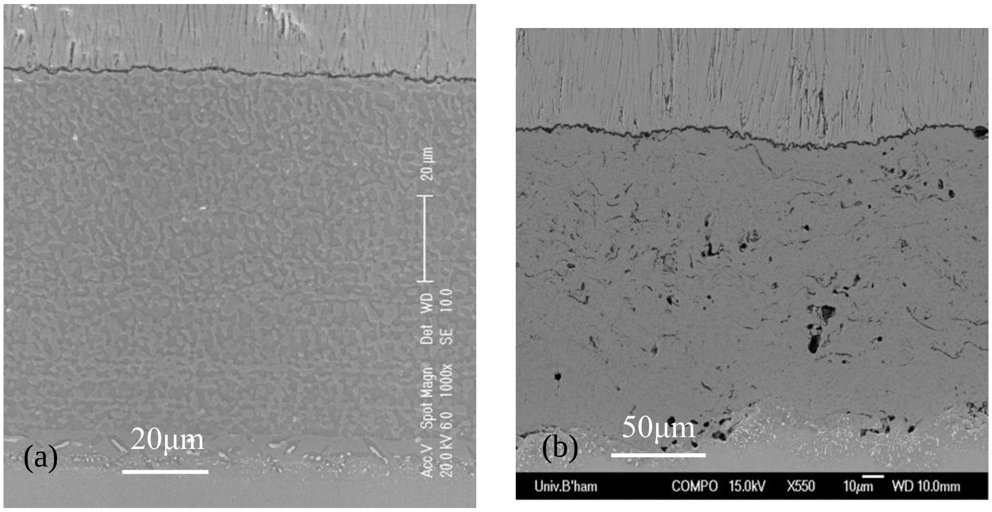

Figure 8.8: Two SEM micrographs of cross sections through the as-received specimen for both coatings showing (a) the EBPVD bond coat specimen with a relatively flat interface and , (b) the HVOF bond coat specimen showing a the two scales of roughness.

Table 8.4: Short scale wavelength and amplitude measurements for both coatings in the as received state and after isothermal oxidation.

		HVOF		**EBPVD**	
		As-received	100 hours at 1050°C	As-received	100 hours at 1050°C
Average small scale peak to trough height(µm)	6 Measurements	2.28	1.97	0.59	0.71
Average large scale peak to trough height(µm)	6 Measurements	16.12	18.15	NOT OBSERVED	
Average small scale wavelength (µm)	6 Measurements	3.82	3.42	1.69	1.49
Average large scale wavelength (µm)	6 Measurements	199.58	203.61	NOT OBSERVED	

This large scale roughness is a consequence of the different manufacturing route of the HVOF coating. In order to provide mechanical keying of the bond coat to the substrate the substrate is shot peened and the surface therefore deliberately roughened. This process does not take place for the EBPVD application method as a smoother substrate surface on application likely provides better columnar growth of the grains during the EBPVD process and a more even coating microstructure after final processing. Additionally it is likely that the adhesion between the substrate and the bond coat in the EBPVD system is greater than the HVOF system and therefore this mechanical keying is not required. The presence of a rougher interface in the HVOF applied bond coat may have a deleterious effect on the coating lifetime. Section 4.7 described how growth of the TGO could lead to the development of out of plane tensile stresses at temperature on the flanks of these asperities. These stresses could then lead to cracks forming in the topcoat and or TGO around these asperities and could ultimately lead to failure of the coating. Some examples of this type of cracking have been seen in the coating with a HVOF applied bond coat but did not lead to failure of the coating (section 6.6.1). These cracks were not seen in the smoother interface of the EBPVD applied coating.

8.4.2 Thermal Cycling

Numerous studies have shown that thermal cycling of diffusion coatings without topcoats can lead to a greater roughening of the coating surface, as stated in section 8.4.1. Therefore short 1hr cycles were carried out. It was important in gaining these results that a base line value of the surface roughness was obtained. However due to the presence of the topcoat the only way to obtain this for each specimen was to section the specimen prior to testing and examine the untested section as a reference. Additionally as noted in the previous section the effect of bond coat roughening has not been observed in the presence of a topcoat. To investigate the effect the topcoat may have on this mechanism it was decided to mechanically remove the topcoat from half of each sectioned specimen. The roughness of each section with and without a topcoat could then be compared. Whilst a reasonable match to the short scale roughness was achieved the large scale roughness of the HVOF applied bond coat was not. This is largely due to the difficulty of trying to match a roughness obtained from shot peening with that from mechanical grinding.

The results of this experiment show that for both coatings there was no significant difference in the surface roughness in any part of the specimen after thermal cycling to failure. As expected there is a difference between areas of the specimen with and without a topcoat due to difficulties in matching the coated surface roughness through mechanical polishing. This result is important as it suggests that the mechanical constraint applied by the topcoat in the systems tested here is not responsible for the lack of surface roughness observed. It therefore remains that there must be another contributing factor. This type of surface roughness has also not been observed from this type of coating with a thick substrate as seen here. It is therefore likely given this observation and the results seen here that the creep strength of the bond coats tested here prevents roughening of the bond coat.

Additionally it has been proposed[141] that one of the mechanisms that leads to this surface roughening is the transformation of phases in the bond coat adjacent to the TGO. In the case of the bond coats tested here only the γ phase was observed adjacent to the TGO even prior to oxidation. This is due to the depletion of aluminium to form the TGO during the application process of the topcoat. Therefore any phase change would not occur adjacent to the bond coat/TGO interface during subsequent oxidation. Any phase volume change associated with this phase change would be accommodated by the surrounding bond coat and would not lead to rumpling in these coatings.

8.5 Microstructure and Composition

Analysis of the compositional and microstructural development was carried out on both coatings using the techniques described in section 5. Emphasis was placed on analysing the bond coat and the TGO as these are the main differences and areas of interest between the two coatings. The microstructral development of the bond coat is an important consideration in many failure mechanisms such as chemical failure (8.7.2), rumpling (8.7.7) and phase transformations (8.7.3), therefore these results are important in characterising the behaviour of the coating systems.

This section will look to compare the main differences and similarities between two coating systems, looking firstly at the bond coat and moving on to the TGO. It will look to draw some conclusions as to the reasons and relevance of the observations reported in sections 6.5 and 7.5 for the HVOF and EBPVD applied bond coats respectively.

8.5.1 NiCoCrAlY Bond Coat

Whilst having slightly different compositions as shown in table 8.1, both coatings exhibited a similar dual phase β and γ structure, typical of NiCoCrAlY systems[148-152]. EDS analysis of the two phases was performed and the results are given in table 8.5, where data from slow and fast cooled experiments are presented alongside the results after normal air cooling.

Table 8.5: Compositions of the two phases present in the bond coat of both specimens after slow, fast and normal air cooling.

Concentration/ wt%	Gamma Phase					
	EBPVD Bond coat			HVOF Bond coat		
	Slow Cooled	Normal Cooling	Fast Cooled	Slow Cooled	Normal Cooling	Fast Cooled
Al	5.5	5.3	5.3	4.2	5.3	5.8
Ni	44.9	33.9	42.1	35.7	33.9	37.5
Co	25.9	36.3	25.9	36.0	36.3	33.9
Cr	26.9	26.0	26.9	24.3	24.2	22.6
Y	0.0	0.4	0.0	0.0	0.4	0.1

Concentration/ wt%	Beta Phase					
	EBPVD Bond coat			HVOF Bond coat		
	Slow Cooled	Normal Cooling	Fast Cooled	Slow Cooled	Normal Cooling	Fast Cooled
Al	19.5	19.2	17.4	17.9	18.7	17.5
Ni	58.7	52.8	56.2	50.4	50.4	50.3
Co	12.9	17.8	15.9	20.9	21.4	21.9
Cr	9.0	10.2	11.0	10.7	9.2	9.8
Y	0.0	0.1	0.0	0.1	0.3	0.6

This data shows that both coatings have similar phase compositions with any differences being within the measured standard deviation. A slight variation in the two coatings can be seen in the concentration of cobalt and nickel present, with the HVOF applied bond coat showing more cobalt and corresponding less nickel than the EBPVD applied bond coat. This fact appears however to have no effect upon the phases formed or the oxide formed as discussed in section 8.5.2.

These data are plotted in figure 8.10, on two Ni-Cr-Al phase diagrams at 1150°C and 1025°C, as discussed in sections 6 and 7 this is an approximation as no quaternary phase diagram taking into account the nickel and cobalt concentrations is available to match this system. The compositions of the beta and gamma phases follow boundaries of those phases as expected. Additionally from the phase diagrams the close proximity of the γ′-phase must be noted and therefore the possible presence of γ′ phases within the bond coats. However no evidence of these phases was observed in either coating system prior to or after oxidation. It can also be seen in figure 8.10 that the γ′ phase field shrinks with increasing temperature. Therefore it is possible that at the temperatures tested in this study the γ′ would not form at temperature but only briefly during cooling. Varied cooling rate experiments were carried out to examine this further, table 8.5, but this demonstrated that even with a relatively slow cool no γ′ was present. This is possibly due to the slow cool not being slow enough to form a fully room temperature equilibrium structure or that any nucleation of γ′ phase was too small to detect using SEM analyse and further analyse using TEM could be necessary.

In addition to the predominating γ and β phases present in both coatings some α-Cr isolated particles were observed in both coatings along the boundary with the interdiffusion zone, figure 8.9.

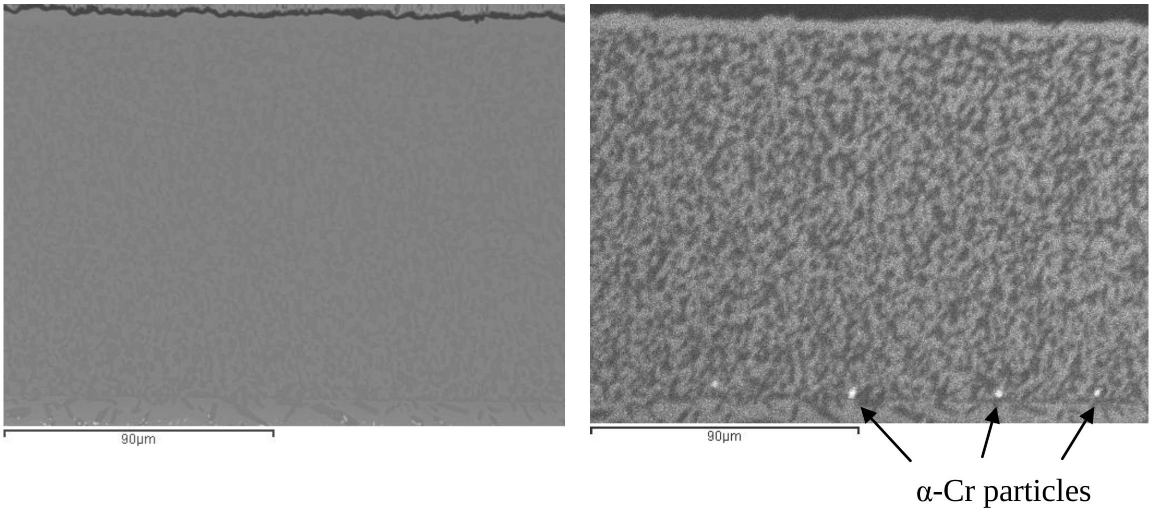

Figure 8.9: EBPVD applied bond coat oxidised for 25 hours at 1050°C. a) Scanning electron micrograph of bond coat, b) chromium EDS map showing α-Cr particles in bright contrast.

These particles are seen in the same area for both coatings and are likely formed in this region due to interdiffusion between the bond coat and substrate as this phase wasn't observed elsewhere in these coatings.

The structure of the outer region of the bond coat changed during exposure such that the β grains near the TGO convert to γ releasing aluminium for TGO formation. An increasing β depleted zone in this region developed in both coatings. This decrease in aluminium close to the TGO surface is typical of that formed under a growing oxide scale and can lead to failure of the coating if the level falls below that required for rehealing and continued growth of the oxide scale. This leads to the formation of often rapidly growing mixed oxides under the TGO, normally in isolated regions where diffusion of aluminium form the bond coat is restricted. Failure associated with this formation of none protective oxides is classed as chemical failure and was not observed in either of these coatings, section 8.7.2.

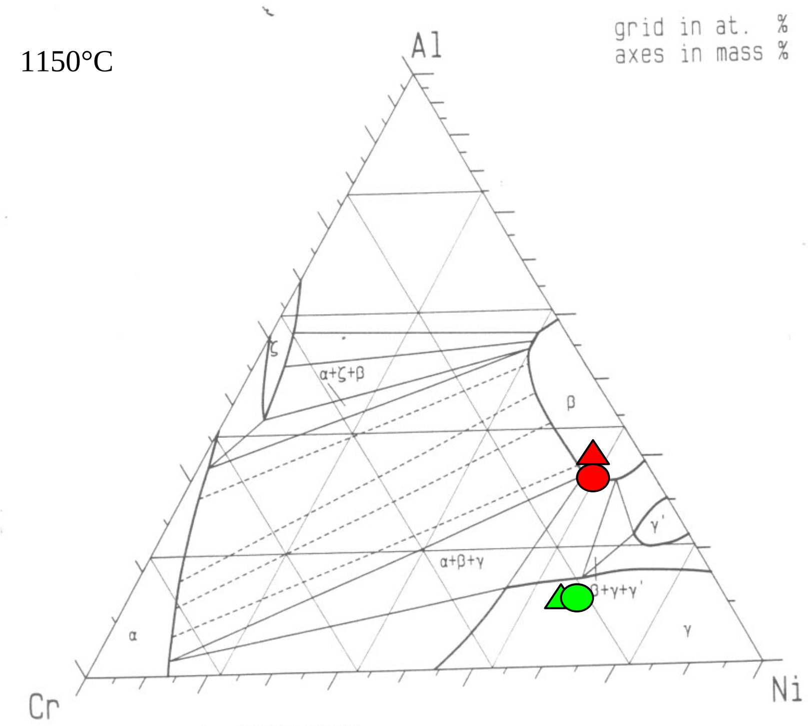

Figure 7: Partial isothermal section at 1150°C after [85Ofo]

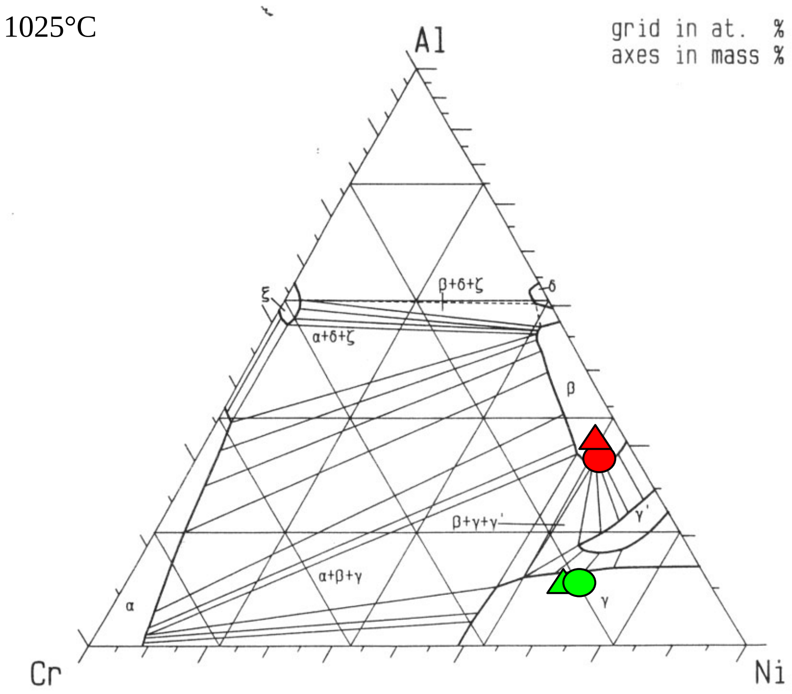

Figure 6: Partial isothermal section at 1025°C after [82Tu]

Figure 8.10: Ni-Cr-Al Phase diagrams at 1025°C and 1150°C showing the locations of the phases from both coating systems[153].

8.5.2 TGO Composition

Both coatings formed a stable dense α-alumina TGO at all times and temperatures as shown by the extensive statistical analysis performed, the kinetics of the two systems, EDS analysis and the XRD data, sections 6 and 7. The TBC system with the EBPVD bond coat exhibited substantial yttrium aluminium garnet (YAG) formation in the TGO coupled with enrichment of yttrium in precipitate phases in the bond coat near to the TGO possibly at grain boundaries in the bond coat. These yttrium phases were not seen with the HVOF bond coat, this may be a consequence of the coating production technique which tends to oxidise yttrium during the coating process. This effectively removes yttrium from the MCrAlY and forms yttria which is then trapped at the inter-splat boundaries. This does not occur during the EBPVD process, thus these bond coats are enriched with yttrium. This yttrium as described in section 2.5 is added to the bond coat to aid the adherence of the alumina TGO. The formation of these YAG pegs has been shown in section 2.5 to have both beneficial and deleterious effects on coating lifetime as the pegs are faster growing than the alumina scale but could provide mechanical keying for the scale. However, in this case neither of these effects are obvious as the failure time of both coatings are very similar, section 8.8, and therefore there appears to be no influence from the oxide pegs. It may be possible to prevent the formation of these yttrium rich particles and pegs for the EBPVD coating through reducing the yttrium content of the source ingot materials.

8.6 Cracking and Failure

During measurement of the TGO thickness examination of the entire bond coat/ TGO interface was carried out to look for signs of cracking and degradation of the coating. This was combined with the oxidation testing failures and observations were made to assess the mechanism of cracking and failure within both coating systems. The observations could be grouped into two categories, there were sub-critical cracks which did not lead to coating failure and, secondly, final coating delamination. The results of these observations can be found in section 6.6 and 7.6 for the two coatings systems. This section will compare the two coating systems and attempt to draw some conclusions from the observations made.

8.6.1 Sub-Critical Cracking

During observation of the HVOF applied coating after testing, short sometimes linked cracks were observed in the TGO/topcoat interface region. These cracks were often less than a few microns in length and normally associated with the flanks of asperities or surface roughness, figure 8.11.

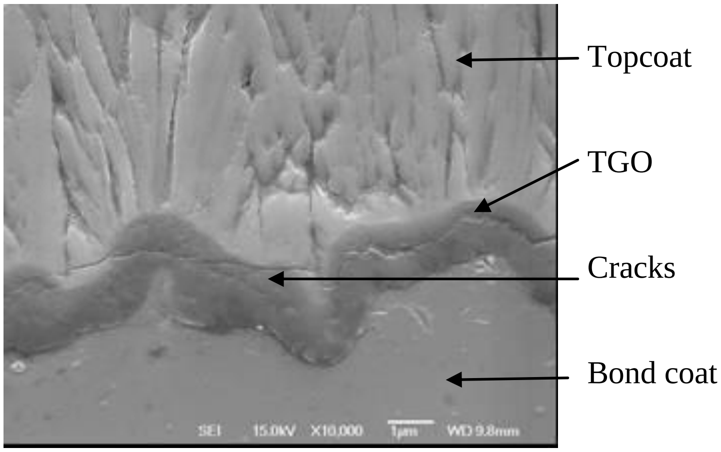

Figure 8.11: Scanning electron micrograph of a specimen with a HVOF bond coat oxidised for 2 hours at 1050°C showing short cracks at the interfacial region.

These cracks have been seen only in a few of the specimens but as all the specimens were prepared and examined in the same way so it is not believed that these features are produced during preparation. Also of note is that no such features have been observed in the EBPVD specimens. This is likely an indication and reflection that these crack are associated with the surface roughness of the bond coat. As was seen in section 8.4 the HVOF applied bond coat has a considerably rougher bond coat surface.

Cracks such as these have been demonstrated in the literature to be associated with the development of out of plane stresses on the flanks of the asperities where growth of the oxide is not perpendicular to the mean bond coat surface. The displacement of the topcoat however is perpendicular to the mean bond coat surface and as such exerts an out of plane stress across the TGO. Finite element analysis from the literature has shown that these stresses accumulate at temperature within the TGO and mainly the topcoat on the flanks of the asperities only for a short distance, figure 6.14. The short range of developed stresses means that there is no driving force to propagate these cracks for long distance through the coating and this explains the short nature of the cracks observed here and demonstrates why failure has not occurred associated with these cracks. Furthermore, figure 6.14 demonstrates that if the surface roughness is small, as is the case for the EBPVD coating, there is much less stress developed and therefore no cracks would be expected. This is what is seen with the EBPVD coating.

These cracks are only seen in some specimens oxidised at 1050°C with no sub critical cracks observed at the other test temperatures. It is possible that at the lower tested temperatures the rate of oxidation is too slow and thus the oxide is too thin to generate the required stresses to cause these cracks. Additionally it is possible that deformation of the bond coat through high temperature creep acts as a stress reliever and releases the stress before cracking occurs. A significant observation for both specimens is the lack of roughening, rumpling, of the bond coat during either isothermal or thermal cycle testing. This is an important consideration in this mechanism as rumpling of the bond coat will increase the size and distribution of the surface roughness where these cracks are observed. The lack of rumpling observed here would suggest that any cracking could only occur on pre existing roughness and this effect is unlikely to occur late in life due to a rougher bond coat.

8.6.2 Final Coating Failure

Both coatings demonstrated identical final failures with total removal of the topcoat and TGO at the TGO/bond coat interface upon cooling. For both coatings failure typically occurred across the entire surface at once, a short time after removal from the furnace. This indicates that the mechanism of failure is similar in both coatings and is likely related to the strain energy generated upon cooling due to thermal expansion mismatch between the TGO and substrate. It is possible to calculate the expected strain energy generated in the TGO and topcoat for these coatings and as each is similar in composition and make up the generated energies would be expected to be similar. Equation 6.2 gives the equation for calculating the strain energy and plotting these energies, figure 8.12, for the topcoat, TGO and combined system. This shows that large strain energies are generated predominantly in the topcoat. This plot was calculated using the parameters in table 8.6.

Table 8.6: Parameters used for calculation of strain energy in the TGO and topcoat of a TBC system.

Parameter/ Coating layer	**Alumina TGO**	**EBPVD YSZ topcoat**	**CMSX-4 Substrate**
Young's Modulus, E, GPa	367	60	NA
Poisson's Ratio, υ	0.25	0.1	NA
Thermal Expansion Co-efficient, K^{-1}	$7.9x10^{-6}$	$1.03x10^{-5}$	$2.0x10^{-5}$

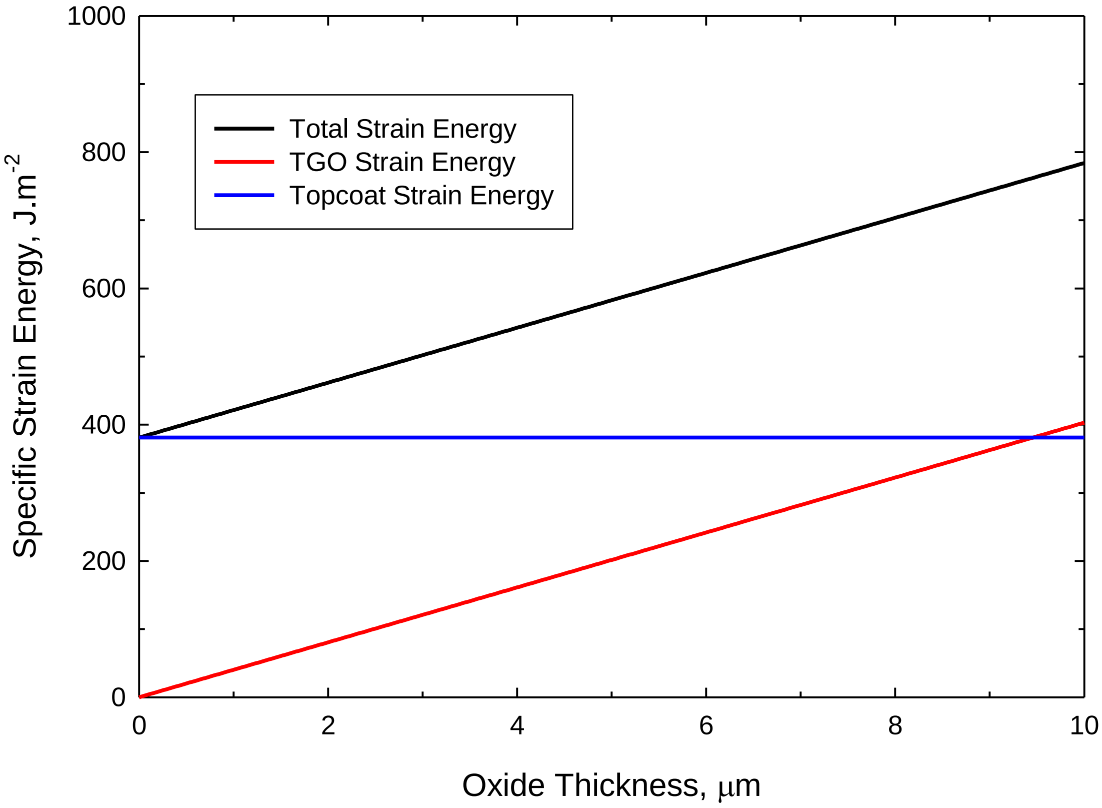

Figure 8.12: Plot of the specific strain energy generated in the TGO and topcoat due to thermal expansion co efficient miss match between these layers and the substrate against oxide thickness for a temperature drop of 1000K

This level of energy is clearly above the fracture energy required to cause decohesion of the alumina at the bond coat/TGO interface which, first-principle calculations[62] indicate, is around 0.66 J.m^{-2}. Therefore as described in section 6.6 the energy generated in the TGO is most likely being absorbed by creep of the bond coat.

8.7 Failure Mechanisms and Coating Lifetimes

Final spallation in both TBC systems occurred by the same mechanism at the bond coat/TGO interface. The driving force for this was the thermal expansion mismatch between the very different material layers. Section 4 of this thesis described some major failure mechanisms associated with thermal barrier coating systems. This section will explore these failure mechanisms in relation to the results and observations for this project.

8.7.1 Wedge Cracking

This failure mechanism occurs at the bond coat/TGO interface by the growth of a wedge crack driven by shear stresses along fracture surfaces in the TGO. The driving force for this failure mechanism is the energy from thermal expansion mismatch between the TGO and substrate. This generates a compressive stress within the oxide as the substrate contracts more than the TGO during cooling. It is this compressive stress coupled with strong TGO/bond coat adhesion which leads to the formation of shear cracks within the TGO and small area of decohesion between the TGO and bond coat. The deflection of the TGO leads to the development of stresses at or near the crack tip. Some of this stress is released by creep of the bond coat. However as the temperature decreases the ability of the bond coat to creep decreases and the compressive stresses on the TGO increase. This leads to greater tensile stresses at the crack tip until a sufficient temperature drop is reached for propagation of the crack. However a requirement for the generation of the wedge crack is the formation of shear cracks within the TGO but no clear evidence for such cracks was found in this work. The vertical displacement of the TGO required to form this shear cracks is very small in the range of a few nanometres. It is therefore possible that these cracks were present but not observed prior to failure by rapid propagation of the areas of decohesion. It is likely that this is the final failure mechanism observed for both of these coatings however the lack of through thickness cracks within the TGO make it difficult to confirm this.

8.7.2 Chemical Failure

Chemical Failure is the breakdown of the bond coat through oxidation and the formation of rapidly growing oxides, typically of Ni and Co. These sorts of failures occur because of excessive depletion of the selectively oxidised alloying element, in this case aluminium. Typically these failures will occur where an anomaly will prevent the transport of aluminium through the bond coat to the oxide/bond coat interface. These anomalies could be oxide splats, usually found in plasma sprayed coatings, creases and folds in the bond coat surface where undercut oxidation has prevented aluminium diffusion and in surface protuberances. This type of failure can also occur very late in life where the aluminium concentration of the bond coat has fallen below the level required to maintain an alumina protective oxide. Examination of these specimens under an SEM has shown no evidence of any of the features required for this type of failure. Although some oxide splats have been observed in the HVOF applied coating they are small in number and widely dispersed so do not prevent aluminium diffusion. Additionally statistical analysis of the TGO thickness has shown no evidence for rapidly growing oxides. Therefore this mechanism is not occurring in either coating examined here.

8.7.3 Bond coat Phase Transformations

The transformation of phases in the bond coat adjacent to the TGO could cause displacement of the TGO through a volume expansion or contraction associated with the phase change. This can be particularly noticeable in the conversation of β to γ or γ′ phase in the bond coat. Some calculations have shown that a volume contraction due to this conversion could cause stresses across the TGO. However observations of β to γ′ phase changes in the bond coat adjacent to the TGO interface has shown no deflection, figure 8.13. Another additional phase transformation which could be important is the formation of β-martensite. However the presence of an area depleted of β- phase adjacent to the TGO already present in the as received specimen would negate any impact of phase changes on these coatings. No evidence of phase changes adjacent to the TGO has been seen in either of these coatings and so this mechanism is unlikely to have any affect here.

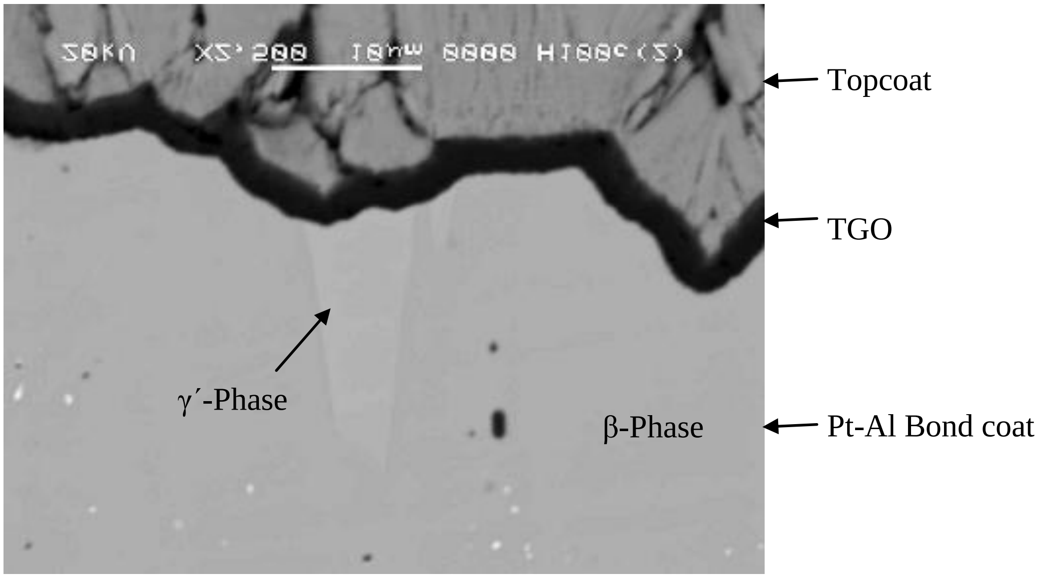

Figure 8.13: Scanning electron micrograph of a platinum aluminide bond coat oxidised for 100 hours at 1100°C showing phase transformation from β to γ′ phase and no deflection of the TGO.[154]

8.7.4 Non-uniform oxide growth

The growth of transitional aluminas with a high growth rate can have a deleterious effect on the lifetime of the coating. These transitional aluminas are meta-stable at the high temperatures used in this study and will therefore tend to convert to α- alumina. This conversion leads to a volume decrease and can therefore lead to increased stress in the TGO. This generates tensile stresses across the TGO and leads to crack nucleation and growth at the topcoat/TGO interface. XRD analysis of the TGO formed from both of these coatings has shown no evidence of transitional aluminas, additionally the statistical analysis performed on the TGO thickness shows the oxide formed is consistent with solely α-alumina formation. This is likely due to the heat treatment performed for application of the topcoat forming a fully dense α-alumina oxide. Furthermore extensive cracking on these coatings leading to final failure has not been observed at the TGO/topcoat interface, therefore this mechanism is unlikely to affect these coatings.

8.7.5 Growth of Oxide on non-planar Surfaces

The growth of alumina on a roughened surface can lead to considerable localised out of plane stress development of the flanks of any asperities. While localised this mechanism can form small cracks in the TGO/topcoat interface, which can link together to lead to further degradation of the coating. The EBPVD bond coat studied here has a relatively flat bond coat surface and thus does not have the necessary roughness to form these sorts of cracks. This is consistent with the observation that no cracks have been seen in the EBPVD coating in this area. However the HVOF bond coat has a much rougher surface and therefore could form these sorts of cracks. At some short times at 1050°C cracks of this sort have been observed in this coating. However these cracks are short as there is insufficient driving force to propagate the cracks through the coating. Also few of the cracks have linked together probably because the surface roughness is not great enough for the cracks to be close enough together to link. Whilst it is clear that this mechanism is occurring only in the HVOF coating, the roughness of the coating and the subsequent size of the cracks is not sufficient to lead to coating failure.

8.7.6 Ratcheting

As discussed earlier in this section considerable stresses are developed in the TGO upon cooling due to the thermal expansion mismatch with the substrate. On a planar surface these stresses are purely biaxial in nature, however TBC coatings are often quite undulating in nature as demonstrated in these coatings in there surface roughness[116]. These undulations lead to shear stresses on the flanks of the asperities during cooling after growth of the TGO[116, 117]. If these stresses are greater than the yield strength of the alloy the undulation will increase in size due to plastic deformation of the bond coat[116, 117]. This process relies on thermal cycles with incremental increase in roughness with increasing cycles[116, 117]. This increased roughness can lead to decohesion at the base or peaks of the asperities and cause failure through buckling[117]. This failure mechanism relies on the growth of the oxide and thermal cycles[117]. Measurement of bond coat surface roughness of both coatings tested here shows that there is no significant increase due to thermal cycling or isothermal testing. Therefore this mechanism is not occurring in either of the coatings tested here.

8.7.7 Rumpling

Roughening of the bond coat surface has been shown to occur in systems without a topcoat and leads to cracking of the oxide layer. Currently no evidence has been observed for rumpling of bond coats with the topcoat in place as is the case with both the coatings tested here. Measurement of the surface roughness before and after oxidation for the isothermal tests showed no increase in surface roughness or any evidence of rumpling occurring. Additionally 1-hour thermal cycle tests carried out with and without a topcoat in place on both coatings types showed no significant increase in surface roughness. Therefore, this would mean that rumpling of the bond coat surface is not occurring in either coating tested here. This could be due to the bond coats being too strong in creep to allow sufficient deformation and movement of the TGO.

8.7.8 Coating Lifetime

There is considerable literature available on the failure times for TBC systems containing both MCrAlY and Pt-aluminide bond coats. Figure 8.14 gives some of these results obtained from specimens coated with standard, non-experimental TBC systems. The coatings presented in figure 8.14 include a range of MCrAlY overlay coatings of different compositions and also NiAlPt diffusion type bond coats. In all cases failure has been determined by the spallation of at least 20% of the topcoat using the same criteria as used in this thesis. They include tests which were exposed to both isothermal and thermal cycling conditions but no systematic effect of test condition could be found. Similarly, there appeared to be no great difference between systems with a MCrAlY or Pt-aluminide bond coat. It is clear however from figure 8.14 that there is considerable scatter in the observed failure lifetimes, often varying by 10 times. This large scatter is likely a consequence of variation in the coating manufacture. Even when the same equipment and parameters are used some variation in handling can occur between coating batches. These variations invariably lead to variations in surface roughness or inclusion on the coating surface or layers. It is likely that the variation in surface roughness affects the scatter of failure times observed here, as this is a major cause of stress generation in coatings. Also plotted in this graph are the failure times for both coating systems studied here, noting however that only the EBPVD coating showed a failure at 950°C. This shows that the spallation times found in this present work agree well with the literature values reported elsewhere for similar coatings and the present coatings tested offer neither an advantage nor disadvantage in terms of coating lifetime.

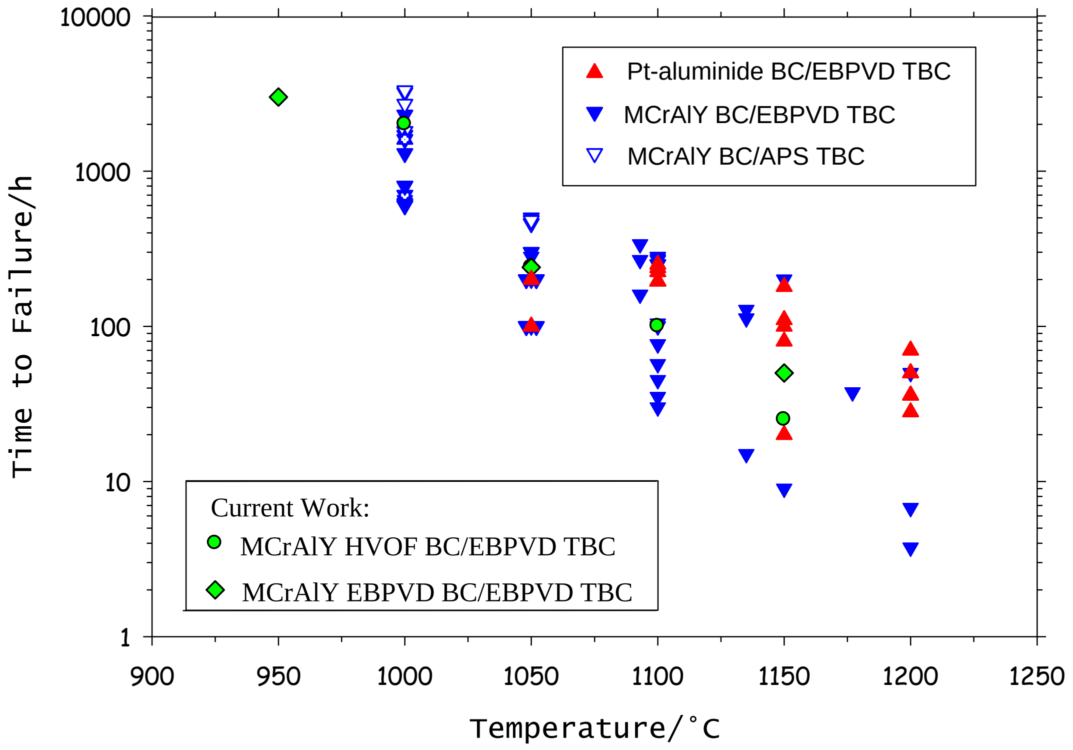

Figure 8.14: The failure times of both coating 1(HVOF) and coating 2(EBPVD)in comparison with literature data on failure times of similar coatings[100, 155-163].

9 CONCLUSIONS AND FUTURE WORK

9.1 Conclusions

- An in depth and extensive study has been carried out into the oxidation behaviour of two thermal barrier coating systems consisting of a CMSX-4 substrate, MCrAlY bond coat and EBPVD applied yttria stabilised zirconia (YSZ) topcoat. One bond coat was applied by high velocity oxy-fuel (HVOF) spraying and the other of similar composition was applied by electron beam physical vapour deposition (EBPVD).

- Oxidation kinetics
    - An examination of the oxidation kinetics through detailed analysis of oxide thicknesses was performed after isothermal testing in air on both coating systems at three test temperatures of 950°C, 1050°C, and 1150°C. Additional testing at 1000°C and 1100°C was carried out on the HVOF applied coating only due to limitations in the availability of specimens.
    - The kinetic data produced showed that the oxide thickness varied across the surface with a Gaussian distribution found for both coating systems.
    - Further analysis showed that an increase in the standard deviation of these coating thicknesses was observed with increasing time at temperature for both coatings and this was likely due to varying localised alumina growth rates across the coating surface.

    - The growth rates for both coatings were found to be sub parabolic at all the tested temperatures with n values ranging from 2.3-3.3. This was likely due to an increase in the average oxide grain size with increasing time at temperature but could not be confirmed in the present study.
    - For comparison to literature kinetics, pseudo parabolic kinetics were calculated for both coatings. These kinetics were found to fit well to the mean line for alumina formers derived by Hindam and Whittle[136].

- Bond coat surface roughness.
    - The surface roughness of the isothermally oxidised specimens for both coatings were determined from amplitude and wavelength measurements taken from specimen cross sections. The HVOF applied bond coat system was found to have a short and long scale roughness, characteristic of this coating type. The EBPVD applied bond coat system showed a much smoother interface with only short scale roughness present.
    - The surface roughness did not increase in either coating under isothermal oxidation exposures.
    - The surface roughness was measured for both coating systems with and without a topcoat under cyclic oxidation of 1 hour cycles at 1170°C. Again, no increase in surface roughness with increasing cycles was observed in either coating. No evidence of bond coat rumpling was found.

- Microstructure and compositions
  - The compositions of the bond coats of each coating were measured using EDS. Both coatings formed a dual phase β-NiAl and γ-Ni structure throughout the bond coat with heavy elements from the substrate precipitating in the interdiffusion zone. Some α-Cr particles were found in both coatings along the bond coat interdiffusion zone interface.
  - Depletion of aluminium adjacent to the bond coat surface to form the thermally grown oxide (TGO) led to the formation of a β depleted zone adjacent to the TGO. This increased in size with increasing time at temperature for both coatings.
  - A TGO was present between the bond coat and topcoat in all specimens including the as coated, untested specimens. This was found, through XRD analysis of oxidised specimens, to be α-alumina. The oxide thickness distributions were uni-modal, indicating that no breakaway-type oxides had formed and that α-alumina was the predominant oxide phase at all tested times and temperatures for both coating systems. This was consistent with the SEM observations.
  - Yttrium rich phases were observed in the TGO of the EBPVD applied bond coat only with further yttrium rich phases within the bond coat close to the TGO/bond coat interface. These phases were likely to be yttrium aluminium garnet (YAG) pegs. They were not observed in the HVOF applied bond coat appear to have no influence on coating failure in these coatings.

- Cracking and failure
    - Sub critical cracks of a few microns in length were observed in the vicinity of the TGO/topcoat interface after short times at 1050°C for the HVOF applied coating.
    - These cracks were found predominantly on the flanks of the asperities in the bond coat surface roughness.
    - Whilst some of these cracks were found to link together, they were not of considerable length and appeared not to grow with increasing time at temperature.
    - These cracks are formed by the generation of out of plane tensile stresses on the flanks of the asperities at temperature. These stresses are typically shown through finite element modelling, performed elsewhere, to be localised in these areas and so there is no driving force to propagate the cracks further. As such these cracks are not, in the case of the coating tested here, associated with final coating failure.
    - These cracks are not observed in the EBPVD applied bond coat, this is due to the bond coat surface having a low roughness.
    - Final coating failure in both coating systems occurred at the bond coat/TGO interface through rapid propagation of cracks–along the interface. This rapid propagation is likely driven by the large strain energies generated in the TGO through thermal expansion mismatch between the TGO and substrate layer.
    - The mechanism of generation of the initial decohesion at this interface is unknown but could be due to the formation of wedge cracks. However failure typically occurred through complete spallation of the topcoat and TGO therefore no

    evidence of wedge crack formation was observed so this mechanism cannot be confirmed.

    - Comparison of the time to failure for both coating systems with published literature values for a range of coatings shows a good fit. However there is a large scatter within these observed failure times even for similar coatings. This is likely due to variation in manufacture of these coatings, specifically related to the bond coat surface roughness.

9.2 Future Work

- Confirmation of the measured oxidation kinetics could further demonstrate the sub parabolic growth of the TGO in these coating systems. This could be carried out through thermo gravimetric analysis of the mass gain of the coatings. Some experiments were conducted with the present set of specimens but a failure to mask the substrate alloy on the exposed surface made the results unusable. The use of fully coated specimens would alleviate this problem and allow this type of testing.
- The characterisation of the microstructure of the TGO formed on these coatings could be used to confirm its effect on TGO growth kinetics. This could be achieved through use of Focussed Ion Beam Scanning Electron Microscopy (FIBSEM) to polish specimen cross sections for examination using Electron Backscatter Diffraction (EBSD). Trials on this technique for these coatings have shown promising results for the FIBSEM polishing, figure 8.4.

10 APPENDIX 1

10.1 Thermal-Gravimetric Analysis (TGA)

TGA experiments were attempted using the apparatus available, figure 11.1, in an attempt to obtain oxidation kinetics based on weight gain. The intension was to compare these data with the kinetics obtained from the TGO thickness measurements and obtain early stage oxidation data.

Figure 11.1: TGA measurement equipment.

However, this procedure was complicated by the exposed superalloy on the base surface of the specimens. In addition, the total weight of each specimen exceeded the maximum weight capability of the apparatus. Therefore, each test specimen had to be first manually thinned by using wet and dry SiC paper to remove part of the superalloy substrate from the uncoated surface of the specimen and reduce the total specimen weight to 3mg. Oxidation of the exposed superalloy was still an issue and three techniques to limit its extent were investigated. Firstly, an alumina paste supplied by Pi-Kem, was applied to the uncoated superalloy. However, it was found that the alumina paste did not sufficiently bond to the alloy and thus easily spalled away during the early part of the test, proving ineffective. Secondly, a platinum sputtered coating was applied to the uncoated superalloy. Despite reducing the substrate oxidation this again produced no useable results as it did not prevent oxidation of the substrate. Thirdly, a CMSX-4 coupon, uncoated on all surfaces, was used. It was postulated that the TGA data this provided could be standardised for surface area and then be used to subtract from the specimen mass gain data of the coated specimens to obtain the mass gain for the coated section only. However, the high rate and variability of the oxidation of the substrate made the errors involved in this procedure too great to obtain meaningful results.

11 REFERENCES

1. Goward, G.W., *Progress in coatings for gas turbine airfoils.* Surface and Coatings Technology, 1998. **108-109**(1-3): p. 73-79.
2. Miller, R., *Current status of thermal barrier coatings- an overview.* Surface & Coatings Technology, 1987. **30**: p. 1-11.
3. Stringer, J., *Role of coatings in energy production systems: An overview.* Materials Science and Engineering, 1987. **87**: p. 1-10.
4. Miller, R., *History of thermal barrier coatings for gas turbine engines*, in *Thermal Barrier Coatings 2*. 2007: Germany.
5. Chen, M.W., R.T. Ott, T.C. Hufnagel, P.K. Wright, and K.J. Hemker, *Microstructural evolution of platinum modified nickel aluminide bond coat during thermal cycling.* Surface and Coatings Technology, 2003. **163-164**: p. 25-30.
6. Evans, H.E., *High Temperature Coatings: Protection and Breakdown*, in *Shreirs Corrosion Series*, T. Richardson, B. Cottis, R. Lindsay, S. Lyon, D. Scantlebury, F.H. Stott, and M.J. Graham, Editors. In Press.
7. Sivakumar, R. and B.L. Mordike, *High temperature coatings for gas turbine blades: A review.* Surface and Coatings Technology, 1989. **37**(2): p. 139-160.
8. Kofstad, P., *High Temperature Oxidation of Metals*. Corrosion Monograph Series. 1966: John Wiley & Sons. 338.
9. Birks, N. and G.H. Meier, *Introduction to High temperature Oxidation of Metals*. 1983: Edward Arnold Publishers Ltd.
10. Wagner, C., *Ionen Und Elektronenleitung in Silberbromid Und Abweichungen Von Der Idealen Stochiometrischen Zusammensetzung.* Zeitschrift Fur Elektrochemie, 1959. **63**(9-10): p. 1027-1030.
11. Wagner, C. and K. Grunewald, *An article on the theory of the start-up procedure. III.* Zeitschrift Fur Physikalische Chemie-Abteilung B-Chemie Der Elementarprozesse Aufbau Der Materie, 1938. **40**(6): p. 455-475.
12. Baker, M., J. Rosler, and G. Heinze, *A parametric study of the stress state of thermal barrier coatings Part II: cooling stresses.* ACTA Materialia, 2005. **53**(2): p. 469-476.
13. Chegroune, R., E. Salhi, A. Crisci, Y. Wouters, and A. Galerie, *On the Competitive Growth of Alpha and Transient Aluminas During the First Stages of Thermal Oxidation of FeCrAl Alloys at Intermediate Temperatures.* Oxidation of metals, 2008. **70**(5-6): p. 331-337.
14. Huntz, A.M., *Parabolic laws during high temperature oxidation: relations with the grain size and thickness of the oxide.* Journal of Materials Science Letters, 1999. **18**(24): p. 1981-1984.
15. Liu, Z.Y., W. Gao, and Y.D. He, *Modeling of oxidation kinetics of Y-doped Fe-Cr-Al alloys.* Oxidation of metals, 2000. **53**(3-4): p. 341-350.
16. Naumenko, D., B. Gleeson, E. Wessel, L. Singheiser, and W.J. Quadakkers, *Correlation between the microstructure, growth mechanism, and growth kinetics of alumina scales on*

a FeCrAlY alloy. Metallurgical and Materials Transactions a-Physical Metallurgy and Materials Science, 2007. **38A**(12): p. 2974-2983.

17. Wagner, C., *Theoretical Analysis Of The Diffusion Processes Determining The Oxidation Rate Of Alloys.* Journal of the Electrochemical Society, 1952. **99**(10): p. 369-380.
18. Xu, C. and W. Gao, *Pilling-Bedworth ratio for oxidation of alloys.* Materials Research Innovations, 2000. **3**: p. 231-235.
19. Pint, B.A., J.R. Martin, and L.W. Hobbs, *O-18/Sims Characterization of the Growth-Mechanism of Doped and Undoped Alpha-Al2O3.* Oxidation of metals, 1993. **39**(3-4): p. 167-195.
20. Prescott, R. and M.J. Graham, *The Formation of Aluminum-Oxide Scales on High-Temperature Alloys.* Oxidation of metals, 1992. **38**(3-4): p. 233-254.
21. Clemens, D., V.R. Vosberg, H.J. Penkalla, U. Breuer, W.J. Quadakkers, and H. Nickel. *TEM and SNMS studies on the oxidation behaviour of NiCrAlY-based coatings*. in *9th Applied Surface Analysis Workshop (AOFA 9)*. 1996. Aachen, Germany: Springer Verlag.
22. Monceau, D. and B. Pieraggi, *Determination of parabolic rate constants from a local analysis of mass-gain curves.* Oxidation of metals, 1998. **50**(5-6): p. 477-493.
23. Quadakkers, W.J., D. Naumenko, E. Wessel, V. Kochubey, and L. Singheiser, *Growth rates of alumina scales on Fe-Cr-Al alloys.* Oxidation of metals, 2004. **61**(1-2): p. 17-37.
24. Schulz, U., M. Menzebach, C. Leyens, and Y.Q. Yang, *Influence of substrate material on oxidation behavior and cyclic lifetime of EB-PVD TBC systems.* Surface and Coatings Technology, 2001. **146-147**: p. 117-123.
25. Sabol, G.P. and S.B. Dalgaard, *Origin of Cubic Rate Law in Zirconium Alloy Oxidation.* Journal of the Electrochemical Society, 1975. **122**(2): p. 316-317.
26. Quadakkers, W.J., D. Naumenko, E. Wessel, V. Kochubey, and L. Singheiser, *Growth Rates of Alumina Scales on Fe–Cr–Al Alloys.* Oxidation of metals, 2003. **61**(1/2): p. 17-37.
27. Calvarin-Amiri, G., A.M. Huntz, and R. Molins, *Effect of an applied stress on the growth kinetics of oxide scales formed on Ni20Cr alloys.* Materials at High Temperatures, 2001. **18**: p. 91-99.
28. Moulin, G., P. Arevalo, and A. Salleo, *Influence of external mechanical loadings (creep, fatigue) on oxygen diffusion during nickel oxidation.* Oxidation of metals, 1996. **45**(1): p. 153-181.
29. Pillai, S.R., N.S. Barasi, H.S. Khatak, and J.B. Gnanamoorthy, *Effect of External Stress on the Behavior of Oxide Scales on 9Cr-1Mo Steel.* Oxidation of metals, 1998. **49**(5): p. 509-530.
30. Yen, J.-Y. and J.-G. Hwu, *Enhancement of silicon oxidation rate due to tensile mechanical stress.* Applied Physics Letters, 2000. **76**(14): p. 1834-1835.
31. Evans, H.E., D.J. Norfolk, and T. Swan, *Perturbation of Parabolic Kinetics Resulting from Accumulation of Stress in Protective Oxide Layers.* Journal of the Electrochemical Society, 1978. **125**(7): p. 1180-1185.
32. Hou, P.Y., *Impurity effects on alumina scale growth.* Journal Of The American Ceramic Society, 2003. **86**(4): p. 660-668.

33. Pragnell, W.M., H.E. Evans, D. Naumenko, and W.J. Quadakkers, *Aluminium depletion in FeCrAlY steel during transitional alumina formation.* Materials at High Temperatures, 2005. **22**(3-4): p. 561-566.
34. Schumann, E. and M. Ruhle, *Microstructural Observations on the Oxidation of Gamma-Ni3al at High Oxygen Partial-Pressure.* Acta Metallurgica Et Materialia, 1994. **42**(4): p. 1481-1487.
35. Brumm, M.W. and H.J. Grabke, *The Oxidation Behavior of NiAl .1. Phase-Transformations in the Alumina Scale During Oxidation of NiAl and NiAl-Cr Alloys.* Corrosion Science, 1992. **33**(11): p. 1677-&.
36. Evans, H.E., *High Temperature Coatings:Protection and Breakdown*. 2009.
37. Ezugwu, E.O., Z.M. Wang, and A.R. Machado, *The machinability of nickel-based alloys: a review.* Journal of Materials Processing Technology, 1998. **86**(1-3): p. 1-16.
38. Giggins, C.S. and F.S. Pettit, *Oxidation Of Ni-Cr-Al Alloys Between 1000 Degrees And 1200 Degrees C.* Journal of the Electrochemical Society, 1970. **117**(8): p. C254-&.
39. Meier, G.H., *A review of advances in high-temperature corrosion.* Materials Science and Engineering A, 1989. **120-121**(Part 1): p. 1-11.
40. Stott, F.H., G.C. Wood, and J. Stringer, *The Influence of Alloying Elements on the Development and Maintenance of Protective Scales.* Oxidation of metals, 1995. **44**(1-2): p. 113-145.
41. Evans, H. and M. Taylor, *Oxidation of high-temperature coatings.* Proceedings of the Institution of Mechanical Engineers, Part G: Journal of Aerospace Engineering, 2006. **220**(1): p. 1-10.
42. Pint, B. and K. More, *Characterization of alumina interfaces in TBC systems.* Journal of Materials Science, 2009. **44**(7): p. 1676-1686.
43. Pint, B.A., *Experimental observations in support of the dynamic-segregation theory to explain the reactive-element effect.* Oxidation of metals, 1996. **45**(1): p. 1-37.
44. Pint, B.A., I.G. Wright, W.Y. Lee, Y. Zhang, K. Prüßner, and K.B. Alexander, *Substrate and bond coat compositions: factors affecting alumina scale adhesion.* Materials Science and Engineering A, 1998. **245**(2): p. 201-211.
45. Pint, B.A. *Optimization of reactive-element additions to improve oxidation performance of alumina-forming alloys*. in *2nd International Workshop on the Science and Technology of Alumina*. 2002. Schloss Ringberg, Germany: Amer Ceramic Soc.
46. Nijdam, T.J. and W.G. Sloof, *Combined pre-annealing and pre-oxidation treatment for the processing of thermal barrier coatings on NiCoCrAlY bond coatings.* Surface & Coatings Technology, 2006. **201**(7): p. 3894-3900.
47. Nijdam, T.J. and W.G. Sloof, *Effect of reactive element oxide inclusions on the growth kinetics of protective oxide scales.* ACTA Materialia, 2007. **55**(17): p. 5980-5987.
48. Naumenko, D., W.J. Quadakkers, V. Guttmann, P. Beaven, H. Al-Badairy, G.J. Tatlock, R. Newton, J.R. Nicholls, G. Strehl, G. Borchardt, J. Le Coze, B. Jonsson, and A. Westerlund. *Critical role of minor element constituents on the lifetime oxidation behaviour of FeCrAl(RE) alloys*. in *EFC Workshop on Lifetime Modelling of High Temperature Corrosion Processes*. 2001. Frankfurt, Germany: Maney Publishing.
49. Naumenko, D., J. Le-Coze, E. Wessel, W. Fischer, and W.J. Quadakkers. *Effect of trace amounts of carbon and nitrogen on the high temperature oxidation resistance of high*

purity FeCrAl alloys. in *8th International Conference on Ultra-High Purity Base Metals (UHPM-2001)*. 2001. Berlin, Germany: Japan Inst Metals.

50. Hindam, H. and D.P. Whittle, *Peg Formation by Short-Circuit Diffusion in Al2O3 Scales Containing Oxide Dispersions.* Journal of the Electrochemical Society, 1982. **129**(5): p. 1147-1149.
51. Tien, J.K. and F.S. Pettit, *Mechanism of Oxide Adherence on Fe-25Cr-4Al (Y or Sc) Alloys.* Metallurgical Transactions, 1972. **3**(6): p. 1587-&.
52. Subanovic, M., D. Naumenko, M. Kamruddin, G. Meier, L. Singheiser, and W.J. Quadakkers, *Blistering of MCrAlY-coatings in H-2/H2O-atmospheres.* Corrosion Science, 2009. **51**(3): p. 446-450.
53. Clemens, D., K. Bongartz, W. Speier, R.J. Hussey, and W.J. Quadakkers. *Analysis and Modeling of Transport Processes in Alumina Scales on High-Temperature Alloys*. in *7th Working Conf on Applied Surface Analysis*. 1992. Julich, Germany: Springer Verlag.
54. Whittle, D.P. and J. Stringer, *Improvements in High-Temperature Oxidation Resistance by Additions of Reactive Elements or Oxide Dispersions.* Philosophical Transactions of the Royal Society of London Series a-Mathematical Physical and Engineering Sciences, 1980. **295**(1413).
55. Kuenzly, J.D. and D.L. Douglass, *Oxidation Mechanism of Ni3Al Containing Yttrium.* Oxidation of metals, 1974. **8**(3): p. 139-178.
56. Gil, A., V. Shemet, R. Vassen, M. Subanovic, J. Toscano, D. Naumenko, L. Singheiser, and W.J. Quadakkers, *Effect of surface condition on the oxidation behaviour of MCrAlY coatings.* Surface & Coatings Technology, 2006. **201**(7): p. 3824-3828.
57. Pilling, N.B. and R.E. Bedworth, *The oxidation of metals at high temperatures.* Journal of the Institute of Metals, 1923. **29**: p. 529-582.
58. Evans, H.E., *Stress Effects in High-Temperature Oxidation of Metals.* International Materials Reviews, 1995. **40**(1): p. 1-40.
59. Fromhold, A.T., *Theory of Metal Oxidation 2*. 1975.
60. Borie, B., C.J. Sparks, and J.V. Cathcart, *Epitaxially Induced Strains in Cu2o Films on Copper Single Crystals .1. X-Ray Diffraction Effects.* Acta Metallurgica, 1962. **10**(AUG): p. 691-&.
61. Evans, H.E. and R.C. Lobb, *Conditions for the initiation of oxide-scale cracking and spallation.* Corrosion Science, 1984. **24**(3): p. 209-222.
62. Carling, K.M. and E.A. Carter, *Effects of segregating elements on the adhesive strength and structure of the alpha-Al2O3/beta-NiAl interface.* ACTA Materialia, 2007. **55**(8): p. 2791-2803.
63. Goward, G.W., *Protective coatings - purpose, role, and design.* Materials Science and Technology, 1986. **2**: p. 194-198.
64. Walston, W.S. *Coating and Surface Technologies for Turbine Airfoils*. in *Superalloys 2004*. 2004.
65. Pomeroy, M.J., *Coatings for gas turbine materials and long term stability issues.* Materials and Design, 2004.
66. Fu, C.L., R. Reed, A. Janotti, and M. Krcmar. *On the diffusion of alloying elements in the nickel base superalloys*. in *Superalloys 2004*. 2004.

67. Xie, L., Y.H. Sohn, E.H. Jordan, and M. Gell, *The effect of bond coat grit blasting on the durability and thermally grown oxide stress in an electron beam physical vapor deposited thermal barrier coating.* Surface and Coatings Technology, 2003. **176**: p. 57-66.
68. Karlsson, A.M., J.W. Hutchinson, and A.G. Evans, *The displacement of the thermally grown oxide in thermal barrier systems upon temperature cycling.* Materials Science and Engineering A, 2003. **351**: p. 244-257.
69. Madhwal, M., E.H. Jordan, and M. Gell, *Failure mechanisms of dense vertically-cracked thermal barrier coatings.* Materials Science and Engineering A, 2004. **384**: p. 151-161.
70. Darzans, S. and A.M. Karlsson, *On the microstructural development in platinum-modified nickel-aluminide bond coats.* Surface and Coatings Technology, 2004. **177-178**: p. 108-112.
71. Evans, H.E. and M.P. Taylor, *Creep relaxation and the spallation of oxide layers.* Surface and Coatings Technology, 1997. **94-95**: p. 27-33.
72. Nicholls, J.R., *Designing Oxidation-Resistant Coatings.* Journal of Materials, 2000: p. 28-35.
73. Saunders, S.R.J. and J.R. Nicholls, *Coatings and surface treatments for high temperature oxidation resistance.* Materials Science and Technology, 1989. **5**: p. 780-798.
74. Levi, C.G., *Emerging materials and processes for thermal barrier systems.* Current Opinion in Solid State and Materials Science, 2004. **8**: p. 77-91.
75. Sturgeon, A., *Ceramic coatings-a growing technology.* TWI Bulletin, 1992. **March/April**: p. 31-35.
76. Stringer, J., *Role of coatings in energy-producing systems: An overview.* Materials Science and Engineering, 1987. **87**: p. 1-10.
77. *Gordon England Limited*. [cited 2009; Available from: www.gordonengland.co.uk.
78. http://en.wikipedia.org/wiki/Electron_beam_physical_vapor_deposition. 2010 [cited; Available from: http://en.wikipedia.org/wiki/Electron_beam_physical_vapor_deposition.
79. Mevrel, R., C. Duret, and R. Pichoir, *Pack cementation process.* Materials Science and Technology, 1986. **2**: p. 201-205.
80. Kung, S.C. and R.A. Rapp, *Analyses of the Gaseous Species in Halide-Activated Cementation Coating Packs.* Oxidation of metals, 1989. **32**(1-2): p. 89-109.
81. Chen, J.H. and J.A. Little, *Degradation of the platinum aluminide coating on CMSX4 at 1100 °C.* Surface and Coatings Technology, 1997. **92**(1-2): p. 69-77.
82. Tawancy, H.M., N.M. Abbas, and T.N. Rhysjones. *Effect of Substrate Composition on the Oxidation Behavior of Platinum-Aluminized Nickel-Base Superalloys*. in *19th International Conf on Metallurgical Coatings and Thin Films*. 1992. San Diego, Ca: Elsevier Science Sa Lausanne.
83. Tawancy, H.M., N.M. Abbas, and T.N. Rhys-Jones, *Role of platinum in aluminide coatings.* Surface and Coatings Technology, 1991. **49**(1-3): p. 1-7.
84. Zhang, Y.H., D.M. Knowles, and P.J. Withers, *Microstructural development in Pt-aluminide coating on CMSX-4 superalloy during TMF.* Surface and Coatings Technology, 1998. **107**(1): p. 76-83.
85. Zhao, X. and P. Xiao, *Effect of platinum on the durability of thermal barrier systems with a [gamma] + [gamma]' bond coat.* Thin Solid Films, 2008. **517**(2): p. 828-834.

86. Rickerby, D.S., R.G. Wing, and S.R. Bell, *Method of applying a thermal barrier coating to a superalloy article and a thermal barrier coating*. 1995, Rolls-Royce PLC
Chromalloy UK Ltd.

87. Stringer, J., *Coatings in the electricity supply industry: past, present, and opportunities for the future.* Surface and Coatings Technology, 1998. **108-109**(1-3): p. 1-9.

88. Panat, R., S. Zhang, and K.J. Hsia, *Bond coat surface rumpling in thermal barrier coatings.* ACTA Materialia, 2002. **51**: p. 239-249.

89. Kokini, K., Y.R. Takeuchi, and B.D. Choules, *Surface thermal cracking of thermal barrier coatings owing to stress relaxation: zirconia vs mullite.* Surface and Coatings Technology, 1996. **82**: p. 77-82.

90. Winter, M.R. and D.R. Clarke, *Thermal conductivity of yttria-stabilized zirconia-hafnia solid solutions.* ACTA Materialia, 2006. **54**(19): p. 5051-5059.

91. Barea, R., M.I. Osendi, J.M.F. Ferreira, and P. Miranzo, *Thermal conductivity of highly porous mullite material.* ACTA Materialia, 2005. **53**(11): p. 3313-3318.

92. Nicholls, J.R., K.J. Lawson, A. Johnstone, and D.S. Rickerby, *Methods to reduce the thermal conductivity of EB-PVD TBC's.* Surface and Coatings Technology, 2002. **151-152**: p. 383-391.

93. Lutique, S., D. Staicu, R.J.M. Konings, V.V. Rondinella, J. Somers, and T. Wiss, *Zirconate pyrochlore as a transmutation target: thermal behaviour and radiation resistance against fission fragment impact.* Journal of Nuclear Materials, 2003. **319**: p. 59-64.

94. Rabiei, A. and A.G. Evans, *Failure mechanisms associated with the thermally grown oxide in plasma sprayed thermal barrier coatings.* ACTA Materialia, 2000. **48**: p. 3963-3976.

95. Wu, F., H. Murakami, and A. Suzuki, *Development of an iridium-tantalum modified aluminide coating as a diffusion barrier on nickel-base single crystal superalloy TMS-75.* Surface and Coatings Technology, 2003. **168**(1): p. 62-69.

96. Strawbridge, A. and H.E. Evans, *Mechanical Failure of Thin Brittle Coatings.* Engineering failure Analysis, 1995. **2**(2): p. 85-103.

97. Wang, J.-S. and A.G. Evans, *Measurement and analysis of buckling and buckle propagation in compressed oxide layers on superalloy substrates.* ACTA Materialia, 1998. **46**(14): p. 4993-5005.

98. Bull, S.J., *Failure modes in scratch adhesion testing.* Surface and Coatings Technology, 1991. **50**(1): p. 25-32.

99. Mao, W.G., C.Y. Dai, Y.C. Zhou, and Q.X. Liu, *An experimental investigation on thermo-mechanical buckling delamination failure characteristic of air plasma sprayed thermal barrier coatings.* Surface and Coatings Technology, 2007. **201**(14): p. 6217-6227.

100. Sohn, Y.H., J.H. Kim, E.H. jordan, and M. Gell, *Thermal cycling of EB-PVD/MCrAlY thermal barrier coatings :I.
Microstructural development and spallation mechanisms.* Surface and Coatings Technology, 2001. **146-147**: p. 70-78.

101. Choi, R.S., J.W. Hutchinson, and A.G. Evans, *Delamination of multilayer thermal barrier coatings.* Mechanics of Materials, 1999. **31**: p. 431-447.

102. Vaidyanathan, K., M. Gell, and E.H. Jordan, *Mechanisms of spallation of electron beam physical vapor deposited thermal barrier coatings with and without platinum aluminide bond coat ridges.* Surface and Coatings Technology, 2000. **133-134**: p. 28-34.

103. Tolpygo, V.K. and D.R. Clarke, *On the rumpling mechanism in nickel-aluminide coatings Part 1: an experimental assessment.* ACTA Materialia, 2004. **52**: p. 5115-5127.

104. Chau, E., *A High Temperature Oxidation Study of Two Coating Systems*, in *Department of Metallurgy and Materials*. 2002, University of Birmingham.

105. Taylor, M.P. and H.E. Evans. *Formation of diffusion cells in LPPS MCrAIY coatings*. in *5th International Conference on the Microscopy of Oxidation*. 2002. Limerick, Ireland.

106. Taylor, M.P., W.M. Pragnell, and H.E. Evans, *The influence of bond coat surface roughness on chemical failure and delamination in TBC systems.* Materials and Corrosion-Werkstoffe Und Korrosion, 2008. **59**(6): p. 508-513.

107. Evans, H.E. and M.P. Taylor, *Diffusion Cells and Chemical Failure of MCrAlY Bond Coats in Thermal Barrier Coating Systems.* Oxidation of metals, 2000. **55**: p. 17-34.

108. Renusch, D., M. Schorr, and M. Schutze, *The role that bond coat depletion of aluminum has on the lifetime of APS-TBC under oxidizing conditions.* Materials and Corrosion-Werkstoffe Und Korrosion, 2008. **59**(7): p. 547-555.

109. Chen, M.W., M.L. Glynn, R.T. Ott, T.C. Hufnagel, and K.J. Hemker, *Chracterisation and modeling of a martensitic transformation in a platinum modified diffusion aluminide bond coat for thermal barrier coatings.* ACTA Materialia, 2003. **51**: p. 4279-4294.

110. Angenete, J., K. Stiller, and E. Bakchinova, *Microstructural and microchemical development of a simple and Pt-modified aluminide coatings during long term oxidation at 1050 C.* Surface and Coatings Technology, 2004. **176**: p. 272-283.

111. Kim, H.J. and M.E. Walter, *Characterisation of the degraded microstructure of a platinum aluminide coating.* Materials Science and Engineering A, 2003. **360**: p. 7-17.

112. Pan, D., M.W. Chen, P.K. Wright, and K.J. Hemker, *Evolution of a diffusion aluminide bond coat for thermal barrier coatings during thermal cycling.* ACTA Materialia, 2003. **51**: p. 2205-2217.

113. Vaidyanathan, K., E.H. Jordan, and M. Gell, *Surface geometry and strain energy effects in the failure of a (Ni,Pt)Al/EB-PVD thermal barrier coating.* ACTA Materialia, 2004. **52**: p. 1107-1115.

114. Busso, E.P., Z.Q. Qian, M.P. Taylor, and H.E. Evans, *The influence of bondcoat and topcoat mechanical properties on stress development in thermal barrier coating systems.* ACTA Materialia, 2009. **57**(8): p. 2349-2361.

115. Lau, H., C. Leyens, U. Schulz, and C. Friedrich, *Influence of bondcoat pre-treatment and surface topography on the lifetime of EB-PVD TBC's.* Surface and Coatings Technology, 2003. **165**: p. 217-223.

116. Evans, A.G., M.Y. He, and J.W. Hutchinson, *Effect of interface undulations on the thermal fatigue of thin films and scales on metal substrates.* ACTA Materialia, 1997. **45**(9): p. 3543-3554.

117. He, M.Y., A.G. Evans, and J.W. Hutchinson, *The ratcheting of compressed thermally grown thin films on ductile substrates.* ACTA Materialia, 2000. **48**: p. 2593-2601.

118. Tolpygo, V.K. and D.R. Clarke, *On the rumpling mechanism in nickel-aluminide coatings*

Part II: characterisation of surface undulations and bond coat swelling. ACTA Materialia, 2004. **52**: p. 5129-5141.

119. Tolpygo, V.K. and D.R. Clarke, *Surface rumpling of a (Ni, Pt)Al bond coat induced by cyclic oxidation.* ACTA Materialia, 2000. **48**: p. 3283-3293.
120. Tolpygo, V.K. and D.R. Clarke, *Morphological evolution of thermal barrier coatings induced by cyclic oxidation.* Surface and Coatings Technology, 2003. **163-164**: p. 81-86.
121. Balint, D.S., T. Xu, J.W. Hutchinson, and A.G. Evans, *Influence of bond coat thickness on the cyclic rumpling of thermally grown oxides.* ACTA Materialia, 2006. **54**(7): p. 1815-1820.
122. Goniakowski, J. and C. Noguera, *Relaxation and rumpling mechanisms on oxide surfaces.* Surface Science, 1995. **323**(1-2): p. 129-141.
123. Tolpygo, V.K. and D.R. Clarke, *Temperature and cycle-time dependence of rumpling in platinum-modified diffusion aluminide coatings.* Scripta Materialia, 2007. **57**(7): p. 563-566.
124. Tolpygo, V.K. and D.R. Clarke, *Rumpling of CVD (Ni,Pt)Al diffusion coatings under intermediate temperature cycling.* Surface and Coatings Technology, 2009. **203**(20-21): p. 3278-3285.
125. Tolpygo, V.K., K.S. Murphy, and D.R. Clarke, *Effect of Hf, Y and C in the underlying superalloy on the rumpling of diffusion aluminide coatings.* ACTA Materialia, 2008. **56**(3): p. 489-499.
126. Wen, M., E.H. Jordan, and M. Gell, *Effect of temperature on rumpling and thermally grown oxide stress in an EB-PVD thermal barrier coating.* Surface and Coatings Technology, 2006. **201**(6): p. 3289-3298.
127. Dryepondt, S. and D.R. Clarke, *Effect of superimposed uniaxial stress on rumpling of platinum-modified nickel aluminide coatings.* ACTA Materialia, 2009. **57**(7): p. 2321-2327.
128. Dryepondt, S., J.R. Porter, and D.R. Clarke, *On the initiation of cyclic oxidation-induced rumpling of platinum-modified nickel aluminide coatings.* ACTA Materialia, 2009. **57**(6): p. 1717-1723.
129. Haynes, J.A., B.A. Pint, W.D. Porter, and I.G. Wright, *Comparison of thermal expansion and oxidation behaviour of various high-temperature coating materials and superalloys.* Materials at High Temperatures, 2004. **21**(2): p. 87-94.
130. Wilson, B., *Solution heat treatment responce of CMSX-4.* Journal of Undergraduate Research, 2002. **3**(7).
131. Doychak, J. and M. Ruhle, *Tem Studies of Oxidized Nial and Ni3al Cross-Sections.* Oxidation of metals, 1989. **31**(5-6): p. 431-452.
132. Shillington, E.A.G. and D.R. Clarke, *Spalling failure of a thermal barrier coating associated with aluminum depletion in the bond-coat.* ACTA Materialia, 1999. **47**(4): p. 1297-1305.
133. Tolpygo, V.K. and D.R. Clarke, *Microstructural study of the theta-alpha transformation in alumina scales formed on nickel-aluminides.* Materials at High Temperatures, 2000. **17**(1): p. 59-70.

134. Hou, P.Y., A.P. Paulikas, and B.W. Veal, *Strains in thermally growing alumina films measured in-situ using synchrotron x-rays.* High-Temperature Oxidation and Corrosion 2005, 2005. **522-523**: p. 433-440.
135. Al-Badairy, H. and T.G. J. *Mechanistic understanding of the chemical failure of FeCrAl-RE alloys in oxidising environments*. in *EFC Workshop on Lifetime Modelling of High Temperature Corrosion Processes*. 2001. Frankfurt, Germany: Maney Publishing.
136. Hindam, H. and D.P. Whittle, *Microstructure, Adhesion and Growth-Kinetics of Protective Scales on Metals and Alloys.* Oxidation of metals, 1982. **18**(5-6): p. 245-284.
137. Tolpygo, V.K. and D.R. Clarke, *Surface rumpling of a (Ni, Pt)Al bond coat induced by cyclic oxidation.* ACTA Materialia, 2000. **48**(13): p. 3283-3293.
138. Tolpygo, V.K. and D.R. Clarke, *On the rumpling mechanism in nickel-aluminide coatings - Part II: characterization of surface undulations and bond coat swelling.* ACTA Materialia, 2004. **52**(17): p. 5129-5141.
139. Tolpygo, V.K. and D.R. Clarke, *Rumpling induced by thermal cycling of an overlay coating: the effect of coating thickness.* ACTA Materialia, 2004. **52**(3): p. 615-621.
140. Mumm, D.R., A.G. Evans, and I.T. Spitsberg, *Characterization of a cyclic displacement instability for a thermally grown oxide in a thermal barrier system.* ACTA Materialia, 2001. **49**(12): p. 2329-2340.
141. Tolpygo, V.K. and D.R. Clarke, *On the rumpling mechanism in nickel-aluminide coatings - Part I: an experimental assessment.* ACTA Materialia, 2004. **52**(17): p. 5115-5127.
142. Tolpygo, V.K., D.R. Clarke, and K.S. Murphy, *Evaluation of interface degradation during cyclic oxidation of EB-PVD thermal barrier coatings and correlation with TGO luminescence.* Surface and Coatings Technology, 2004. **188-189**: p. 62-70.
143. Busso, E.P., L. Wright, H.E. Evans, L.N. McCartney, S.R.J. Saunders, S. Osgerby, and J. Nunn, *A physics-based life prediction methodology for thermal barrier coating systems.* ACTA Materialia, 2007. **55**(5): p. 1491-1503.
144. Busso, E.P., Z.Q. Qian, H.E. Evans, and M.P. Taylor, *Unpublished Work.*
145. Toscano, J., R. Vaen, A. Gil, M. Subanovic, D. Naumenko, L. Singheiser, and W.J. Quadakkers, *Parameters affecting TGO growth and adherence on MCrAlY-bond coats for TBC's.* Surface and Coatings Technology, 2006. **201**(7): p. 3906-3910.
146. Evans, H.E. and M.P. Taylor, *Delamination Processes in Thermal Barrier Coating Systems.* Journal Article, In Press.
147. Balint, D.S. and J.W. Hutchinson, *An analytical model of rumpling in thermal barrier coatings.* Journal of the Mechanics and Physics of Solids, 2005. **53**(4): p. 949-973.
148. Lee, E.Y., D.M. Chartier, R.R. Biederman, and R.D. Sisson, *Modeling the Microstructural Evolution and Degradation of M-Cr-Al-Y Coatings During High-Temperature Oxidation.* Surface & Coatings Technology, 1987. **32**(1-4): p. 19-39.
149. Saeidi, S., K.T. Voisey, and D.G. McCartney, *The Effect of Heat Treatment on the Oxidation Behavior of HVOF and VPS CoNiCrAlY Coatings.* Journal of Thermal Spray Technology, 2009. **18**(2): p. 209-216.
150. Pietrangeli, E., F. Cappuccini, M. Bellacci, F. Iozzelli, and M. Romanelli, *Characterization and oxidation damage modelling of MCrAlY.* Proceedings of the ASME Turbo Expo 2006, Vol 4, 2006: p. 925-930.

151. Nijdam, T.J. and W.G. Sloof, *Microstructural evolution of a MCrAlY coating upon isothermal annealing*. Materials Characterization, 2008. **59**(12): p. 1697-1704.
152. Mendis, B.G., B. Tryon, T.M. Pollock, and K.J. Hemker. *Microstructural observations of as-prepared and thermal cycled NiCoCrAlY bond coats*. in *33rd International Conference on Metallurgical Coatings and Thin Films*. 2006. San Diego, CA: Elsevier Science Sa.
153. *ASM handbook. Vol.3, Alloy phase diagrams*. Vol. Volume 3. 1992: Metals Park, Ohio : ASM International, 1992.
154. Jackson, R.D., *The Oxidation of two Bondcoats in a Thermal Barrier Coating System*, in *Department of Metallurgy and Materials*. 2005, University of Birmingham.
155. Niranatlumpong, P., *Oxidation Behaviour and Failure Mechanisms of NiCrAlY Overlay Coating and ZrO2-8wt% Y2O3/NiCrAlY Thermal Barrier Coating*. 1999, University of Birmingham.
156. Adesanya, O.A., K. Bouhanek, F.H. Stott, P. Skeldon, D.G. Lees, and G.C. Wood, *Cyclic oxidation of two bond coats in thermal barrier coating systems on CMSX-4 substrates.* High Temperature Corrosion and Protection of Materials 5, Pts 1 and 2, 2001. **369-3**: p. 639-646.
157. Monceau, D., F. Crabos, A. Malie, and B. Pieraggi, *Effects of bond-coat preoxidation and surface finish on isothermal and cyclic oxidation, high temperature corrosion and thermal shock resistance of TBC systems.* High Temperature Corrosion and Protection of Materials 5, Pts 1 and 2, 2001. **369-3**: p. 607-614.
158. Bouhanek, K., O.A. Adesanya, F.H. Stott, P. Skeldon, D.G. Lees, and G.C. Wood, *High temperature oxidation of thermal barrier coating systems on RR3000 substrates: Pt aluminide bond coats.* High Temperature Corrosion and Protection of Materials 5, Pts 1 and 2, 2001. **369-3**: p. 615-622.
159. Saunders, S.R.J., *Unpublished Work.*
160. Taylor, M.P., *Unpublished Work.*
161. Yanar, N.M., G.H. Meier, and F.S. Pettit, *The influence of platinum on the failure of EBPVD YSZ TBC's on NiCoCrAlY bond coats.* Scripta Materialia, 2002. **46**: p. 325-330.
162. Sun, J.H., E. Chang, C.H. Chao, and M.J. Cheng, *The Spalling Modes and Degradation Mechanism of ZrO2-8 Wt-Percent Y2O3/CVD-Al2O3/Ni-22Cr-10Al-1Y Thermal-Barrier Coatings.* Oxidation of metals, 1993. **40**(5-6): p. 465-481.
163. Lih, W., E. Chang, B.C. Wu, C.H. Chao, and A. Peng, *Effect of Bond-Coat Pre-Aluminization and Preoxidation Duplex Pretreatment on the Performance of ZrO2-8 Wt-Percent Y2O3/Co-29Cr-6Al-1Y Thermal-Barrier Coatings.* Oxidation of metals, 1993. **40**(3-4): p. 229-243.